ABSTRACT

Title of dissertation:	ADVANCING NITROUS OXIDE AS A MONOPROPELLANT USING INDUCTIVELY HEATED HEAT-EXCHANGERS: THEORY AND EXPERIMENT
	Pratik Sharma Saripalli Doctor of Philosophy, 2019
Dissertation directed by:	Professor Raymond J. Sedwick Department of Aerospace Engineering

Most monopropellant thrusters used for attitude control and station keeping employ hydrazine as their propellant. In recent years, significant effort has been focused on finding an alternative due to its high toxicity. This work focuses on advancing nitrous oxide, a green monopropellant with a strong performance capability, as a replacement for current monopropellant thrusters. A large emphasis is placed on trying to address catalyst degradation experienced in most thrusters due to the high temperatures from decomposition. The approach described here eliminates the dependence for a high catalytic surface area, typically decreased from degradation, and catalysts altogether by using high temperature porous heat exchangers.

A 1-D numerical compressible fluid model was created to model a typical decomposition chamber and simulate self-sustained decomposition of nitrous oxide. It implements a preheated, thermally-conductive, metal foam as the heat exchanger. An extensive parameter study was conducted to help understand thermal and fluid

effects on steady-state decompositions. Using a copper metal foam, steady-state solutions simulated successful nitrous oxide decomposition, with an exit gas temperature around 1345 K. Simulations were extended to other high temperature metal foams with different thermal conductivities and melting points. Modeling flow rate conditions more representative of current monopropellant thrusters required scaling of the decomposition chamber in order to be self-sustaining.

Experiments were conducted using results from the numerical simulations as guidelines. Three different heat exchangers (copper metal foam, copper discs, and stainless-steel discs), all of which have significantly less effective surface area than nominal catalysts used in thrusters, were tested for nitrous oxide decomposition. These heat exchangers were preheated to thermal decomposition temperatures using an inductive heating system and placed in a vacuum bell jar to mitigate heat loss to the environment. Testing with copper metal foam resulted in complete degradation of the heat exchanger due to oxidation from nitrous oxide decomposition. A set of copper discs, uniquely designed to maximize tortuosity of the flow, was implemented in an attempt to address the oxidation issues. While the preliminary test did confirm steady-state decomposition of nitrous oxide within the heat exchanger, further tests resulted in temperatures exceeding the melting point of copper within the discs. The last heat exchanger was a set of stainless-steel discs of the same design. Repeated tests all successfully achieved steady-state decomposition of nitrous oxide within a two-minute interval.

ADVANCING NITROUS OXIDE AS A MONOPROPELLANT USING INDUCTIVELY HEATED HEAT-EXCHANGERS: THEORY AND EXPERIMENT

by

Pratik Sharma Saripalli

Dissertation submitted to the Faculty of the Graduate School of the
University of Maryland, College Park in partial fulfillment
of the requirements for the degree of
Doctor of Philosophy
2019

Advisory Committee:
Professor Raymond J. Sedwick, Advisor
Professor Kenneth Yu, Chair
Professor James Baeder
Professor Christine Hartzell
Professor Adil Hassam

Dedication

To my future wife, wherever you are. I've been searching for you throughout this journey.

Acknowledgments

"The future belongs to those who believe in the beauty of their dreams."

- Eleanor Roosevelt

I've always dreamed of earning the "Dr" in front of my name. The fact that I've accomplished it; I still can't fathom. It is difficult to describe in words the sheer amount of support and help I received during this journey. My quest for a doctorate required a better part of a decade and to this date, is my biggest achievement. The endless nights and countless hours spent all culminate to this single moment of my life and it could not have been possible without the following people.

First and foremost, I want to thank my advisor, Dr. Raymond John Sedwick for believing in me and taking a chance. He has been my teacher for over ten years and has not only nurtured me into a scholar but also as an individual. Without his guidance and support, I would not be writing this today. Not once during my quest has he ever stopped encouraging me, assisting me, giving me "pep talks" or solving all my issues. He has always been invested in my degree just as much as I have. Who knew a simple email in 2010 for lab experience would kickstart an almost seven year career into a PhD. I would like to extend my thanks to my committee for offering advice and guidance on my work.

My lab mates (Elaine, John, Arber, Drew, Eric, Adriane, Allison, Josh, Matt, Jarred, Adam, New Matt, Melissa, and Jason) deserve a lot of credit for putting up with me. Over the years, you guys became some of my closest friends. Only you know about the late night rants when everything fails, the random conversations

I would like to thank NASA for the financial support via the Harriett Jenkins Graduate Fellowship and specifically, my mentor Dr. Eric Cardiff for his encouragement throughout this endeavor.

Last but certainly not least, I want to say thank you to my family. To my parents, sister, relatives in India; thank you. Without you, I would not be here, or anywhere. The sacrifices made to provide me with the opportunity to learn I will never forget. I hope to have made you proud. Your constant love and support is what kept me going. I love you all. While my years as a student come to a close, I will take with me the lessons and experience I have gained to wherever my life leads me next. I promise to always strive to be better than my current self and to never fall short of greatness.

Honorary Mentions

The various pets I have had the pleasure of meeting, in no particular order: Ally the "always hungry", Horton the Defender, Sophie the Scardy-Cat #1, Penny the Scardy-Cat #2, Clyde the Hunter, Ari the Cutie, Ruby the Tiny, and PoohBear the PoohBear.

To all my housing locations outside of Campus (The House, View, Terrapin Row, Landmark): Thanks for letting me stay and charging an obscene amount of rent. It is because of you that the jokes of "You are still in CP?" never stopped.

UMD Department of Transportation: Thank you for taking all my money for parking tickets. It's made me much more conscious about money and where to park. I will hate you forever.

Table of Contents

List of Tables

List of Figures

List of Abbreviations and Nomenclature

C	Capacitance, $[F]$
I	Current, $[A]$
Dn	Damköhler number
X	Design matrix for linear regression analysis
σ	Effective surface area, $[\frac{m^2}{m^3}]$
ϵ	Emissivity
E_o	Energy required to preheat heat-exchangers, $[J]$
q_d	Energy released from decomposition, $[\frac{J}{kg}]$
F_b	External friction force describing difficulty of fluid moving through a porous material, $[\frac{N}{m^3}]$
b_{slope}	Fitted slope parameter
η	Fluid dynamic viscosity, $[\frac{N-s}{m^2}]$
f	Frequency, $[Hz]$
ρ_{prod}	Gas product density, $[\frac{kg}{m^3}]$
u	Gas velocity, $[\frac{m}{s}]$
$\vec{j_c}$	Heat flux term due to conduction, $[\frac{W}{m^2}]$
$\vec{j_a}$	Heat flux term due to advection, $[\frac{W}{m^2}]$
h	Heat transfer coefficient (between nitrous oxide and porous material), $[\frac{W}{m^2-K}]$
t	Inverse of the Student's t cumulative distributive function
L	Length of setup, $[m]$
L	Inductance, $[H]$
μ_o	Magnetic permeability constant, $[\frac{H}{m}]$
$\dot{m}$	Mass flow rate, $[\frac{kg}{s}]$
$\frac{\dot{m}}{Area}$	Mass flux term, $[\frac{kg}{m^2-s}]$
m_p	Mass of propellant, $[kg]$
s^2	Mean-squared error for regression analysis
$[M]$	Molar concentration of collision partner, $[\frac{mol}{cm^3}]$
χ_A	Mole fraction of species A
MW_A	Molecular weight of species A
Mol_A	Moles of species A
N_2O	Nitrous oxide
Nu	Nusselt number
K	Permeability of the foam, $[m^2]$
P	Porosity
PPI	Pores Per Inch
P_{dcp}	Power from decomposition, $[W]$
P_w	Power into Workpiece, $[W]$
P_{lh}	Power lost to the decomposition chamber and housing, $[W]$

P_{lc}	Power lost to circuit heating, $[W]$
P_{crc}	Power (net) from the DC power supply, $[W]$
Pr	Prandtl number
p_g	Pressure of gas, $[Pa]$
r	Radius of cylinder, $[m]$
α	Rate of decomposition of nitrous oxide, $[\frac{1}{sec}]$
α_0	Rate of decomposition of nitrous oxide, low pressure, $[\frac{1}{sec}]$
α_∞	Rate of decomposition of nitrous oxide, high pressure, $[\frac{cm^3}{sec*mol}]$
γ	Ratio of specific heats
μ	Relative permeability
R	Resistance, $[Ohm]$
ρ	Resistivity of the workpiece, $[Ohm - cm^2]$
Re	Reynolds number
d	Skin depth, $[cm]$
Δx	Spatial resolution, $[m]$
Cp_a	Specific heat capacity of material/gas a as a function of its temperature , $[\frac{J}{kg-K}]$
h_o	Specific total enthalpy of the gas, $[\frac{J}{kg}]$
h_g	Specific enthalpy of the gas, $[\frac{J}{kg}]$
Isp	Specific Impulse, $[sec]$
σ_i	Standard deviation
σ_b	Stefan-Boltzman constant, 5.6 x 10^{-8} $[\frac{W}{m^2-K^4}]$
T_a	Temperature for material/gas a, $[K]$
Δt	Temporal resolution, $[s]$
th_a	Thickness of material a, $[m]$
h_{a-b}	Thermal contact conductance factor between materials a and b, $[\frac{W}{m^2-K}]$
k_a	Thermal conductivity for material/gas a, $[\frac{W}{m-K}]$
D	Thermal diffusivity constant, $[\frac{m^2}{s}]$
t_{teff}	Total operation time for efficiency, $[sec]$
ρ_{gas}	Total gas density, $[\frac{kg}{m^3}]$
n	Total number of spatial nodes
n_t	Total number of temporal nodes
t_{max}	Total time, $[sec]$
R, R_u	Universal gas constant, $[\frac{J}{mol-K}]$, $[\frac{Cal}{mol-K}]$
$\dot{Q}$	Volumetric power term, $[\frac{W}{m^3}]$
w_i	Weights for least square analysis
$AFRL$	Air Force Research Laboratory

COTS	Commercial Off-The-Shelf
DOT	Department of Transportation
ESA	European Space Agency
FOI	Swedish Defense Agency
GPIM	Green Propellant Infusion Mission
GSE	Ground Support Equipment
JAXA	Japan Aerospace Exploration Agency
MSDS	Material Safety Data Sheet
NACA	National Advisory Committee for Aeronautics
NASA	National Aeronautics and Space Administration
NFPA	National Fire Prevention Association
NOFBX	Nitrous Oxide Fuel Blends
PPE	Personal Protective Equipment
RCS	Reaction Control Systems
SCAPE	Self-Contained Hazardous Material Suites
SCAT	Secondary Combustion Augmented Thruster
SSTL	Surrey Satellite Technology Ltd

Chapter 1: Introduction

1.1 Motivation

Since the beginning of space travel in the late 50's, there has been a never-ending yearn to seek the unknown. Sputnik 1 proved to mankind that in time, anything impossible will become possible. Throughout the years, the evolution of propulsion technologies allowed the collective "we" to push all the boundaries of the tangible world. Whereas the advent of electric propulsion helped kickstart the quest for propellant-efficient systems, the improvement of chemical propulsion proved vital for all spacecrafts for simple yet important space maneuvers. Chemical propulsion systems generate thrust by expanding a heated gas (fuel) using a nozzle, converting thermal to kinetic energy and expelling it (reaction mass). The fuel is generally a mixture between propellant and an oxidizer that can combust to create thermal energy. Monopropellant thrusters, however, are chemical propulsion systems that take advantage of propellants with exothermic decompositions, removing the need for a separate oxidizer.

Monopropellant thrusters are widely used in spacecraft attitude control and station keeping for satellites. They generally function by using a catalyst bed to exothermically decompose propellant (for increased specific impulse when compared

to cold gas thrusters) and harness the released thermal energy as thrust. Hydrazine and hydrogen peroxide are among the most used in such propulsion systems and are a proven technology. However, in recent years, research has sparked into finding a "green" alternative to these propellants since their toxicity and inherent flammability make them difficult and costly to handle [3–6].

Nitrous oxide is a potentially favorable alternative primarily due to its classification as a green propellant [6, 7]. The decomposition of N_2O is an exothermic process, and when properly achieved can provide performance similar to current monopropellants. Hydrazine and hydrogen peroxide both require extra pressurization systems due to their low vapor pressures whereas N_2O will self pressurize. Furthermore, hydrazine and hydrogen peroxide have freezing points around 273 K whereas nitrous oxide freezes around 188 K, giving it an edge in functionality in space conditions [4].

The decomposition of nitrous oxide releases a net thermal energy, which can then be converted to kinetic energy for thrust. Uncatalyzed, self-sustained thermal decomposition is only possible at temperatures higher than 1073 K since at that point, the rate of heat dissipation is approximately equal to the rate of heat generation [3, 8]. Potential performance of these propellants must also be taken into account when determining viable replacements. Throughout this work, performance will be compared using specific impulse. Specific impulse (Isp) is defined as the exit gas velocity normalized by the Earth's gravity. The higher the specific impulse, the more mass efficient a thruster for a desired thrust. The maximum theoretical specific impulse of catalytic nitrous oxide systems is about 206 seconds at a temperature of

about 1913 K (assuming a chamber pressure and nozzle expansion ratio) [4].

Past research conducted on the feasibility of nitrous oxide as a monopropelant involved catalytic decomposition, similar to hydrazine monopropellant thrusters [5]. Research at the Surrey Space Center [3, 4] focused on the decomposition of nitrous oxide using a wide variety of catalysts. Their system used an external power source to initially heat the nitrous oxide to the reduced decomposition temperatures. The heat released from decomposition maintains the catalysts at high temperatures, which then further drives the dissociation of nitrous oxide. Eventually, the system reaches steady state and the power source is no longer required, achieving self-sustained decomposition. However, monopropellant thrusters that employ catalysts face a variety of limitations that can affect efficiency and performance due to their inability to withstand decomposition temperatures. Thermal degradation results in deactivation of catalytic active sites (effective surface area available), important for reducing activation energies. This actively impacts thruster performance and therefore is detrimental to a thruster's lifetime [3, 5, 6, 9].

1.2   Project Overview

Monopropellant thrusters that do employ catalysts require a high effective surface area [10–13]. This is to ensure that decomposition of nitrous oxide and any monopropellant in general occurs at a high efficiency at the reduced temperatures. However, any degradation of the catalyst due to high temperatures decreases the effective surface area and therefore is catastrophic for monopropellant system

performance.

As an alternative to catalysts, this work proposes using high temperature porous heat exchangers in order to try and eliminate the huge dependance on the active surface area for decomposition. The approach involves preheating a heat exchanger close to thermal decomposition temperatures. This allows initial nitrous oxide flowing through the channel to decompose and release thermal energy into the heat exchanger. Using a metal with strong heat transfer properties will allow the material to both maintain at a high temperature without an external power source as well as help decompose incoming cold nitrous oxide gas. The rest of the thermal energy will be carried out by the products of nitrous oxide decomposition which, can then be converted into kinetic energy using a nozzle. Fig. 1.1 captures the main heat transfer mechanisms of this approach.
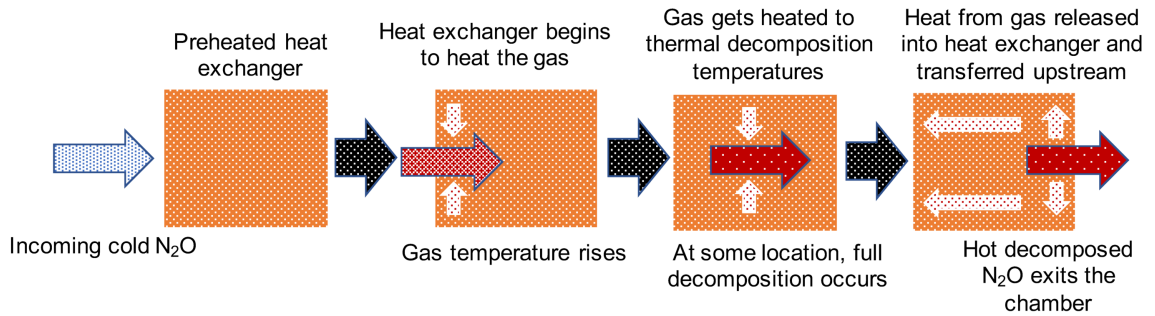
Figure 1.1: Steady-state decomposition of nitrous oxide using heat exchangers

Nitrous oxide decomposition (following $N_2O \rightarrow N_2 + \frac{1}{2}O_2$) has been documented to release a net energy of 82 $\frac{kJ}{mol}$. A closer look shows that it requires 161 $\frac{kJ}{mol}$ to break apart a mole of nitrous oxide (triple bond between the nitrogen and oxygen). The energy release stems from the single oxygen molecules combining to form diatomic oxygen. The bond energy for diatomic oxygen is tabulated to equal

4

498 $\frac{kJ}{mol}$, resulting in the net energy stated above [8].

Before moving forward, it is beneficial to conduct a simple thought experiment on the potential feasibility of this approach. In order to utilize a heat exchanger to help decompose nitrous oxide, it must contain enough energy to decompose incoming nitrous oxide. Contrary to what would be expected, the amount of energy that must be stored within the metal is much lower than what is required to break apart a nitrous oxide molecule. It is primarily dependent on the rate of reaction describing nitrous oxide decomposition. The rate of reaction dictates how much a gas must be heated before the reaction becomes unstable and yields to a runaway decomposition. A more thorough discussion on the rate of reactions can be found in a subsequent chapter. For now, it is sufficient to assume the rate of reaction for decompositions becomes non-negligible only at temperatures greater than 850-900 K [8]. Therefore, the heat exchanger must be preheated to temperatures above that (greater than 1000 K) to guarantee decomposition of nitrous oxide. The energy required to heat cold nitrous oxide to 1000 K (in the ideal case) can easily be calculating using its specific heat capacity. Similarly, this is the amount of energy that the heat exchanger must deposit to achieve decomposition. At steady-state, energy taken from the heat exchanger will be replenished from the hot, decomposed nitrous oxide gas. Assuming a flow of 300 K nitrous oxide with a constant specific heat capacity of 880 $\frac{J}{kg-K}$ and full expansion where all thermal energy can be converted to kinetic energy, 211 seconds Isp can be achieved

1.3 Objective

The objective of this work can be divided into two sections. The first is a numerical model designed in order to capture all fluid and heat transfer properties of this approach using a metal foam as the heat exchanger. The second will demonstrate the viability of this approach in a controlled experiment using different heat exchangers.

1.3.1 1-Dimensional Numerical Heat Transfer Model

The numerical model aims to simulate nitrous oxide steady-state decomposition using a preheated copper metal foam. The model employs heat transfer and rate equations to capture a one-dimensional temperature profile of the gas and foam. A wide parameter space is studied to document the effects of flow parameters and foam specifications on self-sustained decomposition. Furthermore, simulations were extended to other high temperature metal foams, each with different thermal properties. The development of the model and results from simulations have been published in Ref. [14].

1.3.2 Decomposition of Nitrous Oxide in Various Heat Exchangers

In order to substantiate the results from the model, an experimental decomposition chamber was fabricated inside a vacuum bell jar system. Three different heat exchangers, copper metal foam, copper discs, and stainless-steel discs, were tested for nitrous oxide decomposition. All three heat exchangers were first pre-

6

heated to temperature above 1073 K using an contactless inductive heating system. The results will be disseminated to the Journal of Propulsion and Power.

1.4   Contributions

This project describes and demonstrates a novel approach for decomposition of nitrous oxide. It provides a robust one-dimensional numerical model to simulate decomposition of nitrous oxide within a metal foam. A vast parameter space is studied to understand the effects of fluid and thermal properties on nitrous oxide decomposition. The experiment cements the approach as feasible, proving decomposition is possible using a preheated heat exchanger. The overall contributions can be summarized into three categories:(i) trade study on the effects of various heat exchanger and system properties, (ii) development of an inductive heating system capable of heating metals to high temperatures and (iii) self-sustained decomposition tests of nitrous oxide using various heat exchangers. Fig. 1.2 summarizes the contributions of this work.

CONTRIBUTION #1

Trade Study On Heat-Exchanger Properties

Development:

- Numerical model specific to the experimental setup
- Validation against a previous work in literature

Results:

- Effects of heat-exchanger properties on decomposition:
  - Effective Surface Area
  - Gas velocity
  - Gas density
  - PPI/Pre-heat temperature
  - Material type

CONTRIBUTION #2

Inductive Heating System for Pre-Heating

Development:

- Tested different COTS circuits
- Tested different housing materials
- Identified parameters that affect heating efficiency

Results:

- Successfully pre-heating decomposition chambers to >1100 K

CONTRIBUTION #3

Self-Sustained decomposition using heat-exchangers

Development:

- Testing different heat-exchanger setups (vary in material, surface-area properties)
- Studied oxidation effects due to high temperatures

Results:

- Decomposition results from different heat-exchangers
- Mitigating oxidation effects

Figure 1.2: Contributions of this work

Chapter 2:   State of the Art

2.1   Monopropellant Thrusters

Chemical propulsion systems use a variety of fuels to generate the energy required to produce thrust for a spacecraft. Propellants, defined as the reaction masses that provide the forward momentum for a given spacecraft, arise from any fuel that has undergone chemical or thermodynamic changes. They are expelled out of a converging-diverging nozzle, converting the inherent thermal energy into uniform kinetic energy. There are various chemical systems characterized based on the propellants they use. Two of the most popular systems are bi-propellant and monopropellant systems. Bi-propellant systems employ two liquids, a fuel and an oxidizer, that are stored in separate containers and mixed outside a combustion chamber. The fuel and oxidizer can either be hypergolic (spontaneous ignition upon contact) or non-hypergolic (require an ignition source).

Monopropellant systems, on the other hand, do not require a separate oxidizer. The systems generate thrust by decomposing monopropellants with the aid of a catalyst. Although not as efficient (specific impulse is not as high) as other propulsion technologies, they provide a level of simplicity (lower mass) and reliability that cannot be found with other high impulse systems. Due to these reasons, monopro-

pellant systems are almost always selected over other propulsion systems, including bi-propellant systems, for attitude control and on-orbit maneuvering. [15–17]. Major corporations such as Aerojet-RocketDyne, ArianeGroup, Busek and Northrop Grumman all have their own versions of monopropellant thrusters for commercial purchase. Most of them are stated to be flight-tested (on their respective websites) and can offer different degrees of performance based on mission requirements. The thrusters' performance from each vendor are similar to one another, varying only to a small degree based on propellant and other system parameters.

2.1.1 Operation

Monopropellant thrusters can ignite their fuel thermally or use a catalytic bed to decompose the fuel at lower temperatures (catalysts lower activation energies of reactions) [15]. There are several characteristics that come into play when designing a monopropellant thruster. Ignition time-scales (the rate of decomposition, heating time of catalysts) play a role in determining whether a propellant is viable for monopropellant systems. Attitude-control and station-keeping of satellites require quick responses, resulting in engineers minimizing ignition delay as much as possible. Thruster life is also a cause for concern in monopropellant thrusters, especially the ones that use a catalyst bed. Catalysts have temperature limits that can be surpassed by the decomposition of exothermic propellants, resulting in loss of efficiency within the catalyst. This degradation of catalysts and the impact on performance is a major issue for current thrusters [5, 6, 17].

The decomposition products of any fuel in monopropellant thrusters have a maximum energy release that limits the specific impulse. In further discussions on monopropellants used, it will be shown that specific impulses of monopropellant thrusters are typically around 200 seconds. In order to increase the performance of these thrusters, it is possible to augment them with a second-stage that further heats the products before expansion. Some methods by which this can be achieved involve using resistojet and arcjet thrusters. Resistojet thrusters heat the gas using electrical energy and can potentially increase the specific impulse past the 300 second barrier. Arcjet thrusters function by creating a plasma arc between an anode and cathode through which decomposed propellant passes. This heating can increase the specific impulse of monopropellant thrusters up to 600 seconds [17].

2.1.2   Catalysts

Exothermic decomposition for most monopropellants is achieved via a process known as catalysis. Heterogenous catalysis, when the catalysts are of a different phase (typically solid) than that of the propellant, allows monopropellant thrusters to achieve impulses greater than that of cold gas thrusters (e.g expansion of cold nitrogen gas). The main purpose of using a catalyst is to increase the rate of a reaction for decomposition by reducing the activation energy required. Fig 2.1 qualitatively shows how they function.

Heterogenous catalysis occurs due to elements being adsorbed onto the catalyst surface. Figure 2.2 shows catalysis for nitrous oxide, where the oxygen molecules are

11
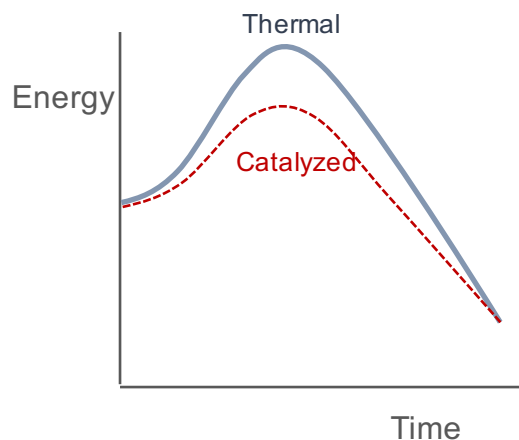
Figure 2.1: Reduction of activation energy when using catalysts

attached onto the catalyst surface. This process reduces the energy of the adsorbed

oxygen and places them in closer proximity to each other, increasing the rate of

reaction for decomposition [18–20].
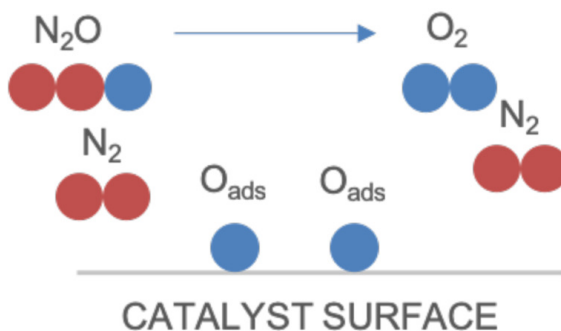
Figure 2.2: N_2O catalysis

Because catalysis involves the active surface available on the catalyst, it is

important to identify the amount of surface area available, especially for decompo-

sition. One parameter used to quantify it is the effective surface area (σ), typically

represented as the surface area available per mass or per bulk volume. Because

catalysts are heavily characterized by the amount of surface area available, they are

usually either finely divided metal or are granules dispersed over a carrier, known

as a support catalyst. Transition metals are typically used as catalysts for oxidizing reactions and are the general candidates for monopropellant decompositions [21].

Catalysts that are exclusively made up of a finely divided metal (active catalyst) are called "non-supported" metal catalysts. A variety of methods exist to prepare these catalysts depending on the metal used. Depending on the exact method and metal, typical sigma values range from 1 - 80 $\frac{m^2}{g}$ [21]. Although non-supported catalysts can help significantly reduce the activation energy for a given reaction, it is necessary to increase the active surface area available to increase efficiency, especially for monopropellant thrusters where performance is proportionally related. This is done by synthesizing small metal crystallites (active catalyst) and attaching them to a support that is thermally stable and has a high effective surface area (most common are SiO_2, Al_2O_3, C and TiO_2) [22]. Typical values of effective surface area are on the order of 100 $\frac{m^2}{g}$ with the aid of support catalysts [10–13].

The biggest obstacle faced when using catalysts for decomposition is the degradation of the metal due to a number of mechanisms, all of which lead to a reduction in the performance of thrusters. Regardless of the propellant used, thermal degradation can lead to loss of mass and active catalytic surface area [23, 24]. As mentioned above, this reduction makes it more difficult for any propellant to decompose, resulting in either an increased preheating temperature or a reduction in thruster performance. The discussions below will delve further into more specific cases of catalyst degradation for various propellants.

2.2 Current Monopropellants

There have been various monopropellants tested throughout the history of spaceflight. The following sections will focus on two extensively researched liquid propellants and their development towards the current state of the art. The discussion will then branch off into other more recent green monopropellants.

2.2.1 Hydrazine

Hydrazine (Anhydrous Hydrazine, N_2H_4) is, without question, the most popular monopropellant used today. It has been utilized in countless missions and is the go-to standard for monopropellant thrusters since the early 1960's. It can be used in tandem with an oxidizer in a bi-propellant system or used alone with a catalyst in a monopropellant system [25]. The decomposition of hydrazine is exothermic, following the reaction $3N_2H_4 \rightarrow 4(1-x)NH_3 + (1+2*x)N_2 + 6*xH_2$, where x is the degree of ammonia dissociation and is a function of catalyst type, size and geometry. Although intermediary reactions lead to hydrogen and ammonia (this step is exothermic), the ammonia further decomposes into hydrogen and nitrogen, as shown above. Ammonia decomposition is endothermic and therefore it is desirable to limit its degree of formation [17].

It was first used on the *Able-4* lunar spacecraft in 1959 and later on in the *Titan 1* vehicle. It further skyrocketed to popularity with the development of the Shell 405 catalyst in the late 1960s, reducing the difficulty to reach hydrazine decomposition [16,25]. At the time, it was the only liquid that was able to decompose

14

efficiently and offer specific impulses better than cold gas thrusters. Because of its head start over other viable propellants and acceptance in the space community, vendors focused on developing their respective space hardware to complement hydrazine. Therefore, a large amount of monopropellant thrusters have become flight qualified, furthering the propellant's appeal to mission designers that want to minimize flight risk on hardware not thoroughly tested in space. Hydrazine has been used on numerous missions during the past couple of decades including *Landsat 3, High-Energy Astronomy Observatory System (HEAO), Viking, Voyager, Magellan, Curiosity*, and *Mars Reconnaissance Orbiter (MRO)* [17]. Although a strong hydrazine infrastructure has cemented within the monopropellant thruster community, a few disadvantages have sparked interest for its replacement [25].

2.2.1.1   Toxicity/Handling

The toxicity of hydrazine has proved to be a paradox in space propulsion, as finding a replacement propellant with the same performance benefits without the hazards of hydrazine is difficult. Hydrazine is classified as toxic with at least a level 3 in health, fire and reactivity by the National Fire Prevention Association (NFPA) in the United States, where anything above level 3 could upon exposure result in a permanent debilitating effects. Some symptoms that occur with hydrazine exposure are eye/nose/throat irritation, blindness, headaches, nausea, seizures and coma. It can also damage organs as well as the central nervous system, and result in dangerous chemical burns when in contact with skin. Researchers have classified

it as a carcinogen and have shown it to cause cancer in humans upon exposure. The severity of these effects is dependent on chemical concentration as well as the time-duration of the exposure [25]. LD50 (Lethal Dose for 50% of a Population) is a metric used to define the dose of a substance ingested orally per unit mass of a subject that would result in the death of 50% of an administrated population. Hydrazine has an LD50 of 60 $\frac{mg}{kg}$ [26]. To compare, aspirin has an LD50 $\frac{mg}{kg}$ of 200 where as arsenic has an LD50 of 15 $\frac{mg}{kg}$.

The material safety data sheet (MSDS) for hydrazine typically asks for a full suit with a face shield and respirator (a large spill requires a full self-contained breathing apparatus). Current safety standards require self-contained hazardous material suits (e.g. SCAPE) and extra procedural steps, resulting in increased costs for the mission. Fueling procedures for hydrazine are complicated, requiring non-vital personal to leave the immediate area. Marshall et al. [25] conducted a comprehensive review on the dangers of hydrazine in 2013, including various studies on the potential costs of transport of hydrazine. Results showed cost reductions are possible with the elimination of both dedicated ground support equipment (GSE) and support personel devoted to proper handling of hydrazine. A large fraction of costs arise with any packing and shipping of hydrazine, where the policies of country-specific transportation policies must be adhered to. The Department of Transportation (DOT) classifies hydrazine into packaging group 1, the highest group for corrosive packages, requiring specialized handling. Furthermore, hardware corrosion and other hazardous material handling equipment negatively affect the cost as well [25].

2.2.1.2   Performance

Hydrazine monopropellant thrusters are generally capable of producing 230 seconds specific impulse [4,15,17,27]. Monopropellant systems that employ catalysts usually have a minimum temperature that the catalyst must be preheated. Lower catalyst preheat temperatures are always desirable as this would reduce the overall power required for satellite systems. The Shell/S-405 catalyst (further enhanced by Aerojet), is an iridium based catalyst capable of spontaneously igniting decomposition, thereby removing the need to add any preheater to the thruster [25, 28]. This helped enable the hydrazine monopropellant era even further. Furthermore, augmented monopropellant thrusters (discussed above) have been shown to significantly increase specific impulse of hydrazine thrusters. Starting from a monopropellant hydrazine thruster using the Shell catalyst (230 seconds), a second-stage resitojet (electrothermal thruster that directly heats the propellant) can be added to increase the specific impulse to 300 seconds. Another example of augmentation is the Secondary Combustion Augmented Thruster (SCAT), which essentially creates a bi-propellant thruster as part of the second-stage [27]. The application would involve mixing in a hypergolic oxidizer (nitrogen tetroxide, N_2O_4) to increase the specific impulse to 315 seconds. Furthermore, the specific impulse could be doubled to 600 seconds using an arcjet as a second stage.

2.2.2 Hydrogen Peroxide

Hydrogen peroxide, one of the oldest propellants, was a monopropellant that was studied extensively before being replaced by hydrazine due to better performance. In recent years, it has regained momentum as a monopropellant and bi-propellant once again as a means to escape the consequences of hydrazine's toxicity [29–31]. It is a high density liquid that can exothermically decompose into steam and oxygen, following the reaction $H_2O_2 \rightarrow H_2O + \frac{1}{2}O_2$, resulting in specific impulses up to 180 seconds or about 20% less than that of hydrazine [4, 32, 33]. Because its decomposition generates oxygen, it was also classified as an oxidizer for other systems, but was quickly replaced by liquid oxygen (cryogenic) and nitrogen tetroxide (compatibility with hydrazine) [33–35]. Operation of hydrogen peroxide thrusters typically involved the use of catalytic beds to decompose the propellant.

Although the discovery of hydrogen peroxide predates the 19th century, its use as a rocket propellant began during the 1930's. Initial work was conducted by Hellmuth Walter, who was the first to use 80% concentration of hydrogen peroxide as a propellant. He worked on developing variants of hydrogen peroxide for both mono- and bi-propellant engines. He classified two different variations of hydrogen peroxide decomposition. One being simply to use the hot decomposition products as exhaust through a nozzle, whereas the other involved firing fuel into the hot oxygen, combusting the mixture and then expanding the propellant through the nozzle. This effectively doubled the specific impulse [33, 35]. During the 1960's, a lot of research was focused on hydrogen peroxide decomposition, enabling it to be used in

reaction control systems (RCS) of early *Mercury* and *Gemini* manned spacecrafts. Its popularity was primarily due to a lack of an effective catalyst for hydrazine decomposition. Once Shell 405 was developed, research efforts diminished [32, 33].

Frequent materials for catalytic beds when decomposing hydrogen peroxide are usually metallic silver or manganese oxides [32]. Renewed interested in hydrogen peroxide is mostly directed towards addressing catalyst deactivation due to poisoning and oxidation. Researchers have found these effects to significantly reduce performance [36]. Significant work has been focused towards developing new catalytic beds [13, 32, 37, 38] and studying the effects of certain system parameters on performance [39–41]. Other scientists focused on developing different versions of hydrogen peroxide, especially ones that have increased stabilizers to remove strict constraints on handling and storage of hydrogen peroxide [35]. An et al. [29] studied instabilities that occur within H_2O_2 monopropellant thrusters. Dongwook et al. found preheating catalysts up to certain temperatures significantly improves decomposition times [11]. Numerical models have been developed to study hydrogen peroxide flow over catalytic beds, focusing on pressure drops that might impact performance [31].

2.2.2.1 Advantages Over Hydrazine

As mentioned above, the performance offered by hydrogen peroxide is lower than hydrazine. However, due to its high density, it boasts a higher volumetric specific impulse. This makes it highly appealing for missions that have stringent

volume constraints [32]. Its ability to be a liquid oxidizer makes it a unique propellant, capable of being used in either mono- or bi-propellant thrusters. Furthermore, its low vapor pressure makes it easier to have lower inlet pressures when used as either a monopropellant or an oxidizer [33]. Lastly, it is much more cost effective to purchase than hydrazine in both low (70%) and high (99%) purity [26].

The biggest advantage of using hydrogen peroxide over hydrazine, however, has to do with the toxicity of propellants. First, hydrogen peroxide's decomposition products consist of steam and oxygen, posing no threat to the environment [32,33]. Second, hydrogen peroxide is considered non-toxic as its effects on humans are less severe since the human body naturally decomposes H_2O_2 (compared to hydrazine). For low exposure to skin, this results in small white spots that will go away within a few hours. More aggressive exposures will, however, result in blistering on the skin [42]. Its low vapor pressure makes it difficult to be inhaled (for an exposed liquid surface) [33]. Its LD50 is much higher than hydrazine, approximately 805 $\frac{mg}{kg}$ and its classification according to NFPA is less severe than hydrazine, with a level 3 for health, level 0 for fire and level 1 for reactivity [26].

However, although not poisonous, it is important to note that its vapors are an irritant to the eyes and long term exposure (8 hours, 1.0 ppm) can cause permanent damage [27]. Similar to hydrazine, personal protective equipment (PPE) is also required when handling hydrogen peroxide. Although not as severe, the PPE associated with hydrogen peroxide involve non-absorbing water resistant clothes, gloves, boots and eye protection to ensure no accidental catalytic decomposition occurs [42].

2.2.3 Green Monopropellants

Being the standard monopropellant for attitude and spacecraft control for over 45 years is a testament to how difficult it is to replace hydrazine. It asserts the fact that being green or less toxic is simply not enough to overrule the importance of other characteristics such as propellant performance. Hydrogen peroxide, for example, failed to gain traction against hydrazine because it was unable to compete with its superior performance. Furthermore, hydrazine's great track record in safety only substantiates the argument that the "greenness" of a propellant needs to also account for the the costs of safety and proper handling [27].

Numerous space agencies and other government-funded organizations (European Space Agency (ESA), National Aeronautics and Space Administration (NASA), Air Force Research Laboratory (AFRL), Swedish Defense Research Agency (FOI) and Japan Aerospace Exploration Agency (JAXA)) are interested in developing green propellants. Their support allowed many researchers to focus their efforts on developing numerous monopropellants aimed at replacing hydrazine. In order to provide an effective alternative to hydrazine, the performance of green propellants must be somewhat comparable (within 15%), it must reduce costs pertaining to handling/transportation and accident avoidance, and it must provide for potential augmentation for increased performance (bi-propellant thrusters, arcjet, etc). The following will discuss the developments and current state of some green monopropellants [27].

2.2.3.1 Classification of "Green"

Although the toxicity of two well-researched propellants was discussed, the actual interpretation of what is considered green has yet to be defined in this study. Phrases such as "green" or "non-toxic" have been used across literature to describe various propellants, but no standard definition or criteria have ever been set in place.

Sackheim et al. [27] and Marshall et al. [25] have thoroughly researched hydrazine and have stated strict guidelines for toxicity that must be addressed in order to be classified as green. The criteria they developed has a strong foundation thanks to their extensive experience in handling monopropellants and are used as the classification tools for this work. A summary of their requirements are shown in Table 2.1. These general requirements can be used to baseline current and new monopropellants. The following sections will detail the main candidates for a green alternative propellant. Although some may not fully qualify based on the requirements outlined in Table 2.1, it is important to consider them as they are still strong candidates.

Table 2.1: Guidelines for green classification of monopropellants

1. Toxic rating less than 3 for all categories on the NFPA diamond
2. Propellant classified as a non-carcinogenic and non-mutagenic
3. Minor environmental impact
4. Elimination of any personal protection equipment (PPE)
5. Ease of transport (packaging group 2 or 3 classification by DOT)

2.2.4 Ionic Liquids

According to Amir et al. [43], the candidates (other than hydrogen peroxide) for green propulsion that have had the most traction in recent years are ionic liquids and nitrous oxide fuel blends. Since this work focuses on the latter, it is beneficial to first explore ionic liquids and the various fuels that have demonstrated promising results. Monopropellants using ionic liquids are typically a mixture of an ionic liquid (salt with a melting point below 100° C), fuel and water. The three listed below do not meet all the requirements outlined in Table 2.1, but nonetheless are still frontrunners due to their potential to provide better performance than hydrazine.

2.2.4.1 Ammonium Dinitramide (ADN)

ADN, $(NH_4N(NO_2)_2)$, is an explosive solid white salt with an LD50 of 823 $\frac{mg}{kg}$. It is considered a non-allergenic and non-carcinogenic with no irritation upon contact with eyes and skin. It is, however, considered both a mutagenic and teratogenic and harmful if swallowed. ADN was first developed as a classified propellant in the Soviet Union before being rediscovered in the early 2000's [43, 44]. ADN thermally decomposes at around 400 K but has been shown to decompose on a copper oxide catalyst (with pre-heating) around 315 K [45]. In 2010, the fuel blend LMP-103S consisting of ADN, water, methanol and ammonia was successfully demonstrated on *PRISMA*, delivering specific impulses up to 250 seconds. Since then, the Swedish Space Corporation successfully developed a 5N and a 22N thruster to TRL 5 and are currently working on 50N and 200N thrusters. Furthermore, a higher performing,

ADN based propellant has been developed using a nonvolatile fuel known as FLP-106 [27]. It is worth mentioning, however, that recent progress has been plagued with high costs for dedicated manufacturing. Currently, the EU Horizon2020 project *RHEFORM* is working on developing ADN based propellants to replace hydrazine. Focusing on LMP-103S and FLP-106 as baseline propellants, its objectives are to address the high combustion temperatures (1903 K as opposed to hydrazine's 1173 K) by varying water content within the propellants and to develop new catalysts that would require less pre-heating [46].

2.2.4.2   Hydroxylammonium Nitrate (HAN)

Developed by the Air Force Research Laboratory (AFRL) in 1998, HAN, (NH_3OHNO_3), is a highly soluble ionic liquid that can be used to create high performance propellants. Similar to ADN based propellants, propellants using HAN derive their low-toxicity due to low vapor pressure and pose no environmental issue (still require PPE equipment) [43]. Its thermal decomposition occurs around 428 K but can be reduced to 325 K when utilizing a preheated iridium based catalyst [45]. A 1N and a 22N thruster using the AF-M315E blend (a HAN, water, and hygroscope fuel mixture), have been in development for NASA's Green Propellant Infusion Mission (GPIM) since 2015 and are expected to produce 250 seconds specific impulse. The two month long mission is scheduled for launch sometime in 2019 [27,47]. Another fuel blend labeled SHP163, a mixture of HAN, ammonium nitrate, methanol and water, is being developed by JAXA [48].

2.2.4.3 Hydrazinium Nitroformate (HNF)

HNF,$(N_2H_5C(NO_2)_3)$, was initially discovered in 1951 but gained more traction as a propellant when it was studied in the early 1990's at Prins Murits Laboratory in the Netherlands. Their research led to the development of the $HNF - H_2O$ mixture, which can achieve higher specific impulses than hydrazine [49, 50]. It has been experimentally shown to catalytically decompose on iridium, rhodium and platinum based catalysts at low temperatures, given the catalysts are preheated to around 375 K [49, 51, 52]. Unfortunately, its issues with thermal stability, sensitivity and compatibility weigh it down as a candidate for replacing hydrazine (compared to ADN and HAN based propellants). Furthermore, it is synthesized using hydrazine, which brings into question whether it should still be considered green [43, 53].

2.3 Nitrous Oxide

Nitrous oxide has been researched for quite some time for its properties as an oxidizer and as a green monopropellant [43]. Both the British and the Germans focused on using nitrous oxide as an oxidizer for military purposes in the early 1930's. Unsuccessful, interest in nitrous oxide gained traction again in the 1950's after a study on its usability as a monopropellant was commissioned by the National Advisory Committee for Aeronautics (NACA). The results, although positive, did identify its need for high initiation temperatures. There was sporadic research in the 1990's on its utility as an oxidizer, but research on utilizing it as a monopropellant began at Surrey Satellite Technology Ltd (SSTL) in 1996 [7]. Their work led to

the launch of *UoSAT-12*, a micro satellite using a nitrous oxide thruster with a self-pressuring feed system [54]. University of Surrey continued the development of this technology, focusing on the limitations presented by the degradation of catalysts [3].

Nitrous oxide decomposition is exothermic, resulting in a net energy release of $82\frac{kJ}{mol}$. Thermal decomposition occurs at temperatures temperatures above 1000 K, with no catalyst available for spontaneous decomposition (on the contrary to hydrazine and hydrogen peroxide). It has been shown that rhodium and ruthenium are the most efficient catalysts for nitrous oxide decomposition, with initiation temperatures around 473 - 573 K. They are typically utilized over a variety of support catalysts such as MgO, SiO_2, CeO_2, Al_2O_3 and TiO_2 [4, 10, 55–57]. Along with meeting all the criteria listed in Table 2.1, added benefits of using nitrous oxide include being able to be stored as a liquid ($\sim$ 52 bar at 300 K) and oxygen generation for augmentation of the thruster via combustion with other fuels [4].

2.3.1 Catalytic Decomposition

Early research at the Surrey Space Center showed their thruster concept achieving self-sustained decomposition using catalysts. It used an external power source to initially heat the LCH 212 hydrazine catalyst before flowing nitrous oxide. Although steady-state decomposition was achieved, researchers experienced catalyst degradation at high temperatures, which therefore limited thruster performance [3,54]. Follow-on efforts by researchers found similar results using various catalysts. A 2014 study developed a 2N thruster prototype employing nitrous oxide gas

decomposing over a rhodium oxide catalyst supported on alumina ($Rh/\gamma - Al_2O_3$). Although a decomposition efficiency of 88% was achieved, a loss of catalyst specific area due to high temperatures was observed [6]. Speaking towards the longevity of the thruster, Chao et al. showed a reduction in decomposition efficiency at a given preheat temperature each consecutive thruster re-fire [56]. Kim et al. studied the endurance and performance of a nitrous oxide system using a ruthenium catalyst supported on alumina oxide ($Ru/\gamma - Al_2O_3$). Results showed a severe loss of specific surface area from 100 $\frac{m^2}{g}$ to 5 $\frac{m^2}{g}$ and a performance reduction of the thruster [10].

In order to address these issues, a majority of current efforts is focused on either identifying new catalysts or modifying system parameters and geometry in order to increase performance and lifetime. Konsolakis conducted an extensive survey on all the advances of nitrous oxide decomposition over non-noble metal oxides [58]. Kevin et al. studied the effect of catalyst bed geometry on decomposition and found no degradation after one hour tests [59]. Beyer et al. quantified the effects of rhodium particle size and metal oxide support on nitrous oxide decomposition. Results showed MgO and SiO_2 being superior oxide supports for rhodium catalysts, leading to decomposition occurring at 573 K [60]. One promising study experimented with $Cu - Zn$ supported on alumina as a catalyst for nitrous oxide decomposition. The catalyst was able to withstand the high temperatures generated and showed no signs of degradation after a 100 hour stability test [61]. Furthermore, mullite-supported Rh catalyst for nitrous oxide decomposition showed strong thermal stability and high catlytic activity [62]. Woo et al. modeled a nitrous oxide catalytic ignitor with metal foam geometry. The study identified various parame-

ters and their effects on thermal performance of the ignitor [63]. Lastly, there has been some interest in developing nitrous oxide as an ignitor for augmented systems. Ref. [64] focused on the feasibility of using nitrous oxide as an ignitor for a hybrid rocket motor.

2.3.2 Catalysis Alternatives

Decomposition of nitrous oxide without the use of catalysts has been studied extensively. Preliminary research conducted by this author focused on achieving decomposition using dielectric barrier discharge (DBD). Results showed an increase in temperature for nitrous oxide versus carbon dioxide when inside a DBD and verified the proof of concept [65]. Kakami et al. created a 1N class thruster using a nitrous oxide/ethanol bi-propellant. The authors were able to successfully achieve arc discharge assisted combustion [5]. Jin-Oh Jo et al. developed plasma-catalytic reactor in which the efficiency was increased by 30% to 50% when compared to pure catalytic decomposition [66]. Galle et al. showed that thermal decomposition of nitrous oxide inside regenerative heat exchange reactors was possible with and without the use of catalysts [67].

2.3.3 Nitrous Oxide Fuel Blends

Nitrous oxide and hydrocarbon fuel blends have been studied since the 1930's with the objective to produce monopropellants with bi-propellant-like performances. However, a large part of this research was abandoned primarily due to safety con-

cerns. Fast forward 70 years, Firestar Technologies developed a family of nitrous oxide and hydrocarbon fuel blends, calling them NOFBX. These blends were able to offer much higher specific impulses than hydrazine [27]. One huge advantage NOFBX offer is the ability to be spark ignited, removing the need for any catalyst or pre-heating. They are classified as non-toxic and their effluents are environmentally friendly. Contrary to ionic liquids, manufacturing costs are also relatively low. A NOFBX thruster has been demonstrated in the 0.4 N to 450N thruster range, with a specific impulse of over 325 seconds [68]. Xuesen Yang et al. developed a model to analyze thermal parameters of nitrous oxide/ethylene blends and their effects on ignition and self-pressurization [69,70]. Although promising, NOFBX still pose a safety hazard since they incorporate hypergolic fuels [71].

Chapter 3: One-Dimensional Numerical Model of Nitrous Oxide Decomposition using a Metal Foam

The numerical model developed in this chapter focuses on the use of a metal foam to help redirect thermal energy released from exothermic decomposition. A metal foam is a porous "sponge" made of metal with empty voids. The foams described in this study are open-cell, where the voids are interconnected, allowing fluid to flow. Open-cell foams are efficient heat-exchangers thanks to their large surface area to volume ratio or effective surface area (σ) [72]. Specifically, this value represents the surface area that is in contact with the fluid per unit volume. In general, a high porosity leads to higher effective surface areas. At constant porosity, σ can be increased by decreasing the pore or void sizes or increasing its roughness [1]. Fig. 3.1 shows an example of a 0.88 inch (22.35 mm) diameter copper metal foam (used later for experimental tests).

This approach takes advantage of the porous structure as well as the thermal properties of the metal foam to reach self-sustained decomposition. By preheating the metal foam to high temperatures (thermal decomposition), the initial nitrous oxide flow will decompose and release thermal energy into the foam. Using a metal with strong heat transfer properties allows the material to both maintain a high

Figure 3.1: Copper metal foam: 0.88 inches diameter, 2.5 inches long

temperature without an external power source as well as help decompose incoming cold nitrous oxide gas. The rest of the thermal energy will be carried out by the products of nitrous oxide decomposition which can then be converted into kinetic energy using a nozzle. Please note that from now on, the metal foam will be referred to as the porous block.

3.1 Derivation of 1-D Equations

The numerical model is divided into three sections; the first and second sections are directed towards capturing all the potential heat transfer paths that are significant for the gas and the block respectively. The third section solves for the change of nitrous oxide density.

All of the terms in the following heat balance equations are defined as volumetric power terms $\left(\frac{W}{m^3}\right)$. The system is treated as compressible in order to account for large changes in flow properties due to decomposition. To maintain consistency among all equations, flow is assumed to be positive to the right with all source terms positive when depositing energy into that respective system. Furthermore, viscosity

effects and body forces are ignored due to the low velocities considered here. Although the focus of the numerical model is to find a viable steady-state solution, the exponential nature of the rate of nitrous oxide decomposition makes implementing any implicit scheme difficult. Therefore, starting from initial conditions, the model evolves the transient solution until it reaches the steady-state.

The governing equations for gas temperature, block temperature and change in gas density are all derived from the conservation laws shown below [73,74].

$$
\frac{\partial \rho}{\partial t} + \nabla \cdot (\rho \, \vec{u}) = 0
$$
$$
\frac{\partial (\rho \, \vec{u})}{\partial t} + \nabla \cdot (\rho \, \vec{u} \otimes \vec{u}) = -\nabla p_g - \vec{F_b} \tag{3.1}
$$
$$
\frac{\partial (\rho \, (h_g + \frac{1}{2}\, u^2) - p_g)}{\partial t} + \nabla \cdot (\rho \, (h_g + \frac{1}{2}\, u^2)\, \vec{u} + \vec{j_c}) = \dot{Q}
$$

Although a $\frac{\partial}{\partial t}$ term is necessary to evolve the system in time, not all terms need to be time-dependent as long as steady-state is eventually achieved. Therefore, in order to simplify the analysis, total gas density is assumed to be constant in time (conservation of mass), anchoring a set mass flux throughout a 1-D constant-area channel represented by the simulation's spatial domain. Furthermore, this also removes the time derivative in the momentum equation for a constant-area channel.

$$
\rho \, \frac{\partial h_g}{\partial t} + \frac{\partial \rho}{\partial t}\, (h_g + \frac{1}{2}\, u^2) + \rho \, u \, \frac{\partial u}{\partial t} - \frac{\partial p_g}{\partial t} + \nabla \cdot (\rho \, (h_g + \frac{1}{2}\, u^2)\, \vec{u} + \vec{j_c}) = \dot{Q} \tag{3.2}
$$

The driving term for the transient evolution comes from the energy equation (Eq. (3.2)), specifically an explicit change in enthalpy term after using the product

rule to separate the time derivative terms. The remaining $\frac{\partial}{\partial t}$ terms in the expanded energy equation above can be neglected since only the steady-state solutions are of interest.

It should be noted that a one dimensional approximation of the flow channel can have some impacts on the flow-regime and temperature. The flow through the porous medium in this study has a Reynolds number of order unity (verified in a later section) and therefore follows Darcy's law which states that the fluid's bulk resistance is only linearly proportional to the flow velocity [1]. Tahiri [2] showed that for relatively low Reynolds numbers, the laminar boundary layers extended only up to 9% of the foam's transverse length. These boundary layer regions, which are not captured within the model, can have some impact on the heat transfer between the block and fluid. Furthermore, the 1-D model assumes no temperature variations along the radial axis of the foam, which isn't necessarily the case. Experiments conducted with copper foam showed temperature variation of up to 7% from the outer wall to the center of the foam. These variations can become more pronounced with either an increase in fluid velocity or a decrease in thermal conductivity [1,2].

3.1.1 Thermal Equations for the Gas

The governing equation for gas temperature must capture conduction ($\nabla \cdot \vec{j_c}$) across the gas, advection due to the bulk fluid flow ($\nabla \cdot [\rho (h_g + \frac{1}{2} u^2) \vec{u}]$) and the volumetric source terms due to decomposition ($\dot{Q}_{dcp}$) energy release and block heating ($\dot{Q}_{blk}$). In Eq. (3.2), while the advective and conductive heat transfer modes

are captured within the divergence, the rest of the heat transfer paths are contained within the $\dot{Q}$ term as a linear combination. After removing all $\frac{\partial}{\partial t}$ terms except the driving $\rho\,\frac{\partial h_g}{\partial t}$ term and defining $\vec{j_a} = \rho_{gas}\,\vec{u}\,(h_g + \frac{1}{2}u^2)$, the energy equation for gas temperature is shown in Eq. (3.3).

$$\rho_{gas}\,\frac{\partial h_g}{\partial t} + \nabla \cdot (\vec{j_a} + \vec{j_c}) = \dot{Q}_{dcp} + \dot{Q}_{blk} \tag{3.3}$$

Heat transfer due to conduction follows Fourier's law, where $\vec{j_c} = -k_{gas}\,\nabla\,T_{gas}$. Assuming k_{gas} is constant, $\nabla \cdot \vec{j_c}$ is then equal to $-k_{gas}\,\nabla^2\,T_{gas}$. The divergence of $\vec{j_a}$ however, is not as straightforward and requires auxiliary derivations from the steady-state momentum equation to solve. In a 1-D channel, an ideal scenario would have nitrous oxide decomposing at some location along the channel. As the gas temperature changes, so will its velocity, resulting in a variable resistance the fluid encounters as it travels through the porous material. This resistance, which can be described as a friction term $\vec{F_b}$, should scale inversely with porosity of the metal foam and is treated as an external force as shown in Eq. (3.4). The procedure on how to approximate $\vec{F_b}$ (via Darcy's law) will be shown later in the paper.

$$\nabla \cdot (\rho\,\vec{u} \otimes \vec{u}) = -\nabla p_g - \vec{F_b} \tag{3.4}$$

In 1-D, Eq. (3.4) reduces to the following:

$$u^2\,\frac{\partial \rho_{gas}}{\partial x} + 2\,u\,\rho_{gas}\,\frac{\partial u}{\partial x} = -\nabla p_g - \vec{F_b} \tag{3.5}$$

To simplify the equation, one can take the derivative of the mass flux equation and multiply it by u. It is also helpful to display the 1-D gradient of the ideal gas equation.

$$-u^2 \frac{\partial \rho_{gas}}{\partial x} = \rho_{gas} u \frac{\partial u}{\partial x}$$

$$\frac{\partial p_g}{\partial x} = \frac{\partial \rho_{gas}}{\partial x} R T_{gas} + \rho_{gas} R \frac{\partial T_{gas}}{\partial x}$$

(3.6)

Substituting Eqs. (3.6) into Eq. (3.5) results in the following expression which can also be further rearranged to solve for the 1-D divergence of velocity.

$$- u^2 \frac{\partial \rho_{gas}}{\partial x} + F_b = -\frac{\partial \rho_{gas}}{\partial x} R T_{gas} - \rho_{gas} R \frac{\partial T_{gas}}{\partial x}$$

(3.7)

$$\frac{\partial u}{\partial x} = (\frac{u}{\rho_{gas}}) \frac{F_b + \rho_{gas} R \frac{\partial T_{gas}}{\partial x}}{R T_{gas} - u^2}$$

(3.8)

With the divergence of velocity determined, it is now ideal to complete the 1-D divergence of $\vec{j_a}$. Assuming mass flux constant throughout the channel, $\nabla \cdot \vec{j_a}$ is equal to $\rho_{gas} u \frac{\partial (h_g + \frac{1}{2} u^2)}{\partial x}$, which can be expanded using the definition of specific enthalpy as shown below. Note that the specific enthalpy of the gas changes as the concentrations of species change (due to decomposition) and is accounted for within the simulation as a function of temperature and molar concentrations.

$$\nabla \cdot \vec{j_a} = \rho_{gas} u C p_{gas} \frac{\partial T_{gas}}{\partial x} + u^3 \frac{F_b + \rho_{gas} R \frac{\partial T_{gas}}{\partial x}}{R T_{gas} - u^2}$$

$$\text{since } \frac{\partial h_g}{\partial x} = \frac{\partial h_g}{\partial T} \frac{\partial T}{\partial x}, \ C p = \frac{\partial h_g}{\partial T}$$

(3.9)

The left side of Eq. (3.3) is now complete and is written explicitly in Eq. (3.10), with all sources and sinks still represented by $\dot{Q}$. The time derivative of enthalpy can also be changed to an explicit rate of change of temperature using the same technique shown above.

$$\rho_{gas}\,Cp_{gas}\,\frac{\partial T_{gas}}{\partial t} - k_{gas}\,\frac{\partial^2 T_{gas}}{\partial x^2} + \rho_{gas}\,u\,Cp_{gas}\,\frac{\partial T_{gas}}{\partial x} + u^3\,\frac{F_b + \rho_{gas}\,R\,\frac{\partial T_{gas}}{\partial x}}{R\,T_{gas} - u^2} = \dot{Q}_{dcp} + \dot{Q}_{blk}$$

(3.10)

Convective heat transfer $(\dot{Q}_{blk})$ loosely follows Newton's law of cooling (heat flux), expressed as $\dot{q}_{conv} = h\,(T_{blk} - T_{gas})$ where h was approximated for this work and will be explained in greater detail in subsequent sections. This heat flux term can be multiplied by the effective surface area for porous media (σ) to convert it to the required volumetric term. Since the gas and block communicate thermally through the convective term, both governing equations (gas and block) will employ an equal and opposite convective term.

Relatively, the decomposition source term $(\dot{Q}_{dcp})$ is a bit more complicated as it requires a temperature dependent rate of reaction. The decomposition can be considered a falloff reaction and therefore, the rate of reaction is a function of system pressure. Specifically, there is a high pressure reaction rate that is first-order and a low pressure reaction that is second-order (a function of gas density). The falloff decomposition follows the reaction $N_2O + [M] \longrightarrow N_2 + O + [M]$, where $[M]$ is the collision molecule that in this case would include both the products and reactants. In low pressure decomposition, the concentration of $[M]$ plays a crucial role in the

reaction, whereas in high pressure decomposition, the concentration of $[M]$ can be disregarded. There have been numerous low- and high-pressure reaction rates in the literature [8, 75–77] that focused on understanding the kinetics of nitrous oxide decomposition. Differences between these rates were minimal and therefore the rate of reactions used for this work were taken from Ref. [8]. They were able to provide both high pressure and low pressure reaction rates for decomposition of nitrous oxide. Although this simulation is expected to perform in the low-pressure regime, the two rates can be combined using the following relation [78]. The activation energies for the low pressure and high pressure rates are -59,200 $\frac{kcal}{mol}$ and -58,000 $\frac{kcal}{mol}$. Likewise, the pre-exponential factors for the low pressure and high pressure Arrhenius equations are 2.7 x 10^{15} $\frac{cm^3}{sec-mol}$ and 1.3 x 10^{11} $\frac{1}{sec}$.

$$\alpha = \frac{\alpha_0\,[M]}{1 + \frac{\alpha_0\,[M]}{\alpha_\infty}},$$
$$\alpha_0 = 2.7(10^{15})\,\exp(\frac{-59,200}{R_u\,T_{gas}}) \tag{3.11}$$
$$\alpha_\infty = 1.3(10^{11})\,\exp(\frac{-58,000}{R_u\,T_{gas}})$$

The high pressure α is a good approximation inside the temperature range of 900-2100 K whereas the low pressure alpha is valid inside the temperature range of 900-1050 K. Although the temperature might exceed these ranges, the author of this work believes any error resulting from this can be accounted for during experimentation. Furthermore, Ref. [8] also list reaction rates for oxygen recombination, all of which occur more quickly than decomposition due to lower activation energies.

Therefore, the decomposition of nitrous oxide is assumed to be the rate-limiting step and is the only reaction modeled.

By setting $[M]$ to be the molar concentration of the gas within the system (total gas density divided by its molecular weight) when solving for α, a volumetric heat source term for nitrous oxide decomposition can be generated. The density of nitrous oxide is not constant along the spatial dimension and its governing equation will be discussed in the upcoming section. Eq. (3.12) now represents the final heat transfer equation for the gas temperature. Due to some of the time derivative terms being eliminated, the time evolution of the system may not be a realistic representation; however, the steady-state solution should be unaffected provided that only one such solution exists.

$$\rho_{gas} \, Cp_{gas} \, \frac{\partial T_{gas}}{\partial t} - k_{gas} \, \frac{\partial^2 T_{gas}}{\partial x^2} + \rho_{gas} \, u \, Cp_{gas} \, \frac{\partial T_{gas}}{\partial x} + u^3 \, \frac{F_b + \rho_{gas} \, R \, \frac{\partial T_{gas}}{\partial x}}{R \, T_{gas} - u^2}$$
$$= h \, \sigma \, (T_{blk} - T_{gas}) + \alpha \, q_d \, (\rho_{gas} - \rho_{prod}) \tag{3.12}$$

3.1.2 Thermal Equations for the Metal Foam

The derivation for the governing equation for block temperature is very similar to how the gas equation was derived, with the only difference being the source term and the flux terms within the divergence.

Since there is no advection term for the block, the only heat flux is the conduction term $\vec{j_c}$, which just mirrors the one calculated for gas but with block thermal

properties. The source term $\dot{Q}$ contains the equal and opposite convective term $-\dot{Q}_{blk}$, with a positive source always resulting in energy deposited into the block as well as a heat loss term that will be discussed in later sections. This loss term can be set to zero, a non-zero constant, or as a function of gas and block temperature. Therefore, the governing equation for block temperature is shown in Eq. (3.13).

$$\rho_{blk}\, Cp_{blk}\, \frac{\partial T_{blk}}{\partial t} - k_{blk}\, \frac{\partial^2 T_{gas}}{\partial x^2} = h\, \sigma\, (T_{gas} - T_{blk}) + \dot{Q}_{loss} \tag{3.13}$$

3.1.3 Gas Density Equations

Once decomposition initiates within the system, the amount of nitrous oxide available dictates how much decomposition can occur. Since this model follows the irreversible reaction $N_2O \longrightarrow N_2 + \frac{1}{2}O_2$, the percent decomposition that has occurred can be tracked by calculating the amount of products within the system. From mass conservation, the amount of total gas density ρ_{gas} must be equal to $\rho_{N_2O} + \rho_{prod}$. Therefore, full decomposition within the system will have occurred when all of the gas within the system is composed of just the products from the reaction.

$$\frac{\partial \rho_{prod}}{\partial t} + \nabla \cdot (\rho_{prod}\, \vec{u}) = S \tag{3.14}$$

Starting from the continuity equation, the rate at which products are generated is shown in Eq. (3.14), with the source term S being a function of α and ρ_{N_2O}. Carrying out the 1-D divergence, the gas density equation is described below. Here,

39

the divergence does not equal zero since mass flux of product density is not constant.

$$\frac{\partial \rho_{prod}}{\partial t} = -u \frac{\partial \rho_{prod}}{\partial x} - \rho_{prod} \frac{\partial u}{\partial x} + \alpha \left(\rho_{gas} - \rho_{prod} \right) \tag{3.15}$$

-

3.2 System Parameters

Now that the equations have been derived, the next step is to outline some of the parameters that will be design choices or physically approximated.

3.2.1 Friction

To the authors' knowledge, there is no experimental data pertaining to nitrous oxide flow through a porous medium. Therefore, an approximate value was calculated using Darcy's law: $F_b = -\frac{\eta}{K} u$ [1, 79, 80]. The dynamic viscosity of nitrous oxide, η, is known at certain temperatures and is used as a constant for this calculation. K is the permeability of the foam and is used to describe the foam's flow conductance. A high permeability would be analogous to an open pipe with no flow restrictions. Darcy's law is only valid for flow through porous medium at low Reynolds numbers (order unity) whereas at higher velocities, inertial drag becomes more prevalent and the flow resistance is no longer linear with the fluid velocity [1,80,81]. In general, the permeability of the foam is a function of its porosity and pore cell size and calculating a value specific to each foam can be difficult and is outside the scope of this work. Instead, an approximate value can be derived

by assuming each pore is circular and the resistance is uniform across the pore, resulting in the permeability being just the cross-sectional area of a pore.

Consider a porous block of unit cross-section and arbitrary depth, with a porosity (ratio of volumes) of P. By definition the void area is equal to the cross-sectional area multiplied by P. Assuming the borders have negligible thicknesses, this area divided by the total number of pores will provide a cross-sectional area of a pore and thereby the permeability. Given a PPI, the number of nodes along a unit length is known and can be used to find an approximation for the total number of nodes (PPI^2) in a unit cross-section of porous block. The permeability calculated for a 10 PPI foam with a porosity of 86% (this work) is on the order of 10^{-6} m^2 which is within an order of magnitude of similar foams [1, 2, 80, 82, 83].

Lastly, it is important to show that the Reynolds numbers in this study support the use of a linear resistance model (Darcy's law). Given a gas density of 1.8 $\frac{kg}{m^3}$, 0.01 $\frac{m}{sec}$ fluid velocity, a characteristic length of the system of 0.01 m, and a dynamic viscosity of 3.7 x 10^{-5} $\frac{N-s}{m^2}$ (taken from tabulated data), a Reynolds number of $\sim$ 5 was calculated using $Re = \frac{\rho_{N_2O} \, u \, l}{\eta}$. Furthermore, it is applicable to calculate the Reynolds number using the permeability calculated above using $Re = \frac{\rho_{N_2O} \, u \, \sqrt{(K)}}{\eta}$ [1]. This equation yields a Reynolds number of $\sim$ 1.2. Both values are small enough to support the usage of Darcy's law to capture the bulk fluid resistance within porous media. From simulations, it was found that the friction term is in fact weak compared to the heating terms primarily due to the low gas velocities and has little impact on the flow.

3.2.2 Heat Loss

Shown in Eq. (3.13), there is a heat loss term $\dot{Q}_{loss}$ that can be set based on the experimental setup. For this work, the block is placed inside a steel sleeve which is then wrapped by insulation, as shown in Fig. 3.2 (not drawn to scale). The 1-D equations solve for the temperature profiles axially at the centerline, with heat loss calculated radially at each axial step. In vacuum, the radial heat is conducted across the steel and insulation and is equal to the radiative heat loss emitted from the insulation's outer surface. For all simulations, the steel sleeve's dimensions were set to an outer radius of 9.5 mm with a thickness of 3.4 mm in order to match commercially sold steel tubes. The insulation radius was set to at least three times the radius of the steel in order to mitigate heat loss.
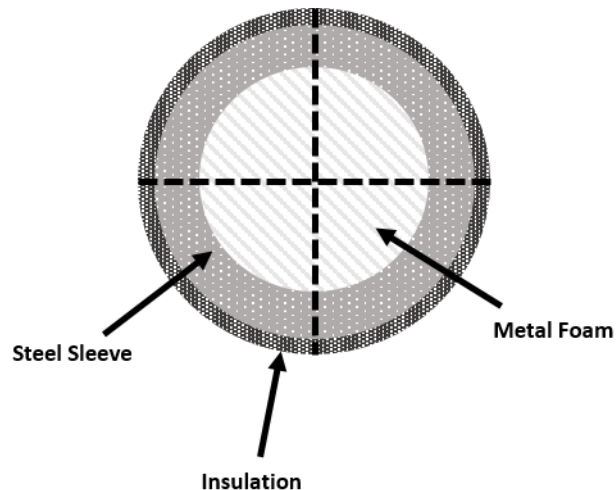
Figure 3.2: Cross-section of the metal foam, steel sleeve and insulation.

The equations for conduction and radiation can be written as a function of the insulation's outer surface temperature. The conduction for heat loss takes into account the amount of heat transfer across the block, the steel foam and the insulation

material. It also has a factor h_{a-b} to take into account a discontinuous temperature drop resulting from heat transfer between different materials.

$$\dot{Q}_{condL} = \frac{(T_{blk} - T_{out})}{\left(\frac{th_{blk}}{k_{blk}} + \frac{1}{h_{b-s}} + \frac{th_{st}}{k_{st}} + \frac{1}{h_{s-i}} + \frac{th_{is}}{k_{is}}\right)}$$

$$\dot{Q}_{radL} = \epsilon\, \sigma_b\, T_{out}^4$$

(3.16)

The equations shown above can be iteratively or analytically (quartic root solver) solved to find the outer surface temperature as well as the heat loss per area. The heat loss term can then be converted to a volumetric term using the surface area-volume ratio for a cylinder, $\frac{2}{r_{blk}}$.

3.2.3 Heat Transfer Coefficient

The heat transfer coefficient is dependent on the material properties of both the gas and the block. As with the friction term for nitrous oxide flow, there appears to be no heat transfer coefficient tabulated for convective heat transfer between nitrous oxide gas and a porous material. Therefore, one was approximated using the Nusselt number for the gas. The Nusselt number is defined as the ratio between convective and conducive heat transfer. It can be written as $\frac{h\,l}{k_{gas}}$ where l is the characteristic length of the system, set to 0.01 m for this study. The Nusselt number for fluid through a porous medium can be calculated via Eq. (3.17) [84]. This is valid for low values of Reynolds number and is valid for this study.

43

$$Re = \frac{\rho_{N_2O}\, u\, l}{\eta}$$

$$Pr = \frac{cp\,\eta}{k_{gas}}$$

(3.17)

$$Nu = 2.0 + 1.1\, Pr^{\frac{1}{3}}\, Re^{0.6}\, P^{0.6}$$

$$h = \frac{Nu\, k_{gas}}{l}$$

Although the equations do not take into account the characteristics of the block, the authors believe they provide an approximate value that of h.

3.2.4 User-Set Parameters

This section will focus on all the parameters that are system specific and set by the user. Table 3.1 lists all the parameters required for the system. The model currently simulates a copper metal foam with a high porosity P inside a steel sleeve wrapped in an ceramic-wool insulation material. Some values and constants are taken at specific temperatures instead of being calculated as a function of temperature.

Table 3.1: List of all simulation parameters

Parameters	Value	Comment
Gas Properties		
Total gas density*, ρ	3 (1-6) $\frac{kg}{m^3}$	Set close to standard temperature and pressure (STP) value
Gas velocity*, u	0.01 (0.008 - 0.013) $\frac{m}{s}$	Set after determining what best allows decomposition
Gas thermal conductivity, k	0.04 $\frac{W}{m-K}$	Set to value at 600 K
Volumetric friction term, F_b	$\sim 1 \frac{N}{m^3}$	Friction term calculated
Block Properties		
Relative block density*, $1-P$	0.12 (0.05 - 0.20) $\frac{kg}{m^3}$	Set based on metal foam used
PPI*	10 (5 - 50) $\frac{kg}{m^3}$	Set based on metal foam used
Block density*, ρ	$8940\,(1-P)\,\frac{kg}{m^3}$	Set based on metal foam used
Specific surface area*, σ	600 (100 - 2000) $\frac{m^2}{m^3}$	Set based on metal foam used
Block thermal conductivity, k_{blk}	$\frac{2}{3}\,(1-P)\,k_{metal} + k\,P$ $\frac{W}{m-K}$	Gibson and Ashby [85]. Mehrdad [2] states this could be an overestimate
Block specific heat, Cp_b	390 $\frac{J}{kg-K}$	Set based on metal foam used
Initial Conditions		
Initial block temperature	1150 K	Initial preheat temperature of block
System Setup		
Length of System	0.0635 m	Length used for simulation

* Value has been changed (within the ranges in parenthesis) to study its effects on nitrous oxide decomposition.

3.3 Numerical Techniques

Before moving forward, it is helpful to collect all the components required for the model into one place. Eq. (3.18) lists the governing equations for gas temperature, block temperature and gas density.

$$\rho_{gas}\,Cp_{gas}\,\frac{\partial T_{gas}}{\partial t} - k_{gas}\,\frac{\partial^2 T_{gas}}{\partial x^2} + \rho_{gas}\,u\,Cp_{gas}\,\frac{\partial T_{gas}}{\partial x} + u^3\,\frac{F_b + \rho_{gas}\,R\,\frac{\partial T_{gas}}{\partial x}}{R\,T_{gas} - u^2} = \dot{Q}_{dcp} + \dot{Q}_{blk}$$

$$\rho_{blk}\,Cp_{blk}\,\frac{\partial T_{blk}}{\partial t} - k_{blk}\,\frac{\partial^2 T_{gas}}{\partial x^2} = h\,\sigma\,(T_{gas} - T_{blk}) + \dot{Q}_{loss}$$

$$\frac{\partial \rho_{prod}}{\partial t} = -u\,\frac{\partial \rho_{prod}}{\partial x} - \rho_{prod}\,\frac{\partial u}{\partial x} + \alpha\,(\rho_{gas} - \rho_{prod})$$

$$(3.18)$$

Eq. (3.19) shows the decomposition rate model, Darcy's law for bulk fluid resistance, heat loss equation for the block, and the approximation for the heat transfer coefficient respectively.

$$\alpha = \frac{\alpha_0\,[M]}{1 + \frac{\alpha_0\,[M]}{\alpha_\infty}}$$

$$F_b = -\frac{\eta}{K}\,u$$

$$\epsilon\,\sigma_b\,T_{out}^4 = \frac{(T_{blk} - T_{out})}{\left(\frac{th_{blk}}{k_{blk}} + \frac{1}{h_{b-s}} + \frac{th_{st}}{k_{st}} + \frac{1}{h_{s-i}} + \frac{th_{is}}{k_{is}}\right)} \qquad (3.19)$$

$$Nu = 2.0 + 1.1\,Pr^{\frac{1}{3}}\,Re^{0.6}\,P^{0.6}$$

$$h = \frac{Nu\,k_{gas}}{l}$$

3.3.1 Simulation Setup

The simulation models a 1-D channel, composed of n nodes (set by $\frac{L}{\Delta x} + 1$) and will run for n_t time-steps (defined by $\frac{t_{max}}{\Delta t}$). The equations are solved explicitly using a central-differencing scheme in the order presented. Gas velocity and gas density are also calculated at each time-step using an upwind scheme.

3.3.2 Stability

Δx and Δt must be carefully selected to ensure stability, especially since an explicit scheme is being used to solve non-linear equations. Since the highest order present is a second-order gradient analogous to the convection-diffusion equation, the stability guidelines are based off its respective Von Neumann stability analysis ($\Delta x < \frac{2D}{Pu}$ and $\Delta t < \frac{\Delta x^2}{2D}$). In order to ensure a good spatial resolution, the Δx was lowered by a factor of $\frac{P}{2}$, redefining the stability requirement $\Delta x < \frac{D}{u}$ [86]. Furthermore, the value was sometimes user-set when the resolution generated was too coarse or too fine for a given test.

For any transport equation involving diffusion, it is conventional to identify a diffusivity constant, defined as $\frac{k}{\rho cp}$ for heat transfer. Since the second-order diffusion term is present in both the gas and block heat transfer equations, there are two thermal-diffusivity constants, D_{gas} and D_{blk}. For simplicity, D_{gas} is calculated using a constant tabulated value for nitrous oxide specific heat and not a temperature-dependent one. Since Δx and Δt are proportional and inversely proportional to the diffusivity respectively, the limiting factor must be calculated for both cases. For

Δx, $D = \min : \{D_{gas}, D_{blk}\}$ and for Δt, $D = \max : \{D_{gas}, D_{blk}\}$. The number of spatial and temporal nodes are set by the physical length of the simulated system and the total amount of time it takes to reach a steady-state solution in an explicit method.

3.3.3 Boundary Conditions

Boundary conditions for temperature, total gas density, product density, and velocity are required to close this system of differentials. Since gas velocity and density are solved using an upwind scheme, only one constant-value boundary condition is required, identified by the "in" subscript. The boundary condition for product density is set to zero since it is assumed that incoming nitrous oxide gas has not undergone any decomposition.

$$
\begin{aligned}
u(x,t)\Big|_{x=0} &= u_{in} \\
rho(x,t)\Big|_{x=0} &= \rho_{in} \\
rho_{prod}(x,t)\Big|_{x=0} &= 0
\end{aligned}
\tag{3.20}
$$

In order to accurately represent system conditions, non-homogenous mixed boundary conditions were implemented to balance all heat transfer paths at each of the end nodes for gas and block temperature.

Gas Boundary Condition

The boundary conditions for gas temperature will balance gas conduction to the left and to the right across the node, advection across the node, and convection into the node. The contribution from the change in velocity in the advective heat flux is omitted here as it is too small relative to the other terms. The left and right side boundary conditions are listed below in Eqs. (3.21) and (3.22). Conduction across the left boundary occurs with the reservoir gas at 300 K and set to zero across the right side boundary. The boundary conditions are complete when solving for T_{gasL} and T_{gasR}.

$$
\begin{aligned}
h\left(T_{blk}(1,t) - T_{gasL}\right) - \rho_{gas}(1,t)\, u(1,t)\, Cp_{gas}(1,t)\left(T_{gasL} - 300\right) \\
- \frac{k_{gas}}{dx}\left(T_{gasL} - 300\right) + \frac{k_{gas}}{dx}\left(T_{gas}(2,t) - T_{gasL}\right) = 0
\end{aligned}
\tag{3.21}
$$

$$
\begin{aligned}
h\left(T_{blk}(n,t) - T_{gasR}\right) - \rho_{gas}(n,t)\, u(n,t)\, Cp_{gas}(n,t)\left(T_{gasR} - T_{gas}(n-1,t)\right) \\
- \frac{k_{gas}}{dx}\left(T_{gasR} - T_{gas}(n-1,t)\right) = 0
\end{aligned}
\tag{3.22}
$$

Block Boundary Condition

The block boundary conditions are easier to generate since only conduction and convection need to be modeled. The boundary conditions assume that conduction cannot occur left of first node and right of node n.

$$h * (T_{gas}(1,t) - T_{blkL}) + \frac{k_{blk}}{dx} (T_{blk}(2,t) - T_{blkL}) = 0 \qquad (3.23)$$

$$h * (T_{gas}(n,t) - T_{blkR}) + \frac{k_{blk}}{dx} (T_{blk}(n-1,t) - T_{blkR}) = 0 \qquad (3.24)$$

3.3.4   Initial Conditions

In order to begin the simulation, a set of initial conditions must be specified. Initial conditions were provided for gas temperature, block temperature, total gas density and product density. Initial gas temperature across the 1-D channel is set to the reservoir tank temperature ($\sim$300 K) while the block is assumed to have been preheated to a set temperature (1175 K). The total gas density is set to an arbitrary value ($3 \frac{kg}{m^3}$) and the product density is set zero across the channel as decomposition has yet to occur. The effects of varying some initial conditions on decomposition are examined in the Results section (3.5).

3.3.5   Variable Time Steps

As mentioned before, the decomposition source term follows an exponential curve, resulting in a large amount of energy released in a short amount of distance and time. The gas temperature and density will therefore contain exponential components in their transient solutions which can cause numerical oscillations if not

50

properly addressed. Although stability guidelines were implemented to prevent this, it was only valid for a generic convective-diffusion equation without any exponential heat sources. In theory, decreasing the system resolution parameters Δx and Δt should solve this issue, but limitations in computational resources motivated the authors to resolve it using another approach.

Since this model prioritizes the steady-state solution over the transient counterparts, it is possible to bypass the instabilities by modifying the rate at which each component updates in time. The method requires two new stability parameters, Δt_{gas} for the gas equations and Δt_{blk} for the block equations, in addition to Δt to be defined. These parameters are then each set to a factor lower than the overall Δt, which is still applied to the density equations. The authors were able to identify these factors by iterating through numerous simulations, focusing on stability and time required to reach a steady-state solution. As a result, the gas component ended up having the lowest Δt_{gas} in the simulation hierarchy, meaning it will update the slowest. The block component will update at a faster Δt_{blk} but still slower than the density component, which updates at the fastest Δt solved previously. For example, if Δt_{gas} was $0.3 \, \Delta t$ and Δt_{blk} was $0.5 \, \Delta t$, then for every one time step of density, the gas updates 30% of the overall Δt and the block would update at 50%. This results in the solutions being out of phase, with a non-physical transient solution, but with the benefit of faster convergence to steady-state.

Furthermore, the gas equations were solved twice at each overall Δt before moving onto the block equations. The solution after one calculation was used as an initial condition for the gas equations, solving them again using the solutions for

block temperature and gas density from the previous time-step. This allowed the simulation to progress as quickly as possible towards convergence without generating any oscillations that caused system instability. Current simulation factors are set to run the block component at 75% and the gas component at 25% of the density Δt.

3.4 Validation

Although a thorough validation of nitrous oxide decomposition will be done with the experimental setup described above, preliminary validation is still beneficial to ensure some of the heat transfer components of the model are implemented correctly. Tsolas [1], and later on by Mehrdad [2], conducted experiments testing heat transfer between air and nickel foam. Their experimental setup involved using a 20 mm x 20 mm square cross-sectional, 10 PPI nickel foam heated using a rope heater and measured gas and foam temperature along the channel. Gas is flowed through the foam using mated compression fitting on either end of the foam. The foam has a sprayed skin to keep the gas contained and is placed in a stainless-steel bracket, exposing three of the foam sides. The rope heater is wrapped over the sprayed skin and the steel bracket and inputs a constant heat flux based on voltage.

For this validation, the model will simulate air flowing through the nickel foam at 0.8 $\frac{m}{sec}$ with the heater running at 60 volts. It should be noted that the conversion from the heat flux (calculated using the resistance and dimensions of the heater) to a volumetric heat source is not as trivial since the heater is in contact with the sprayed skin and the stainless-steel bracket. A factor of ~ 0.78 had to be implemented to

match the heat flux going to the center of the nickel foam (which is what the model is simulating). The heat transfer coeffecient h was set to 22 $\frac{W}{m^2-K}$ (from experimental measurements in [1]) and is on the same order as h predicted using the Eq. 3.17. The foam thermal conductivity is set to 1.8 $\frac{W}{m-K}$ [2] and is in agreement with the value predicted by the foam conductivity equation listed in Table 3.1. The comparison between experimental and simulated gas and block temperatures is shown in Fig. 3.3. Apart from the gas temperatures near the inlet, the simulated gas temperatures are in strong agreement with the measured values. The block temperatures are in agreement in the middle of the chamber but diverge a little at both ends of the system. One explanation that can account for the temperature difference at the boundaries could be due to the abrupt change in area as the gas enters and exits the foam (due to the compression fitting being smaller than the cross-sectional area of the foam). This results in stagnant gas at both ends which could affect heat transfer. Furthermore, any error in the heat transfer coefficient could result in a temperature profile with a different slope, as seen in the block temperature plot. Nonetheless, the model supports the experimental measurements for gas temperature to under 3% error and the experimental measurements for block temperatures to under 4% error. Further validation will still need to be performed for nitrous oxide decomposition.

3.5   Results

This section explores the effects of varying flow and block parameters on achieving self-sustained decomposition. The first step is to establish a baseline case
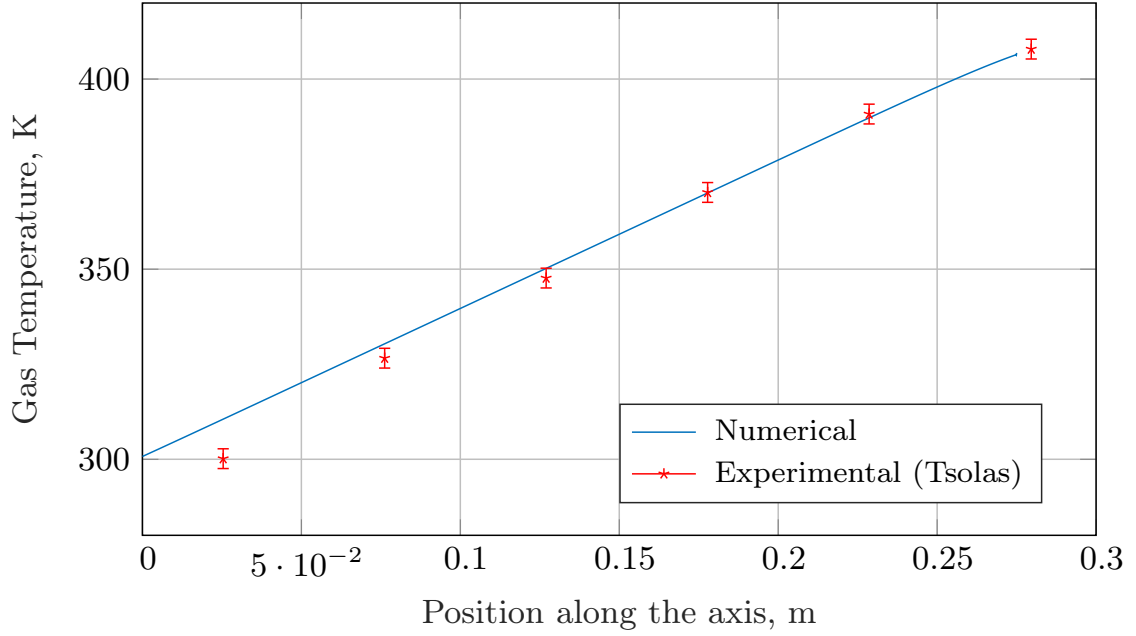
(a) Gas temperature (validation)
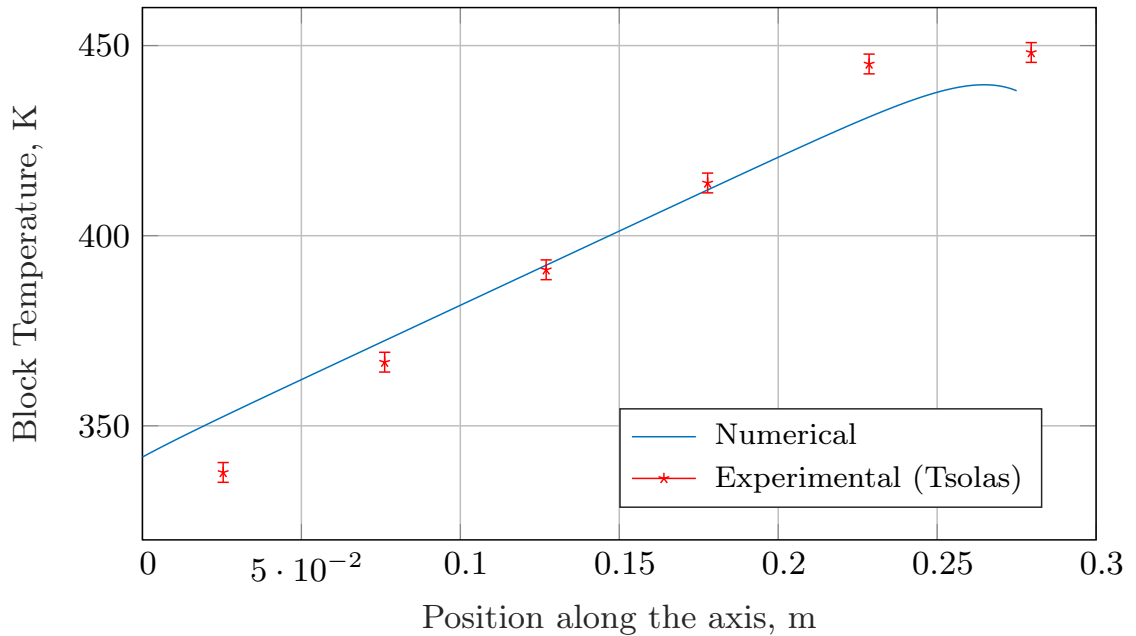
(b) Block temperature (validation)

Figure 3.3: Model validation using an experimental case with air flow through a 10 PPI nickel foam. The data corresponds to gas velocity of 0.8 $\frac{m}{sec}$ and constant heat flux from a rope heater [1, 2].

where self-sustained decomposition does occur. The parameters for this case are shown in Table 3.1. Furthermore, the iteration bounds for the parameters that were

varied are shown in parentheses next to them in subsequent tests. Convergence to steady-state was considered achieved when the relative change in block temperature at a predetermined location fell below a prescribed threshold.

In order to evaluate the effect of changing of some parameters more relevant to this study, steady-state solutions for gas temperature, block temperature, gas density and gas velocity at the centerline are plotted with respect to chamber length. The gas density plots all show two lines for each simulation result, one corresponding to the total density (dashed) and the other to the product density (marker-points). The system is assumed to have achieved full decomposition when the two lines meet. The number of points in each plot do not represent the spatial resolution used in the simulation as they were reduced to increase the clarity of the plots.

It should be stated that the parametric studies conducted below are not necessarily independent of the flow regime. As shown in previous sections, increasing fluid velocity or density can introduce a non-linear component in the friction term, kicking the system out of the Darcy flow regime. Similarly, increasing sigma can also increase the pressure drop across the foam as it would increase flow resistance by lowering permeability [1]. Furthermore, given a constant porosity, the only ways to increase a foam's effective surface area is by either increasing its surface roughness or increasing its PPI. Researchers have shown that either case results in an increased pressure drop (reduction in permeability) at any given velocity [81, 87]. This increase in pressure drop is propagated quadratically at larger velocities due to no longer being in linear Darcy regime. However, since the Reynolds numbers in this study are sufficiently small, the effects of changing sigma on flow resistance are

assumed to be negligible in this study.

3.5.1   Baseline

Fig. 3.4(a) plots the gas temperature across the channel based on the parameters described in Table 3.1. Once the gas temperature is at least ~ 1000 K, decomposition occurs rapidly, described by the large increase in temperature with a peak temperature around 1600 K. This is also in agreement with the exponential increase in product density shown in Fig. 3.4(c). Although the increase looks discontinuous, this is just an artifact from not plotting all the points. It is important to note that in a transient solution, decomposition can occur at any point in the channel. However, once it does occur, the heat balance forces decomposition upstream. The location of steady-state decomposition equilibrium is determined by thermal and fluid properties of system. Previous simulations involving hydrogen peroxide have shown decomposition occurring within a narrow zone near the entrance of the decomposition region [88–90]. Once all of the nitrous oxide has decomposed, shown by the total density and product density converging in Figure 3.4(c), there is no longer a exponential source term for the gas. In fact, now that the gas temperature is higher than the block temperature, the direction of heat transfer between the block and the gas has reversed. Due to this, the gas temperature steadily drops and equilibrates to the block temperature near the end of the channel.

Fig. 3.4(b) plots the block temperature across the channel. Due to the high conductivity of copper, the temperature is mostly uniform with the difference be-

tween the maximum and minimum temperature being only a few Kelvin. One aspect to highlight is the block temperature is close to copper's melting point (~ 1350 K) and therefore this solution might not be feasible. Subsequent tests based on parameter variation will primarily aim to understand their effects and utilize them to keep the exit temperature much lower than the melting point.

In Fig. 3.4(c), total gas density and product density converge as full decomposition is achieved and continue to be equal across the channel. Gas velocity is correctly shown to be negatively proportional to gas density in Fig. 3.4(d).

3.5.2 Parameter Variation

3.5.2.1 Sigma (σ)

Fig. 3.5 plots the results from varying the effective surface area of the material. The solution at $\sigma = 100$ (not shown) actually failed to reach decomposition as the whole system equilibrated to slightly under 300 K. Overall trends have shown a negative correlation between σ and gas/block temperature. As σ is increased, gas and block temperature decrease since a higher sigma yields to a stronger heat transfer path between the gas and the block. Figs. 3.5(c) and 3.5(d) show the negative correlation between total density and gas velocity, resulting from mass flux being constant across a channel. Furthermore, some of the solutions, specifically lower sigmas, result in block temperatures that are close to copper's melting point. Since a lower σ results in a higher exit gas temperature, maximum performance can be achieved by lowering sigma as low as possible while maintaining block temperature
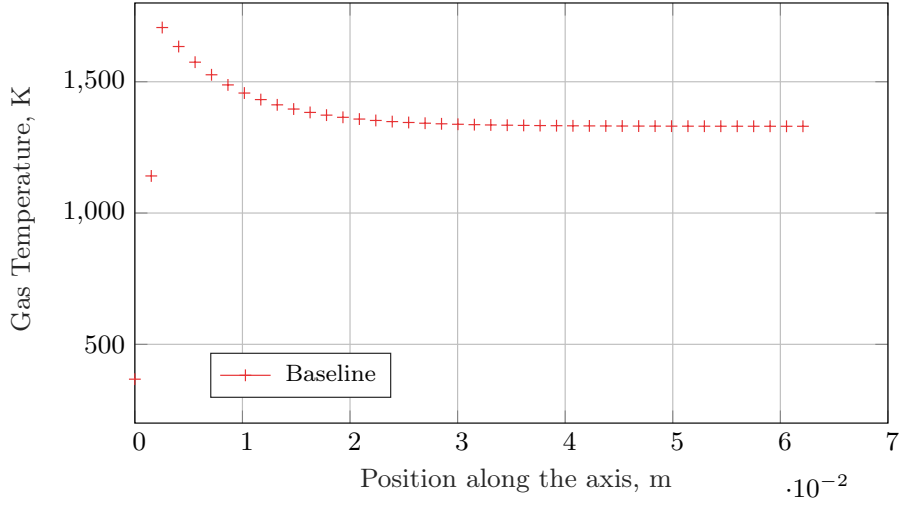
(a) Gas temperature
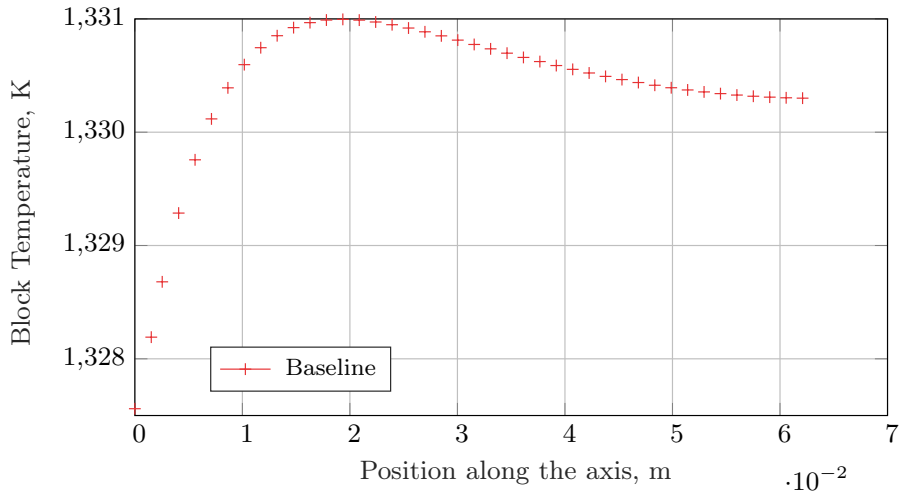
(b) Block temperature
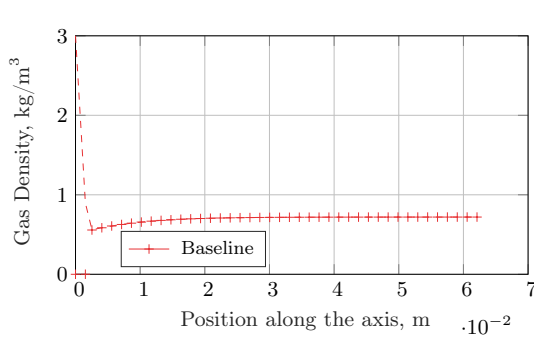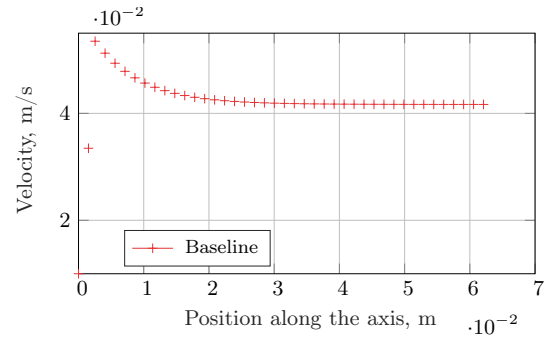
(c) Gas density

(d) Gas velocity

Figure 3.4: Plots of system parameters versus axial location for the reference solution.

below its melting point.
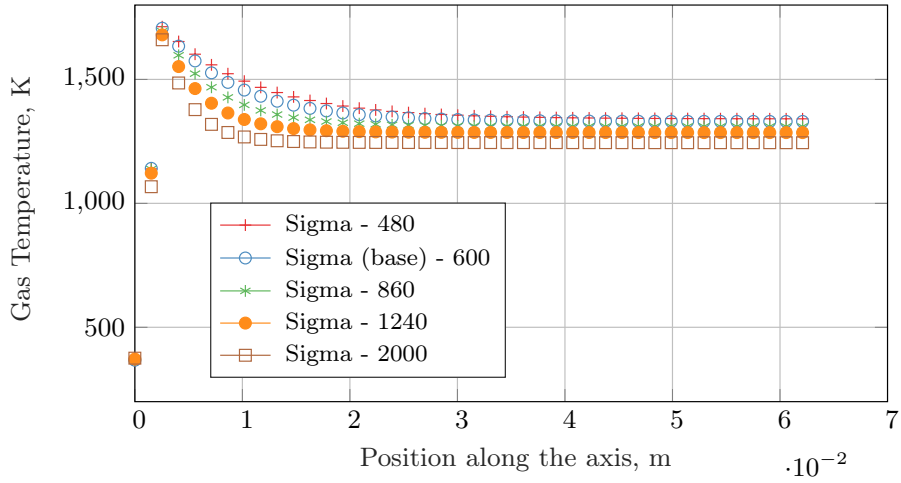
(a) Gas temperature
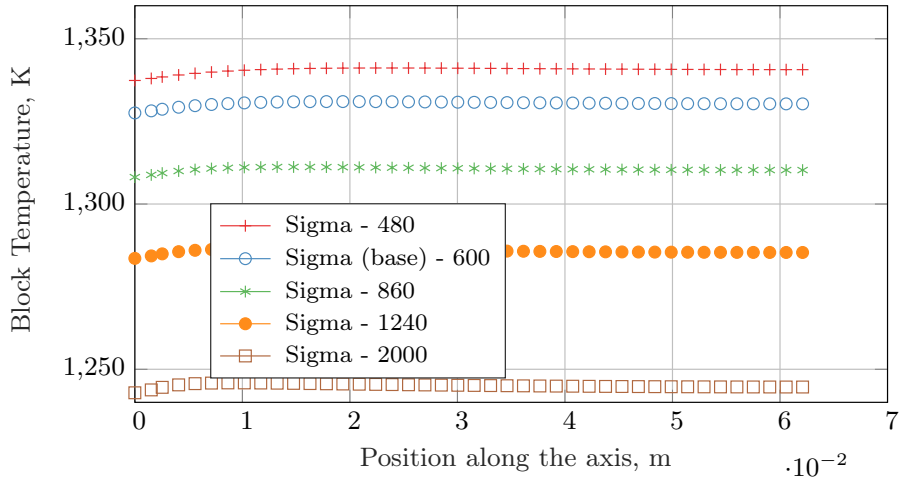
(b) Block temperature
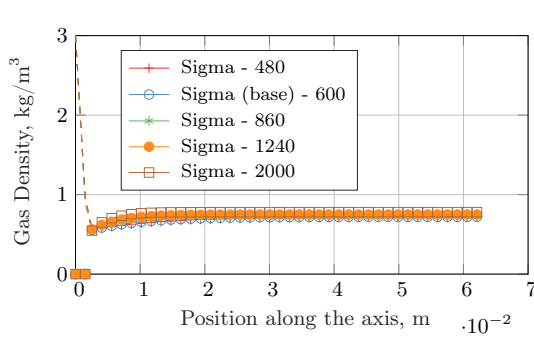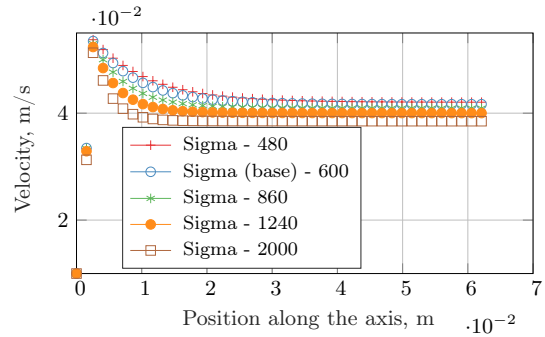
(c) Gas density

(d) Gas velocity

Figure 3.5: Plots of system parameters versus axial location for varying values of σ $\left(\frac{m^2}{m^3}\right)$.

3.5.2.2 Gas density (ρ)

Inlet nitrous oxide concentration is shown to have a positive correlation with both gas and block temperature, as expected. As the gas density is increased past the baseline case, steady-state solutions with temperatures surpassing copper's melting do occur. Furthermore, there is a minimum and maximum gas density at which decomposition can be sustained, specific to each system. This is in agreement with previous simulations that studied the effects of inlet hydrogen peroxide concentration on gas temperature and efficiency of decomposition [89].

3.5.2.3 Gas velocity (u)

Varying gas velocity produces similar effects as gas density, where an increase results in higher exit temperature. This is due to the system resupplying nitrous oxide quicker, allowing the system to be self-sustained at higher temperatures. There also exists a minimum and maximum gas velocity at which decomposition can be ignited, given a set preheating block temperature. This has been shown in previous models where an increase in velocity stretched the decomposition distance [91]. Therefore, one limiting factor on velocity would be when the decomposition distance is close to or greater than the chamber length.

3.5.2.4 Block Parameters

Block PPI seems to have a very small effect on decomposition solutions, at least in the range studied here. Within the simulation, PPI is only of importance

when calculating the friction force discussed in the previous sections. Although varying PPI within this range does change friction force, it does not account for the low gas velocity and therefore has very little effect on the solutions. Furthermore, it was found that the friction force needs to be on the order of $\sim 1 \times 10^6$ to impede decomposition.

Another parameter studied is the relative block density, which affects the friction term as well as the block thermal conductivity. It was found that increasing the block density does not affect the gas temperature but does make the block temperature profile more uniform, similar to increasing the thermal diffusivity coefficient in the heat equation.

From preliminary testing, it was understood that the temperature at which the block was preheated will have a strong impact on whether any decomposition occurs. Once the block is preheated past a minimum threshold, decomposition will initiate within the system. This minimum temperature is system specific, based on the thermal, fluid and block parameters. For the parameters listed in Table 3.1, this temperature is approximately 1150 K. Once decomposition does occur, the final steady-state solution is no longer affected by the initial block temperature, which is expected.

Before moving forward, it is beneficial to characterize the transient response, especially since the model does not present a correct transition from transient to steady-state. The simulation assumes the block is already preheated to an initial temperature before gas is flowed through the system and therefore the question that arises is how hot does the block need to be to ensure the transient region is negligible.

61

One way to address this is to calculate the Damköhler number, defined as the ratio of the fluid and chemical time scales, $Dn = \frac{L}{u}\alpha$. A large value (typically $Dn > 1$ to $Dn > 10$) represents a high conversion (decomposition) within the system. Ref [8] showed that the characteristic decomposition time reaches unity when the gas is approximately 1200 K. For the baseline case, Dn is of order 1 when the gas is around 1150 K and greater than 10 when the gas is heated past 1250 K. It should be noted that at greater velocities, Dn decreases to below 1 and this explains why there is an upper limit on gas velocities as mentioned above. At large velocities, the chamber length is too short for any decomposition to occur within the chamber (at a set reaction rate) [89].

Since the energy release from decomposition is of exponential nature, the limiting factor that determines the transition time to a steady-state is primarily dependent on how long it takes to heat the gas to the temperatures mentioned above. Cold nitrous oxide gas is heated via the volumetric convective term, $h\,\sigma\,(T_{blk} - T_{gas})$. Given the fluid and thermal parameters for the baseline case, the time required to heat the gas is on the order of 100's of milliseconds. This can be reduced by increasing the heat transfer parameters used for convection (10's of milliseconds if the quantity $h\,\sigma$ is increase by a factor of 5). It should be noted that these calculations are an overestimate because as the gas heats up to thermal decomposition temperatures, the input source term from decomposition becomes non-negligible, reducing the heating time even further.

As shown above, the limiting factor for any solution, given a set of parameters, stems from the melting point of the block material used, as exceeding it would be

considered a system failure. In any steady-state heat transfer solution, two materials will equilibrate to the same temperature, barring any external source (or sink). Therefore, nodes farthest from decomposition (at the end of the channel) tend to have gas and block temperatures approximately equal since the decomposition term has been driven to zero. Although there is a heat loss term that is still active, it is relatively small and does not have a large impact due to the insulation. The maximum exit gas temperature, with the block temperature still under its melting temperature, found was around 1345 K which was also the block temperature at that location. Therefore, it can be assumed that by changing a few parameters, it is possible to achieve a gas and block exit temperature of 1350 K, which is copper's melting temperature. One can extend this constraint by simply selecting a metal with a higher melting point.

Fig. 3.6 shows a comparison between copper and metals that have higher melting points (at inlet gas density of 6 $\frac{kg}{m^3}$). It should be noted that the steady-state block temperature for copper surpasses its melting point. In most cases, metals with a higher melting point tend to have lower thermal conductivity when compared to copper. This is best seen with the stainless-steel and titanium foams, where the block temperature is not uniform when compared to copper. The stainless-steel foam, which has a thermal conductivity an order of magnitude smaller than copper, experiences a temperature range of $\sim$100 K.

The fluid conditions simulated so far have been for the experimental setup described earlier and might not be representative of any actual thruster conditions. Therefore, the flow rates set in the model are much lower than the minimum
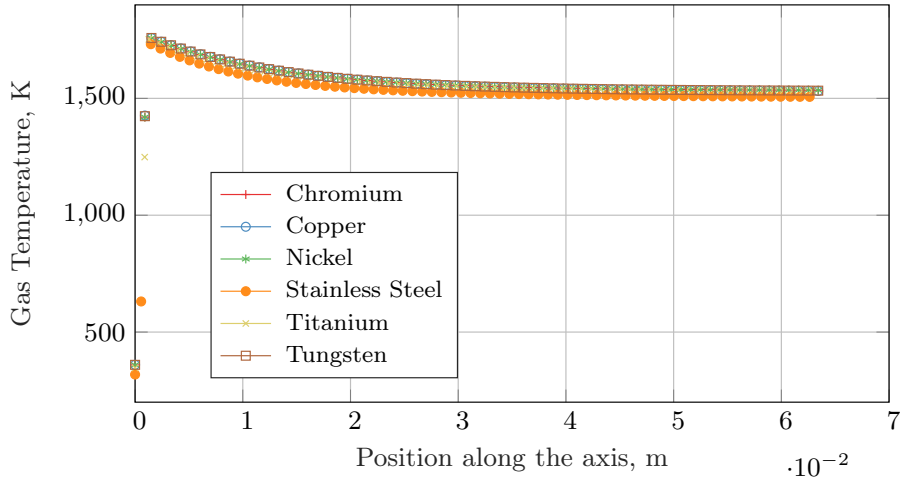
(a) Gas temperature
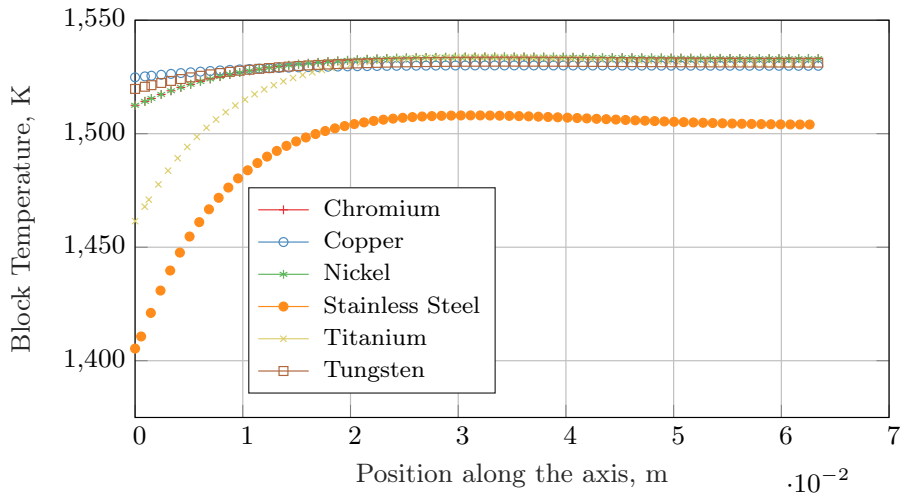
(b) Block temperature
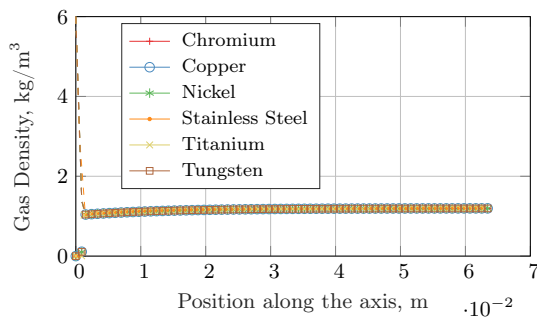
(c) Gas density
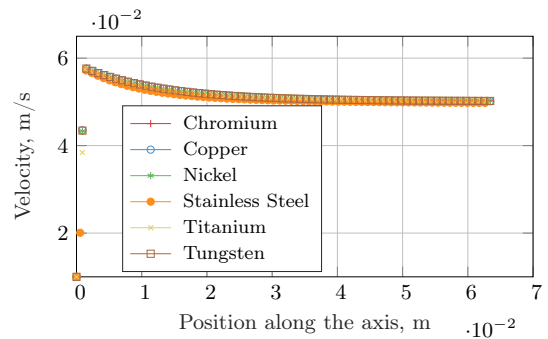
(d) Gas velocity

Figure 3.6: Solutions for nitrous oxide decomposition using various high temperature metals.

flow rates of typical 1N monopropellant thrusters. One example of a nitrous oxide thruster using a self-pressuring nitrous oxide feed system in orbit is the UoSAT-12 satellite [54]. Their system was able to demonstrate a constant mass flow rate of 0.13 $\frac{g}{s}$ without requiring any additional heating for the propellant tank. Simulating this mass flow rate at a reduced inlet temperature resulted in successful decomposition of nitrous oxide using a stainless-steel foam. To ensure that steady-state decomposition was achieved, the decomposition chamber was scaled up accordingly (to keep Dn above 1). The radius was increased by a factor of 2 (38.1 mm or 1.5" diameter) and the length was increased by a factor for 1.5 (95.25 mm or 3.75") with the initial temperature of the foam set to 1200 K.

The solutions from copper and other high temperature metal foams show it is feasible to reach self-sustained decomposition given a specific experimental design (chamber length, gas velocity, gas density, foam and insulation properties). Furthermore, the model helps identify the preheat temperatures required by the foam (and thereby how much energy required from the inductive heating system) to initiate decomposition. As mentioned before, one mode of failure can occur if the temperatures within the decomposition chamber are higher than the foam's melting point. The model will help ensure that none of the temperatures experienced within any experimental run will cause such a failure. Lastly, once experimentally verified with copper foam, the model can extend the theory to other homogenous metal foams that are commercially available.

Chapter 4: Nitrous Oxide Decomposition Using Inductively Heated Heat-Exchangers

The previous chapter focused on creating a one-dimensional numerical model to help model the experimental setup and understand the effects of various fluid and thermal parameters on decomposition. Using these results as guidelines, this chapter details the experimental work testing three different heat exchangers, all preheated using an inductive circuit. The first is the copper metal foam simulated in the numerical model. The other two are copper and stainless-steel discs. Each heat exchanger's ability to successfully reach steady-state decomposition of nitrous oxide was evaluated and compared against carbon dioxide as a control when required.

4.1 Experimental Setup

Fig. 4.1 provides a detailed schematic of the laboratory setup used in this work. It utilizes a vacuum bell jar system to house the decomposition chamber (steel housing with heat exchanger) and the inductive heating circuit. The following sections will describe the vacuum system, flow system, induction circuit, and decomposition chamber in more detail.
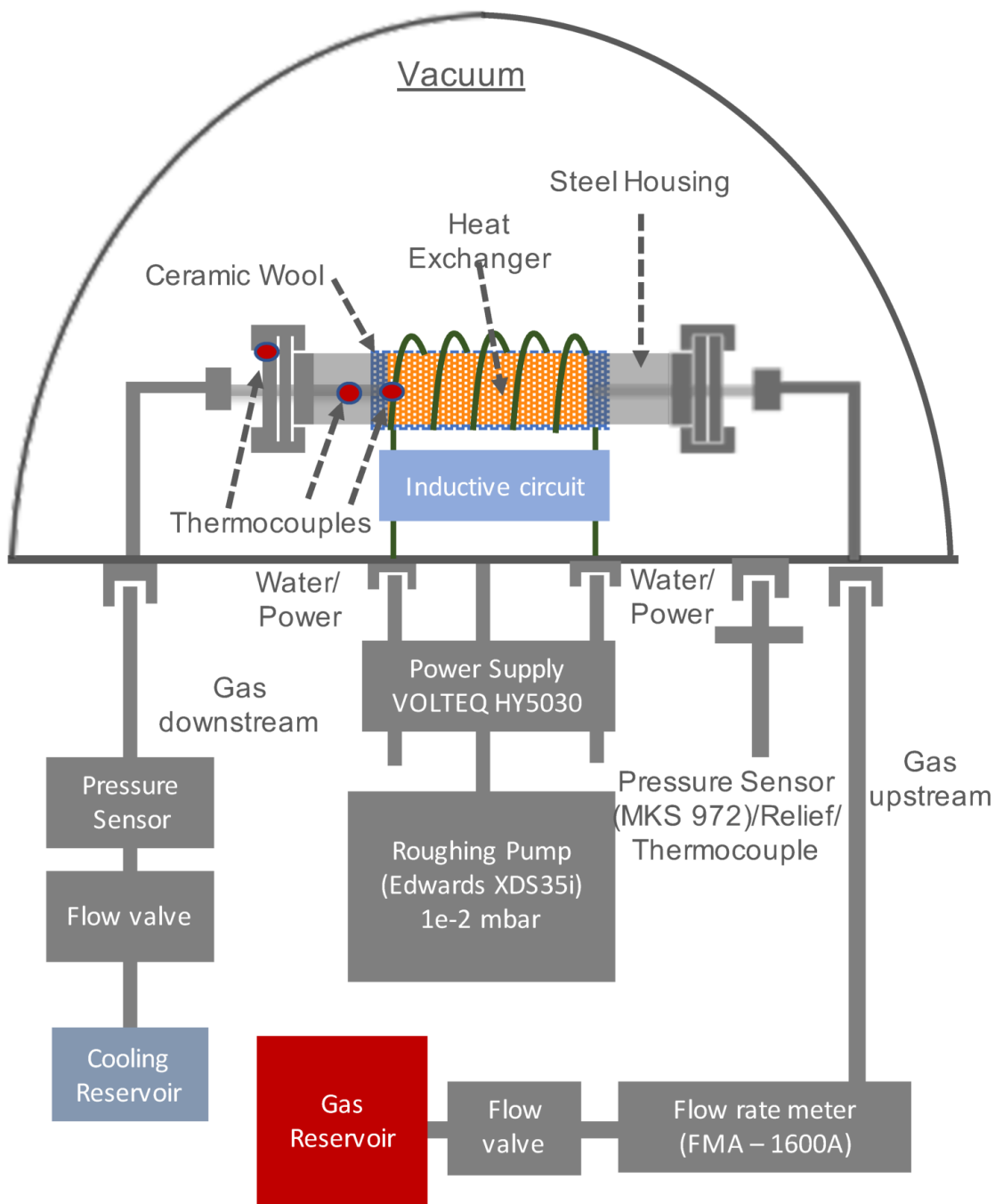
Figure 4.1: Overview of the experimental setup

4.1.1 Bell Jar Vacuum System

The bell jar vacuum system consists of a 18" x 18" (457.2 mm x 457.2 mm) quartz bell jar sitting on a 20 inch (508 mm) diameter, 1 inch (25.4 mm) thick baseplate and sealed using an L-gasket (Fig. 4.2(a)). The baseplate has six ports; one ISO-63 port for a roughing pump and five Klein Flange (KF-25) ports (all sealed using O-rings) for various instruments and feedthroughs (Fig. 4.2(b)).
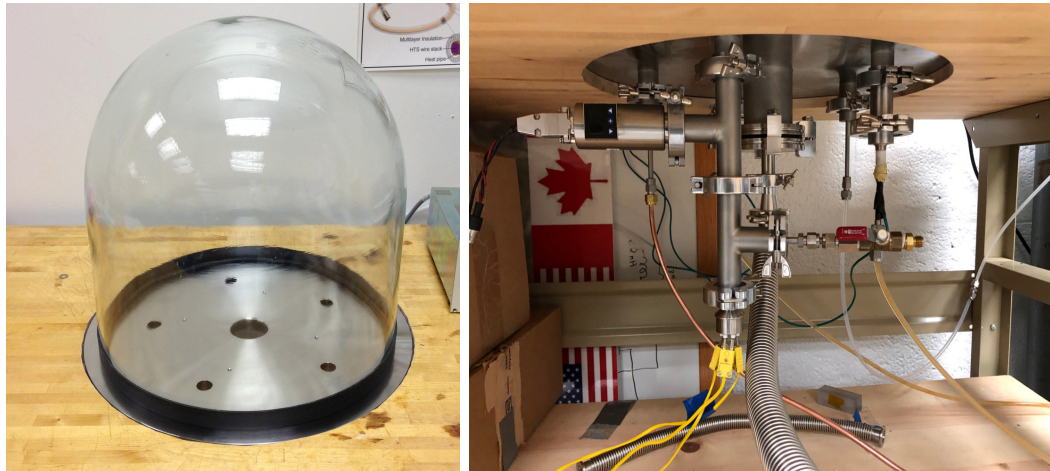
<table>
<tr><td>(a) Bell Jar/Base Plate</td><td>(b) Baseplate with Ports</td></tr>
</table>

Figure 4.2: Pictures of the bell jar, base plate and ports

Table 4.1 describes the instruments attached to each of the ports in greater detail. Two ports are used for upstream and downstream gas feedthroughs. A more detailed description of the flow system including instruments and values will be presented in a later paragraph. In order to provide both DC power and water cooling for the inductive heating circuit, two RF feedthroughs were installed. The last KF port was used for a pressure sensor, a relief valve, and a thermocouple feedthrough. The roughing pump used was able to reduce the pressure of the chamber (with all

components) to roughly 0.02 - 0.05 mbar (2 - 5 Pa), close to its ultimate pressure of 0.01 mbar (1 Pa).

The system is capable of running both nitrous oxide and carbon dioxide. Two high pressure cylinders, one for each gas, are connected to the system via a swagelok tee. A volumetric flow meter is used in conjunction with a valve to set the mass flow rate through the decomposition region. A pressure sensor and a valve are used downstream to control the pressure within the decomposition chamber. Fig. 4.3 outlines the flow path for nitrous oxide and carbon dioxide.
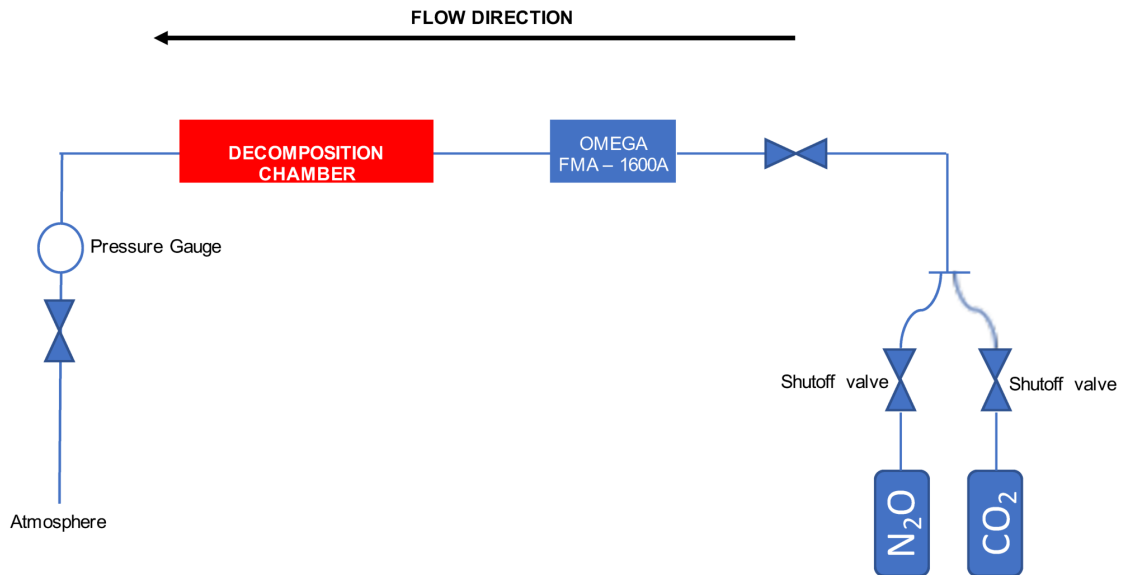
Figure 4.3: Flow Schematic

4.1.2 Inductive Heating

The primary reason monopropellant thrusters employ catalysts as a means for decomposition is due to the high activation barrier found for thermal decomposition. For nitrous oxide, the activation barrier is overcome only when it is heated beyond

Table 4.1: Description of the ports are used on the baseplate

Port	Instrument	Comment
ISO-63	XDS 35i Scroll Pump	Ultimate Pressure: 0.01 mbar (10000 Pa)
KF-25 (1)	Upstream gas feedthrough	Feeds from a reservoir tank
KF-25 (2)	Downstream gas feedthrough	Exit line from decomposition chamber
KF-25 (3)	Upstream water/power (RF power feedthrough)	Power/water cooling for inductive heating circuit
KF-25 (4)	Downstream water/power (RF power feedthrough)	Power/water cooling for inductive heating circuit
KF-25 (5) - Relief value	(1) 3 pair type K thermocouple feedthrough	Used for measuring temperature inside decomposition chamber
	(2) MKS Model 972 pressure sensor	Range: atmosphere to 10^-8 mbar (8×10^{-7} Pa)

1200 K (when the reaction rate becomes order unity). Unfortunately, current heaters such as resistive wire used in monopropellant thrusters preheat catalysts to only a fraction of these temperatures [3, 11, 92–94]. Inductive heating, on the other hand, offers the ability to sucessfully heat metals to these high temperatures.

There are three main components to any form of inductive heating: an induction circuit (AC signal), induction coils (solenoid) and a conductive workpiece (metal that is to be heated, typically a tube or a solid rod). The circuit sends an AC signal into the induction coil, which produces a time varying magnetic field within the coil. When the workpiece is inserted inside the coil, eddy currents are generated on the surface due to the changing magnetic field according to Faraday's law of induction. These eddy currents, although at the same frequency as the AC signal and magnetic field, are in the opposite direction of the coil current. As long as the AC signal is maintained, the eddy currents will continue to form (and flip directions) and heat the workpiece from joule heating ($P = I^2 R$). Here, I and R are the current induced and the resistance of the workpiece respectively. The strength of eddy currents is proportional to the rate of change in magnetic flux experienced in the workpiece [95, 96].

Various parameters can have defining effects on how strongly the workpiece is heated. The resistivity of the workpiece, ρ, directly correlates to the power dissipated via the eddy currents ($R = \rho \frac{l}{A}$). The relative permeability of the workpiece, μ, influences how many of the magnetic field lines penetrate the surface, resulting in more eddy current loops. The frequency of the induced current determines how deep the eddy currents penetrate the surface of the workpiece. The formula for the

skin depth, d in centimeters, is $5000\sqrt{\frac{\rho}{\mu f}}$ where f is the frequency of the signal. Frequencies on the order of 100's of kHz are typically used to heat small and thin objects whereas frequencies less than 100 kHz are used for thicker materials. Heating is more efficient at higher frequencies up to a critical frequency where the ratio between the diameter and depth is about four. Furthermore, using workpieces that are magnetic experience an added effect known as hysteresis. Hysteresis occurs as a result of the magnetic dipoles oscillating and continues to help heat the workpiece until a certain threshold. This limit, known as the Curie temperature, represents the transition at which the material becomes nonmagnetic (relative permeability drops to unity) [95]. The main advantage of using an inductive heating system is the ability to heat a workpiece without any physical contact, limiting any thermal degradation that might occur. The general configuration of the decomposition chamber is designed around a steel tubular housing in which the heat exchanger is placed. The eddy currents are induced on the surface of the housing, which heats up and in turn heats the heat exchanger provided there is strong thermal contact.

Two COTS high-frequency tank circuits were tested for high-temperature heating. Both circuits function using a VOLTEQ DC power supply (50A/30V) and produce an AC signal through an induction coil using transistors as part of an H-bridge circuit (half or full). Fig. 4.4 gives a top-level schematic of an H-bridge circuit, where each of the switches represents a transistor. The coil consists of seven turns of copper pipe, with an inner diameter of 2 inches (50.8 mm) and a length of 2.5 inches (62.5 mm). In general, the coupling between the coil and workpiece

is important and it is good practice to have the workpiece outer diameter as close to the inner diameter of the coil as possible. Therefore, the workpiece is a 1 inch (25.4 mm) diameter, 0.12 inch (3.05 mm) thick low-carbon steel. This allows for a half inch thick insulation to be wrapped around the housing to mitigate heat loss. Low-carbon steel was chosen because it has a higher resistivity and permeability than copper or stainless steel.
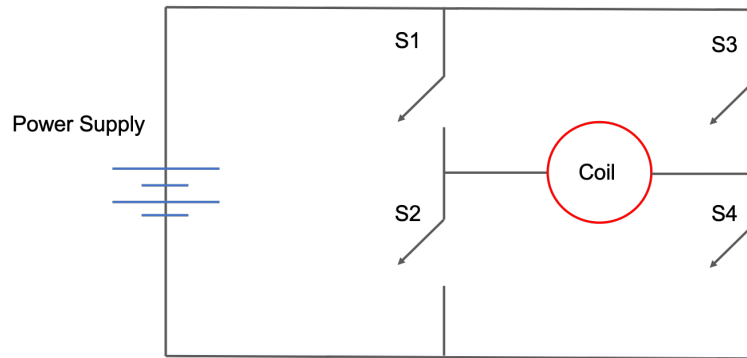
Figure 4.4: Schematic of a full H-bridge circuit where the switches (S) control the direction of the DC signal.

The first circuit (1000W ZVS low voltage induction circuit) tested was a 1000 W max power that operated at a resonant frequency of 97 kHz. Initial tests proved this frequency was too high for effective heating of the workpiece and needed to be reduced. Since the frequency of an LC tank circuit is proportional to $\frac{1}{\sqrt{LC}}$, it was dropped to 60 kHz by adding capacitance to the circuit. At the lower frequency, the low carbon steel was heated close to 1000 K which, although a promising result, was still not close enough to 1200 K required ensure thermal decomposition.

The second circuit (1800W ZVS induction circuit) tested was an extension of the first circuit, capable of handling up to 1800 W max power with a resonant frequency around 85 kHz for the low carbon steel. Because it runs at higher power,

(a) Low power circuit
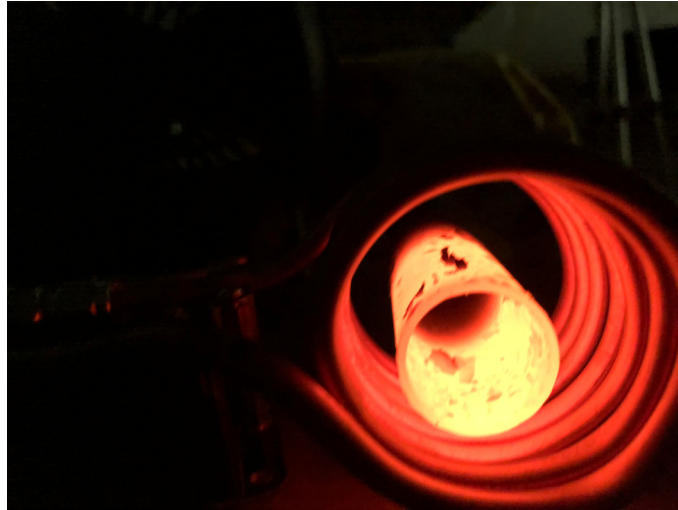
(b) Low carbon steel heated up to 1000 K (lower power)
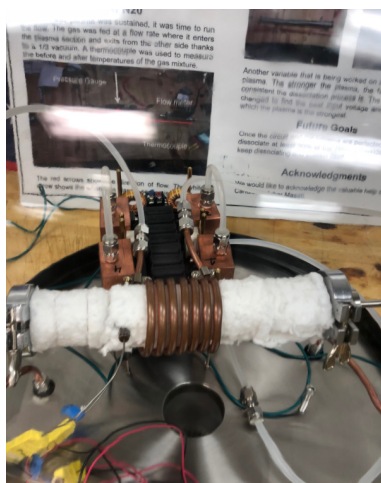
(c) High power circuit with ceramic wool insulation and water cooling
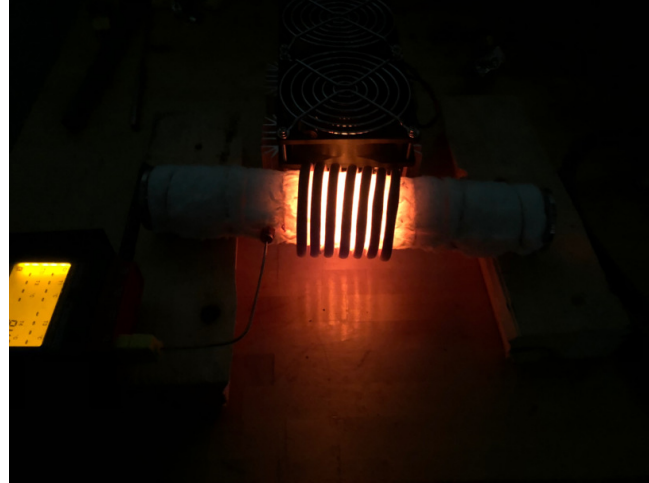
(d) Low carbon steel heated up to 1300 K (high power)

Figure 4.5: Testing of both inductive heating circuits

a water cooling system had to be implemented that first cools the induction coil and then the four transistors. This circuit was able to successfully heat the inside wall of the steel housing past 1300 K with insulation on the outside. It should be stated that during the heating, there was a reduction in current (from the power supply) at a constant voltage once the low-carbon steel surpassed its Curie temperature. This did lower the heating rate but was still successful in reaching the

desired temperatures. Therefore, the second circuit was implemented to preheat the decomposition chamber for all subsequent tests. Fig. 4.5 shows both circuits and a snapshot of when the low carbon steel tube was being heated. Initially, the circuit was placed outside of the bell jar with copper pipe feeding water and power to the coil inside the vacuum chamber. This however, introduced capacitive losses that significantly affected the heating power for the workpiece. Therefore, the circuit was moved inside the bell jar, minimizing the copper pipe between the circuit and the coil.

4.1.3 Decomposition Chamber

(a) Decomposition chamber (axial)

(b) Decomposition chamber (cross-section)
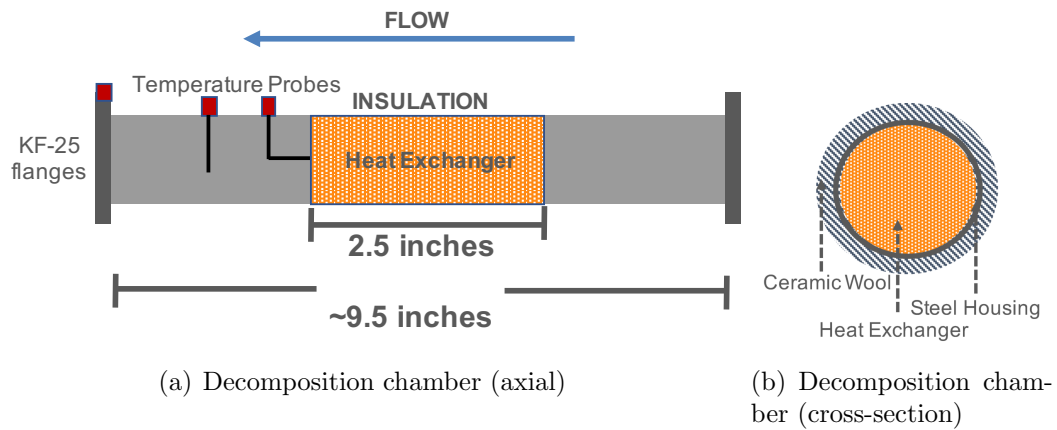
Figure 4.6: Schematic of the decomposition chamber

A schematic of the decomposition chamber is shown in Fig. 4.6. The low-carbon steel tube, with two KF-25 flanges welded on, is 9.5 inches (241.3 mm) long and has a cross-sectional area the same as from circuit testing. All of the heat exchangers tested are 2.5 inches (63.5 mm) long, limited by the axial length of the coil used for inductive heating. The outer diameter of the heat exchanger is

only slightly smaller than the inner diameter of the housing to ensure it fits inside the housing and maintains a strong thermal connection. The housing is sealed from the evacuated chamber via KF-25 feedthroughs on either end and is wrapped with insulation to mitigate radial heat loss. The insulation used is half-inch thick ceramic wool with a melting point of of over 1500 K and a thermal conductivity of $0.01 \frac{W}{m-K}$. The housing material and flanges do change when testing the third heat exchanger and will be explained in following sections. Two type K thermocouples are used to measure both the downstream gas temperature and the heat exchanger's temperature. These were attached using a compression fitting that was directly welded onto the housing. A third thermocouple was used to measure the vacuum flange downstream as a diagnostic for axial heat loss. These measurements were read using an OM-DAQPRO-5300 data logger, capable of recording every second, and exported for further analysis. The thermocouples were all placed outside of the coil region in order to avoid potential magnetic interference.

4.1.4 Uncertainty Analysis

Table 4.2 summarizes the errors for the various measurement instruments used in this work. Any combination of errors is done using the root sum square method, shown in Eq. (4.1).

$$\sigma_e = \sqrt{\sigma_{e1}^2 + \sigma_{e2}^2} \qquad (4.1)$$

All temperature measurements have a combined error that must take into ac-

count both the inherent error from the thermocouple as well as the error associated with the data logger. Uncertainties from repeated experimental measurements are taken to two standard deviations and are combined with the maximum instrument error among all individual measurements. Where applicable, a least squares regression analysis was done to help characterize the rate of heating in certain conditions. Since all instrument error is based on a percentage of the measurement and not a constant, it was necessary to conduct a weighted least squares, using the weights $w_i = \frac{1}{\sigma_i^2}$. A 95% confidence level on the fitted parameters, $b_{slope} \pm t \sqrt{(X^T X)^{-1} s^2}$ (only the slope is of concern here), was calculated, where t is the inverse of the Student's t cumulative distributive function, X is the design matrix, and s^2 is the mean squared error. In order to properly fit non-linear data, a forward rolling regression analysis was done where the fit parameters at a given time were dependent on a chosen interval of data in front of the current time. Further calculations requiring propagation of uncertainty will be addressed when appropriate throughout the paper.

Table 4.2: Error percentages for all instruments used in this study

Type	Instrument	Error
Temperature	Type K Thermocouple	$\pm$ 0.75%
Temperature	OM-DAQPRO-5300 datalogger	$\pm$ 0.5%
Flowrate	OMEGA FMA - 1600A	$\pm$ 0.5%
Pressure	MKS Model 972 (bell jar)	$< 1 \times 10^{-3}$ mbar: $\pm$ 30% $> 1 \times 10^{-3}$ mbar: $\pm$ 5%
Pressure	OMEGA DPG1000 (decomposition chamber)	$\pm$ 0.25%
Input Power	VOLTEQ HY5030	$\pm$ 1%
Inductance	Almost All Digital Electronics	$\pm$ 1%
Current	CWT Rogowski Current Transducer - Standard	$\pm$ 1%
Current	GW Instek GDS-2204 Oscilloscope	$\pm$ 3%

4.2 Results

Because only the housing is undergoing inductive heating, it was high priority to ensure good thermal connection between the housing and the heat exchangers. The general procedure was similar for all tests. First, the heat exchanger is pre-heated to temperatures above 1073 K using the power supply and the inductive heating circuit. Once the temperature was reached, the gas reservoir and the shut-off valves were opened for the respective gas being tested. Using the flow meter and valve upstream, the volumetric flow rate was set to at least 2 SLPM (taken at STP conditions). The temperature readings were monitored to see if decomposition occurred, typically indicated by a surge in gas temperature. Once the gas tempera-ture has risen past $\sim$1070 K, the power supply was shutoff to begin the steady-state tests.

4.2.1 Copper Metal Foam

The first heat exchanger tested was a 50 PPI, 80% porous open-cell copper metal foam; its the same metal foam that was modeled in Chapter 3 (Fig. 3.1). It is 0.88 inches (22.3 mm) in diameter and 2.5 inches (63.5 mm) long (same as the axial length of the induction coil). The effective surface area was not provided but was estimated from other manufacturers' tabulated data to be on the order of 6000 $\frac{m^2}{m^3}$ or 0.71 $\frac{m^2}{kg}$. Although this value is an approximation, it is still significantly less than the powder and granule catalysts typically used for thrusters. Because the metal foam is porous, it is not rigid and has some elasticity. This allowed for a strong

78

thermal connection between the low carbon steel housing and the metal foam.

Preliminary tests were successful in heating the foam outside of vacuum chamber to temperatures beyond 1100 K. Fig. 4.7 shows a cross-sectional view of the foam in the housing during heating tests. Unfortunately, tests for steady-state decomposition were not at all successful. Due to the fact that nitrous oxide is a natural oxidizer, it oxidized and degraded the metal foam. The degradation happened over just a few tests and therefore, no data were collected.

It is important to analyze how to mitigate the oxidation effects as they are analogous to catalyst degradation. Because some preheating tests were conducted outside of the vacuum chamber, there was some oxidation (due to the high temperatures) on the outer surface of the housing as well. For the low carbon steel used, scales formed on the outside and fell off very easily, reducing the structural integrity. This was addressed by ensuring that all future tests were conducted in the evacuated chamber with pressures always lower than 1 x 10^{-2} mbar (1 Pa).

Figure 4.7: Copper metal foam being heated inside the low carbon steel

Heating metals in a low pressure environment is known as vacuum tempering. Fig. 4.8 compares the effects of oxidation from two tests; one in a pressurized environment (1 mbar or 100 Pa) versus one in an evacuated chamber (1 x 10^{-3} mbar or 0.1 Pa).

Oxidation within the housing was a much more difficult problem to solve be-

(a) Heating in 1 mbar pressure environment

(b) Heating in a 1 x 10^{-3} mbar pressure environment
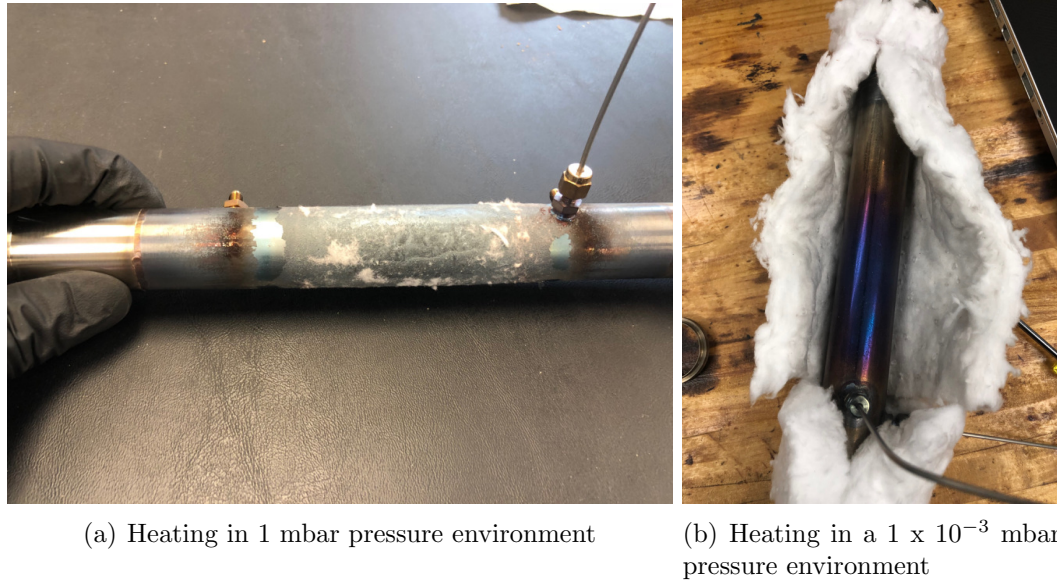
Figure 4.8: Differences in oxidation effects from heating in high/low pressure environments

cause nitrous oxide decomposition will always produce an oxygen-rich environment. Copper has two forms of oxidation, cupric oxide (CuO) and cuprous oxide (Cu_2O). Cupric oxide is a whisker layer that forms on top of cuprous oxide (with copper underneath). As these tiny whiskers form, structural integrity is reduced. It is understood that as the oxidation time is increased, the growth of the cuprous oxide middle layer tapers off at high temperatures whereas the cupric oxide layer continues to grow linearly [97]. For the copper metal foam, the relative thickness of the oxidation layer was on the order of the struts within the foam, resulting in significant reduction of structural strength. Therefore, the following alternate heat exchangers are designed to have more thickness (at the cost of effective surface area).

4.2.2 Copper Discs

A set of 16 copper discs, separated by copper spacers, was designed to address the aforementioned oxidation issues. Both the discs and spacers have a diameter slightly less than 22 mm (or 0.88 inch) such that they can fit inside the steel housing. The 16 copper discs are are split evenly among two designs, each being 3 mm thick with 15 x 1 mm radius holes. The difference between the two designs is the location of the 15 holes, as shown in Fig. 4.9. Design 1 has 15 holes on the outer edge of the disc whereas design 2 has them in a grid pattern close to the centerline. The spacers have an 18 mm inner diameter and are only 1 mm thick. This heat exchanger was designed specifically to address the thickness issues while maintaining tortuosity of the flow.

Fig. 4.10 shows how the discs were arranged and the nominal flow path of the gas assuming a strong seal between the discs and the steel housing. There are eight sets, with each set being a combination of two discs (one of each design) and two spacers. The entire length of the heat exchanger is approximately 2.5 inches (63.5 mm). The holes from both designs are not aligned with each other and therefore present a blocked channel without the use of spacer. This forces the gas to change direction and will ideally increase the heat transfer between the discs and the fluid.

The eight sets of discs were all inserted into a low-carbon steel housing, with the downstream side supported by the thermocouple. There was some concern, however, that the discs would tip over on the upstream side due to their small thickness. Therefore, a small stainless rod was welded to the housing and placed

81
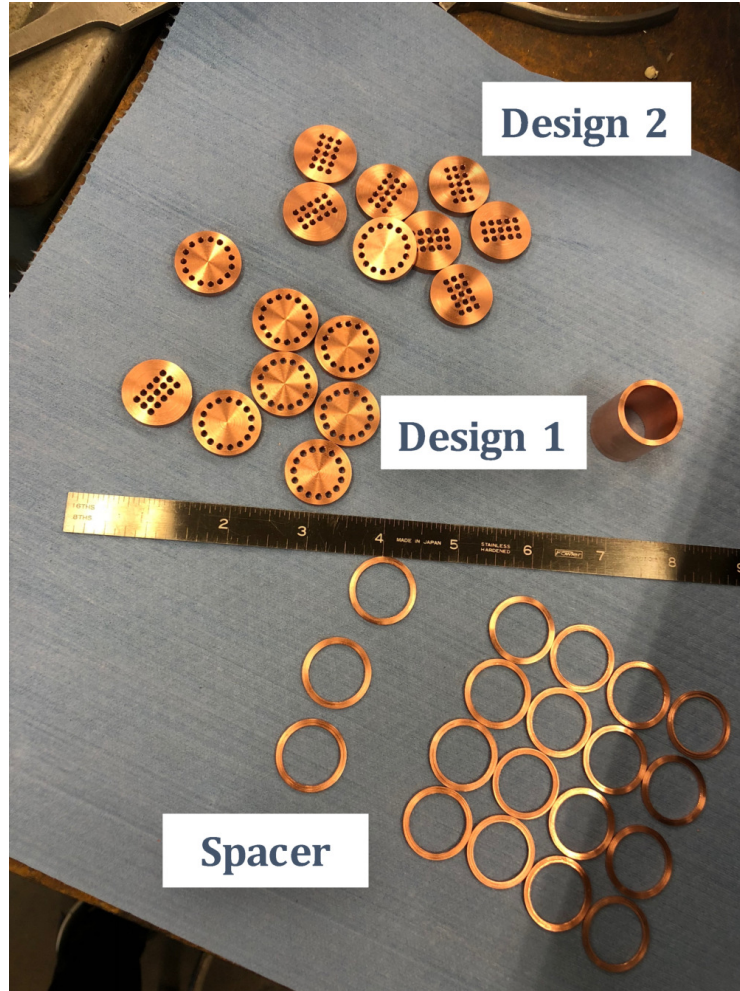
(a) Copper discs – both designs and spacer

(b) Design 1 schematic (mm)

(c) Design 2 schematic (mm)

(d) Spacer schematic (mm)
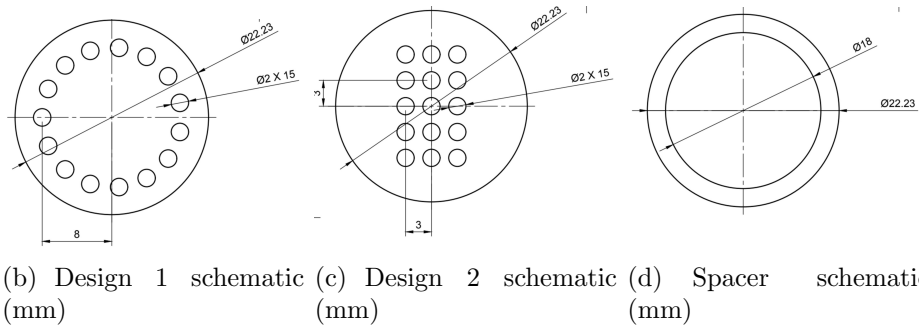
Figure 4.9: Second heat exchanger (16 copper discs separated by spacers)

perpendicular to the upstream face of the heat exchanger. Fig. 4.11 provides cross-sectional images of the upstream and downstream sides of the housing.

Before moving forward, it is instructive to compare the two heat exchangers
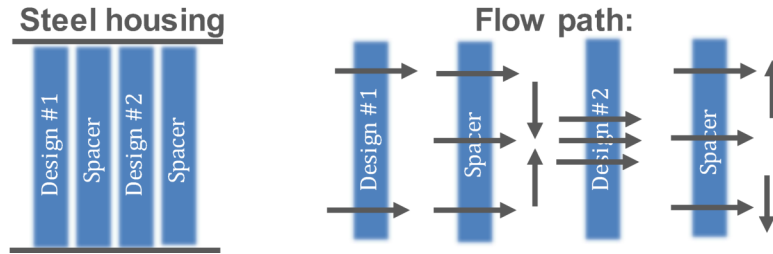
Figure 4.10: The order of copper discs inside the steel housing and the nominal flow path

(a) Upstream (stainless-steel rod support)
(b) Downstream (thermocouple)
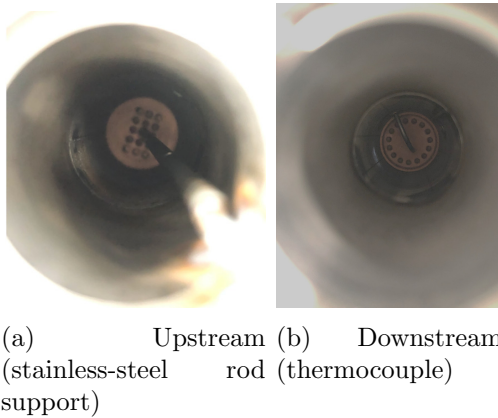
Figure 4.11: Inside the housing: upstream and downstream

mentioned against nominal catalysts. Table 4.3 identifies the effective surface area of the two heat exchangers and compares them to values found in literature for catalysts used in monopropellants. The effective surface area for the copper discs was calculated by simply taking the ratio of the surface area available (including the surface area of the holes) per bulk volume or mass. The porosity was also estimated to be 25% (volume of void divided by total volume). It is immediately apparent that the effective surface areas of the heat exchangers presented are much lower than the values typically expected in monopropellant thrusters. To reiterate, this connects back to the objective of this work which aims to reduce the dependency on a high effective surface area.

Table 4.3: Effective surface area of heat exchangers used in this study

Heat Exchanger	Effective Surface Area (σ)
Catalysts	1 - 80 $\frac{m^2}{g}$
Metal foam	0.7 x 10^{-3} $\frac{m^2}{g}$
Copper discs	0.1 x 10^{-3} $\frac{m^2}{g}$

Prior to testing, the chamber was first pumped down to 0.02 ± 0.001 mbar (2 $\pm$ 0.1 Pa). The temperatures for the copper discs, downstream gas temperature and downstream flange are plotted in Fig. 4.12 along with the errors associated with the instruments. It is important to acknowledge that the downstream gas temperature is an uncorrected measurement from the thermocouple. When measuring high gas temperatures, the values need to be calibrated in order to account for radiation losses. This correction can be solved for by conducting a power balance for the thermocouple. Assuming conduction within the thermocouple wires is relatively small, the heat-flux balance for the thermocouple is $h\,(T_{gas} - T_b) + \sigma_b\,(\epsilon_w\,T_w^4 - \epsilon_b\,T_b^4) = 0$ at steady-state. Here, h is the heat transfer coefficient between nitrous oxide and the thermocouple, T_b represents the measurement from the thermocouple bead and T_w represents the temperature of the surrounding walls, which is assumed to equal to the heat-exchanger's temperature. In order to solve for the actual gas temperature, the heat transfer coefficient and the emissivities need to be estimated. Because the system has a low Reynolds number, these parameters can have large effects on the gas temperature. Since the objective of this work was to study steady-state decomposition, it was not required to quantify the exact temperature of the gas since the corrected value will not affect the results or analysis. Therefore, the estimation
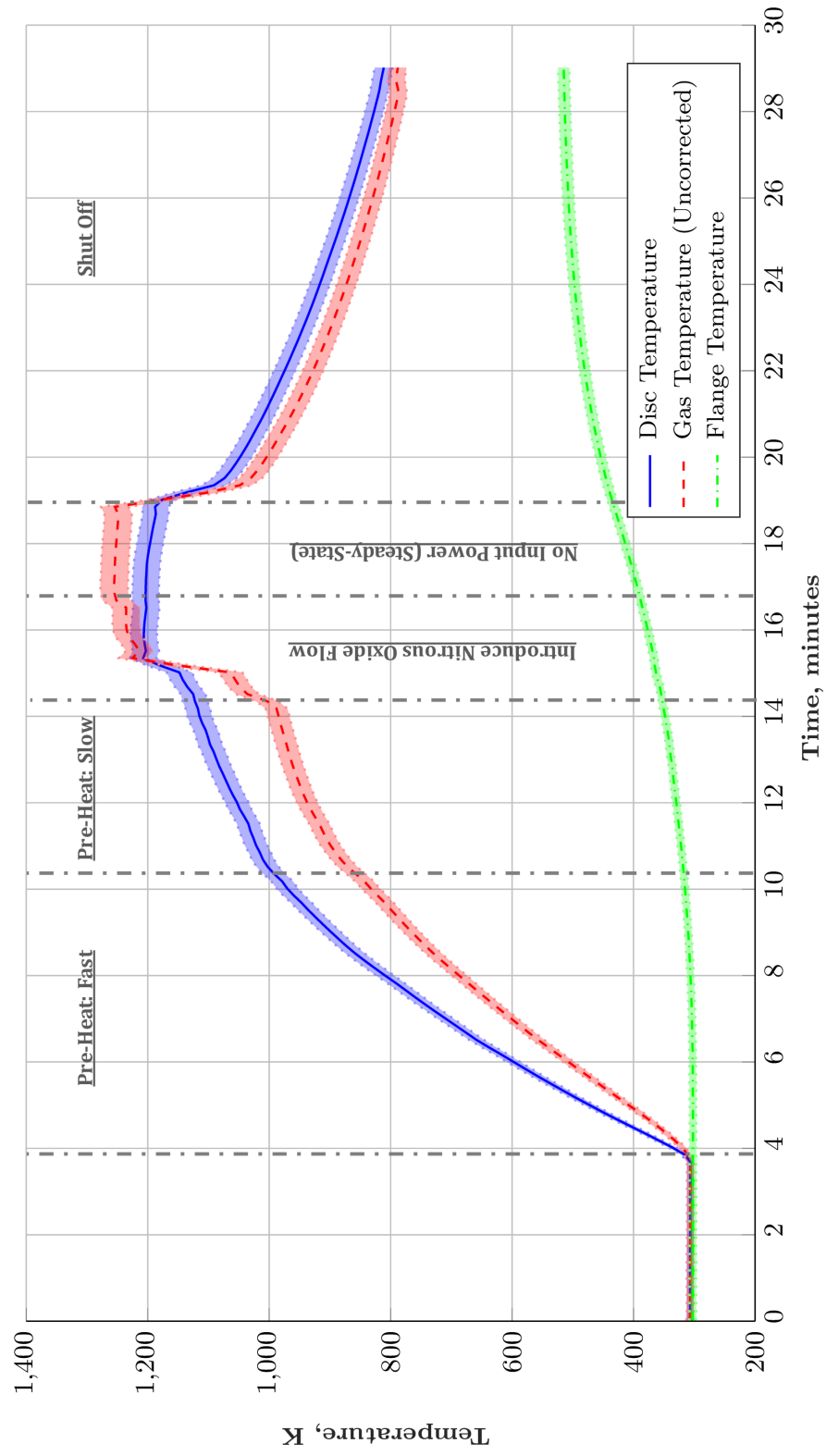
Figure 4.12: Nitrous oxide tests: low carbon steel housing/copper heat exchanger

of these parameters is considered outside the scope of this project.

4.2.2.1 Heating

As seen in Fig. 4.12, the pre-heating stage can be divided into two sections, each having a different rate of heating. The difference in the heating rate is due to the Curie temperature of the low carbon steel used, which according to the data is around 1000 K. The fast heating stage, occurring below the Curie temperature due to hysteresis effects, is able to inject more current into the workpiece for a constant voltage. In fact, the power supply was running at 15 ± 0.2 V, 35 ± 0.4 A, limited by the maximum current the circuit can handle. This translates to approximately 525 ± 8 W. Although this is the input power from the power supply, not all of this power is actually used for workpiece heating and a more appropriate value is calculated in later sections. Once the workpiece was heated past its Curie temperature, the voltage and current dropped to 30 ± 0.3 V, 16 ± 0.16 A and was then limited by the power supply.

To further quantify the effect of Curie temperature on heating, Fig. 4.13 plots the slope of the foam temperature throughout the heating stage. Because the heating stages are not linear, primarily due to the material losing magnetic properties as it heats up, a rolling weighted regression analysis was conducted using two minute bins. The slopes and the respective confidence intervals are collected and plotted in Fig. 4.13, starting at the four minute mark of the test and ending around the fourteen minute mark, which is the end of the preheating regime. What is evident is a gradual
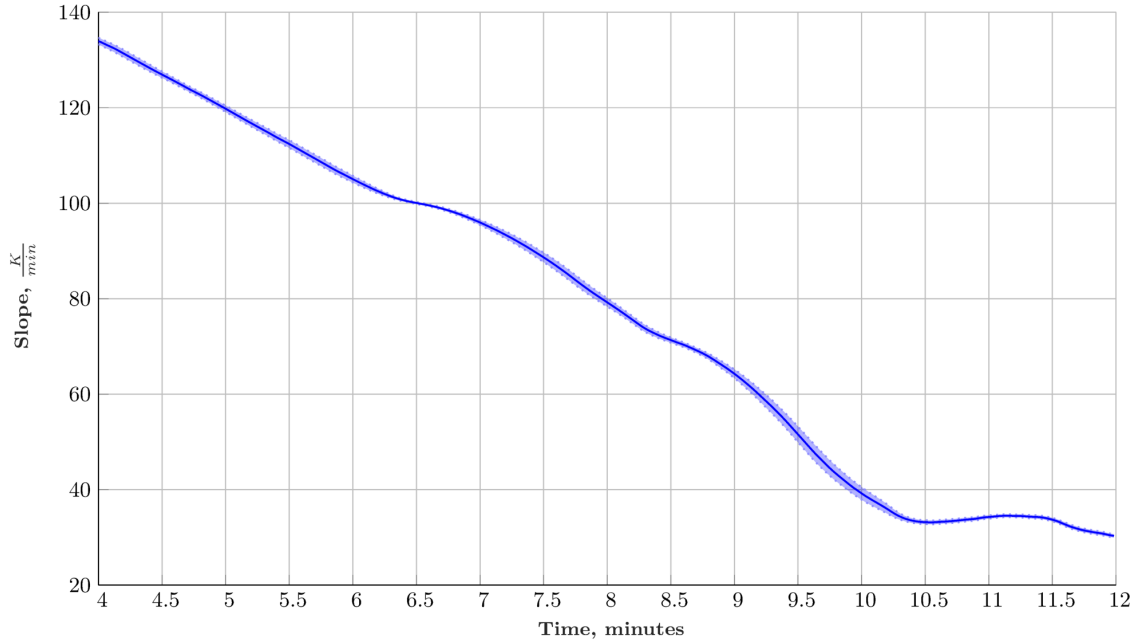
Figure 4.13: Rolling least squares regression analysis: slope during the pre-heating phase of the copper discs

decrease in the slope during the fast pre-heating stage (until the 10.5 minute mark) before plateauing to a constant rate of heating after crossing the Curie point. Below the Curie temperature, the hysteresis effects are prevalent but are diminishing as the material gets hotter. Once it crosses the temperature threshold, the material becomes nonmagnetic and the heating rate is relatively constant.

4.2.2.2 Steady-State

Once the copper discs reached a temperature close to 1000 K, nitrous oxide was introduced into the system at a volumetric flow rate of 2.0 ± 0.01 SLPM (~ 0.06 $\frac{g}{sec}$). This caused an exponential rise in downstream gas temperature, indicative of decomposition. As the temperature inside the chamber increases, so does the pressure, thereby reducing the pressure gradient between the upstream valve and the

chamber and affecting the nominal flow rate. The perturbations visible in Fig. 4.12 are due to the manual adjustments of the flow value to counter these fluctuations.

Once the gas temperature reached approximately 1250 K, the power supply was shut off in order to test for steady-state decomposition during a two minute time period. Fig. 4.12 shows a relatively flat temperature profile for both the discs and the gas within this region, expected for a steady-state profile. Further evidence for steady-state can be derived from comparing the average value and uncertainty to the maximum and minimum temperatures collected. The average discs and gas temperature within this region are 1198 ± 22 K and 1252 ± 23 K respectively. The maximum and minimum temperatures measured within this region for the discs are 1203 K and 1186 K. Similarly, the maximum and minimum temperatures measured for the gas are 1255 K and 1248 K. Because these temperatures are within the average uncertainty bounds for both gas and the discs, the results are a strong indication steady-state decomposition was achieved. At the end of two minute region, the shut-off valve for nitrous oxide was closed and a sharp decrease is visible in all temperatures as there is no longer an energy source. It is worth mentioning that the downstream flange temperature rises smoothly throughout the decomposition test before plateauing as the system cools off. This shows that the axial heat loss is not a fast response since no exponential energy release is identifiable within its profile over time.

Figure 4.14: Degradation of the copper heat exchanger inside the housing (downstream on right side)

4.2.2.3 Degradation

Although preliminary results showed successful decomposition, no subsequent tests were conducted as there was significant degradation to the heat exchanger. The degradation completely sealed the nominal flow path.

Fig. 4.14 shows the housing with a 1.5 inch (38.1 mm) cut out of the decomposition region. There are strong indications of both oxidation and melting of the heat exchanger, more prevalent on the downstream side (right side of the housing). This is of some concern since copper's melting point is around 1350 K, 150 K more than the peak temperature measured by the thermocouple. Recall that the locations of the thermocouple are heavily influenced by the axial location of induction coil, since the changing magnetic field can interfere with the temperature readings. The thermocouple used to measure the heat exchanger's temperature is placed downstream

Figure 4.15: Downstream O-ring failing due to the high temperatures

outside of the inductive heating region. Therefore, this measurement assumes that the entire heat exchanger is at this uniform temperature, an acceptable assumption considering copper's high thermal conductivity. Since there is such a huge discrepancy between the measured temperature and the melting temperature of copper, it is possible there might have been a thermal disconnect between the last copper disc downstream in contact with the thermocouple and the rest of the heat exchanger. This disconnect could have been exacerbated by oxidation as it continues to be significant throughout entire heat exchanger. Local temperatures at decomposition regions could exceed measured temperatures even if for a short interval as the energy is dissipated throughout the heat exchanger. Furthermore, the numerical model did produce results at higher gas densities in which the temperature within the heat exchanger exceeded copper's melting point. If a thermal disconnect did occur, it is entirely plausible the heat exchanger exceeded 1350 K. Due to these uncertainties, it is beneficial to use heat exchangers with higher melting points and stronger resistance to oxidation.

In addition to the heat exchanger, there is some motivation to re-design the housing as well. As shown in Fig. 4.12, the downstream flange temperature exceed 500 K by the end of the test. The KF-25 flanges all require a rubber O-ring to help make a seal. Unfortunately, these O-rings have melting points lower than 500 K and started to lose rigidity by the end of the test. This made it difficult to maintain a seal between the decomposition chamber and the evacuated bell jar. Fig. 4.15 shows the downstream O-ring partially melted due to the hot gas flowing downstream during decomposition.

4.2.3 Stainless-Steel Discs

In an effort to address the partial melting found with copper discs, the third heat exchanger fabricated was a set of stainless-steel discs. The transition only focused on the material and therefore still had the same physical specifications as the copper discs setup (see Fig. 4.16).

Stainless steel was chosen because of its high melting point and resistance to high temperature oxidation and corrosion. The melting point, around 1650 K, is substantially higher than copper's and should be able to withstand any localized spikes in temperature due to decomposition. Its resistance to oxidation at high temperatures ($\sim$1000 K) is a result of chromium in the alloy. The chromium initially oxidizes on the surface of the metal, forming chromium oxide (Cr_2O_3). This acts as a protective layer due to the low diffusion constants for oxygen and metal ions [98].

The housing however, had to be completely modified in order to address the

Figure 4.16: Comparison between copper (left) and stainless-steel (right) heat exchangers

limitations from the O-rings. Instead of the KF-25 flanges, the system now incorporates Conflat (DN25CF) flanges that use copper gaskets to create a seal. In order to accommodate this modification, a 304L stainless-steel housing was adopted with the same dimensions as the low carbon steel. Preliminary high temperature heating tests showed successful reduction of oxidation as expected. Other than some discoloration on the surface, there was no formation of scales or any reduction in structural integrity even in a pressurized environment.

4.2.3.1 Nitrous Oxide

A total of three nitrous oxide tests were conducted using the stainless-steel discs. The heat exchanger was first pre-heated to approximately 1073 K before running three tests sequentially. Similar to the results from the copper heat exchanger, each run shows a large increase in temperature as the flow was turned on, a steady-

state temperature profile as the input power was tuned off, and rapid cooling of the entire system when the flow was turned off. There was some heating in between tests to raise the heat exchanger's temperature back to ~1073 K to maintain similar testing conditions. Fig. 4.17 plots the temperature measurements recorded for all three tests.

Considering that 301 stainless steel is austenitic, it is expected that there is no additional heating effect due to hysteresis. The heating phase for the stainless-steel housing took almost 18 minutes for the discs to reach a temperature above 1050 K, six minutes longer than that for the low-carbon steel housing. In order to compare the heating rates between the low carbon steel and the stainless-steel housing, Fig. 4.18 plots the results of a rolling weighted least squares analysis of the heating phase using two minute bins. Here, the maximum heating rate is no more than 55 $\frac{K}{min}$, much less than the heating rate achieved using the low-carbon steel housing (before Curie temperature). The local maxima within the heating profile can be attributed to small manual adjustments in the power supply as the workpiece is heating up. However, at high temperatures (beyond the Curie point for low carbon steel), the heating rates are in close agreement with each other since the resistivities and relative permeabilities are almost equal.

All three runs attempted to maintain steady-state decomposition within a two minute interval, identified from when the input power was turned off to when the flow value was closed. The temperature profile of the downstream flange matches the profile generated for the copper heat exchanger test. Table 4.4 summarizes key characteristic temperatures and system parameters for each run along with the
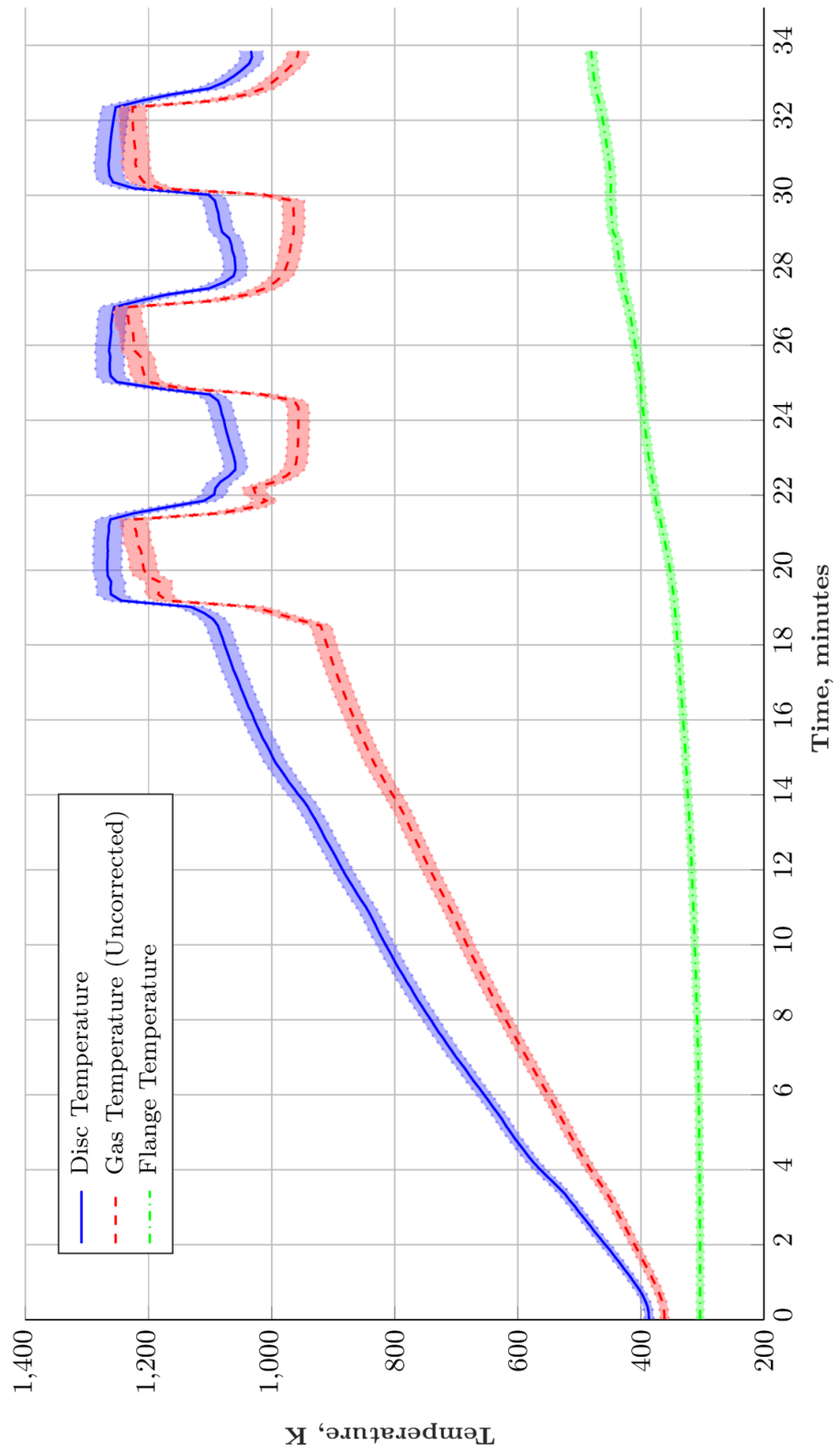
Figure 4.17: Nitrous oxide tests: stainless-steel housing/stainless-steel heat exchanger
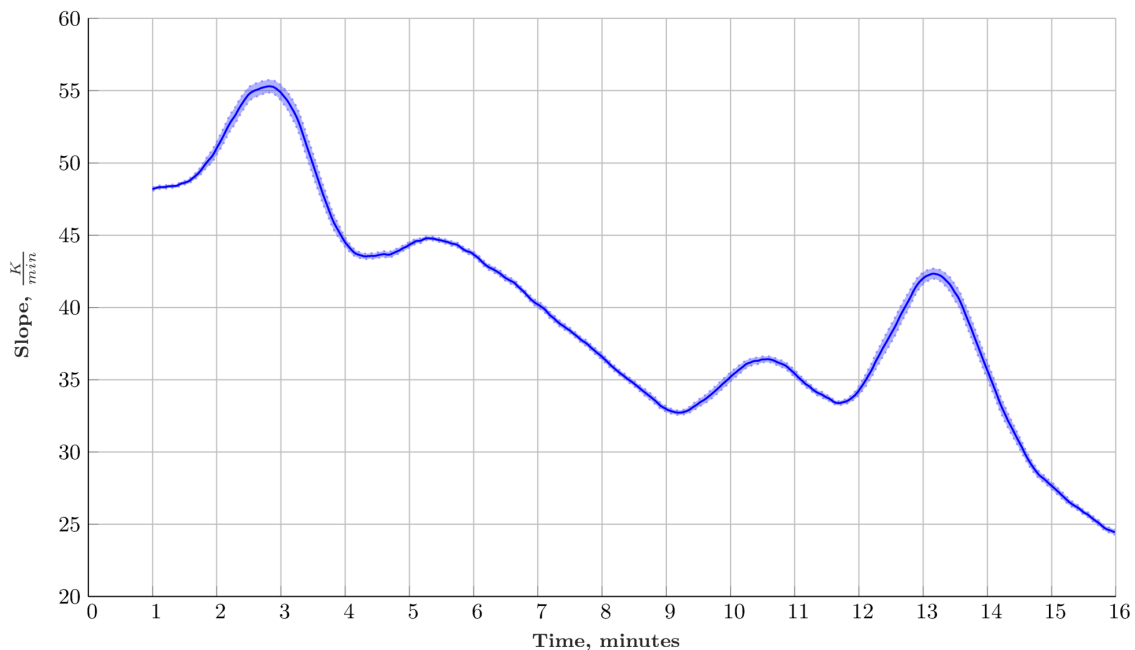
Figure 4.18: Rolling least squares regression analysis: slope during the pre-heating phase of the stainless-steel discs

associated individual instrument errors. It is also helpful to calculate the mean of each of these values as well as the combined experimental uncertainty from all the runs.

The volumetric flow rate and steady-state duration were relatively constant for all three runs. Variations in the flow rate did occur, primarily due to fluctuations in pressure inside the decomposition chamber. The pressure values inside the decomposition region are comparable to other experiments studying nitrous oxide decomposition [6]. Once the temperature of the heat exchanger reached close to 1088 K, nitrous oxide was introduced into the channel. Because these temperatures are close to the thermal decomposition temperatures, the nitrous oxide gas begins to decompose immediately, shown by the quick rise in temperature. On average, both the measured gas and heat exchanger temperatures increase by almost 200 K

Table 4.4: System measurements and characteristic temperatures for the stainless-steel heat exchanger tests with nitrous oxide

	Run #1	Run #2	Run #3	Combined
System Measurements				
Flow rate (SLPM)	2.5 ± 0.05	2.6 ± 0.05	2.7 ± 0.05	2.6 ± 0.2
Total time for steady state (min)	2.08	2.0	2.1	2.06 ± 0.1
Decomposition chamber pressure (Psig)	45 ± 0.1	47 ± 0.1	45.3 ± 0.1	45.7 ± 2.1 ($3 \times 10^2 \pm 14$ kPa)
Characteristic Temperatures (K)				
Introduce N_2O	Discs: 1087 ± 20 Gas: 920 ± 17	Discs: 1085 ± 20 Gas: 950 ± 17	Discs: 1092 ± 20 Gas: 965 ± 17	Discs: 1088 ± 21 Gas: 947 ± 51
Turn off input power	Discs: 1257 ± 23 Gas: 1180 ± 21	Discs: 1251 ± 23 Gas: 1199 ± 22	Discs: 1249 ± 23 Gas: 1200 ± 22	Discs: 1252 ± 24 Gas: 1193 ± 31
Average steady state temperature	Discs: 1265 ± 23 Gas: 1208 ± 21	Discs: 1261 ± 23 Gas: 1221 ± 22	Discs: 1260 ± 23 Gas: 1221 ± 22	Discs: 1262 ± 23 Gas: 1216 ± 28
Maximum temperature (steady state)	Discs: 1268 Gas: 1224	Discs: 1264 Gas: 1234	Discs: 1265 Gas: 1227	Discs: 1266 ± 3 Gas: 1228 ± 10
Minimum temperature (steady state)	Discs: 1257 Gas: 1181	Discs: 1252 Gas: 1120	Discs: 1249 Gas: 1201	Discs: 1252 ± 8 Gas: 1193 ± 22

within a one minute interval. Once the discs reach a temperature close to 1250 K, the input power was turned off. For all three tests, the maximum and minimum temperatures measured within the steady-state regime are all within the uncertainties of the average steady-state temperature. Therefore, it is reasonable to conclude that steady-state decomposition was achieved for all three runs within the tested two minute interval.

From Fig. 4.17, however, it is evident that the temperatures do fluctuate, although within the uncertainty bounds, during the steady-state regime. Fig. 4.19 plots the slopes and uncertainty from a rolling least squares analysis for both the gas and heat exchanger throughout the steady-state regime. The heating rates are plotting across a two minute forward window for all three runs. One aspect to mention is the recurring local maxima throughout the heating rate profile. These maxima are the direct result of manual adjustments to the flow rate overshooting the desired value. The fact that the local maxima are existent on both heating profiles and occur at the same time further support this claim. While the slopes for the gas temperature are all above zero, the slopes for the heat exchanger's temperature dip below zero. This suggests that although a local steady-state solution was achieved, self-sustained decomposition over a longer time interval might not be sustainable with the current configuration. One way to address this is to increase the flow rate and thereby increase the energy released from decomposition. In general, it seems unlikely that steady-state decomposition can be achieved for long durations using a passive flow rate control. A feedback control system with the ability to change the flow-rate depending on system heating is probably required when attempting to run

for longer durations.
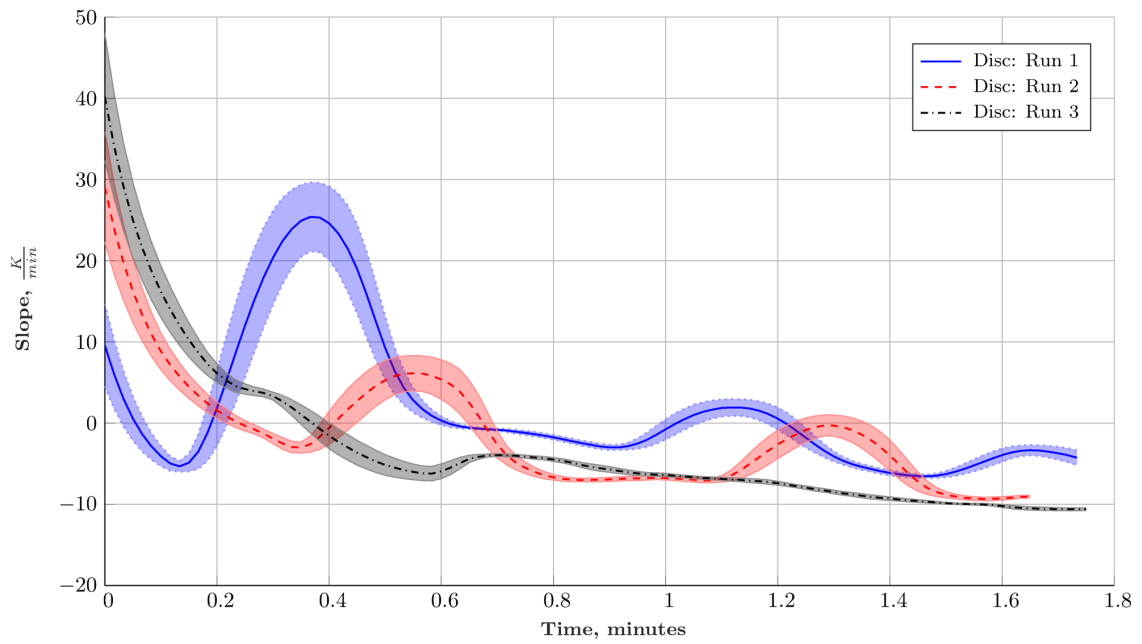
(a) Disc temperature heating rates
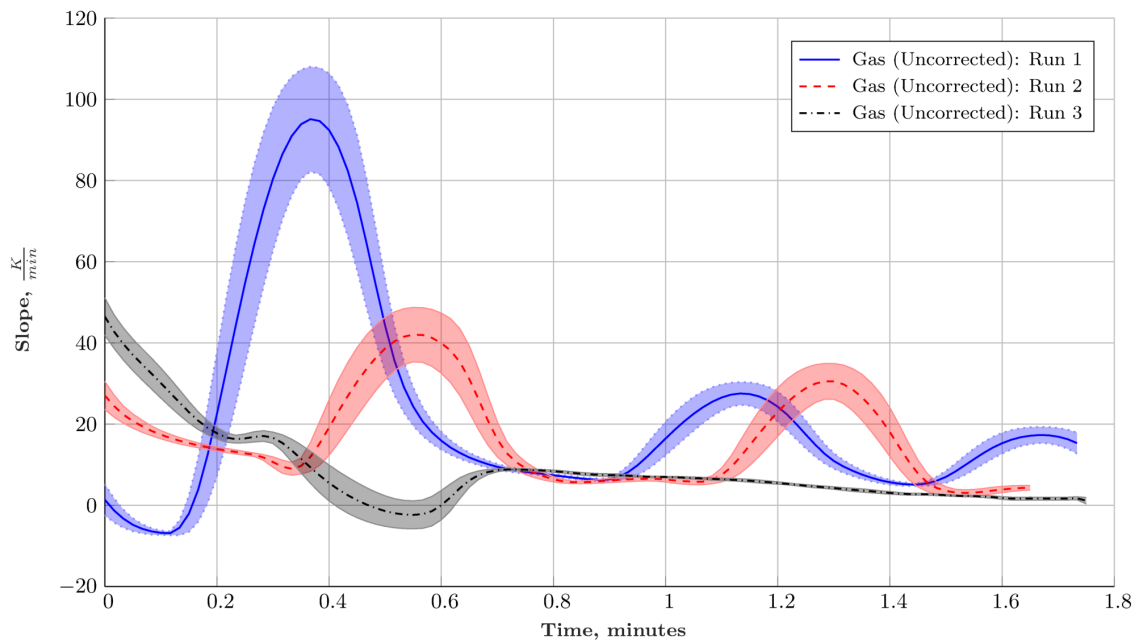
(b) Gas temperature heating rates

Figure 4.19: Rolling least squares regression analysis: slope during the steady-state regime for all three runs of nitrous oxide

4.2.3.2 Carbon Dioxide

Three tests with carbon dioxide were conducted in a similar manner to nitrous oxide, with the flow only being introduced once a threshold disc temperature was reached. While the first was conducted prior to nitrous oxide tests with the initial pre-heating phase, the rest were conducted sequentially after the nitrous oxide tests (system was already near the desired temperatures). The temperature measurements from the three tests are shown in Fig. 4.20.

For all three runs, it is evident that there was no exponential energy release with the introduction of carbon dioxide. This was expected as carbon dioxide does not exothermically decompose at these temperatures. Flow rate was set to approximately 2.5 ± 0.02 SLPM for each of the tests and underwent minimal variation. Instead of a constant two minute interval for decomposition, each of the tests was run without any power source until temperatures dropped below the threshold temperature at which carbon dioxide flow was initially introduced. The third test was run at a lower input power to limit the temperature of the heat exchanger to ~ 1080 K, close to the 1088 K for the nitrous oxide tests before input power was turned off. This eliminated the effects of inductive heating on the system temperature and further confirmed that decomposition did not occur. The small increase in temperature the instant carbon dioxide was first introduced is probably due to flow mixing in the channel and does not represent any external power source. The decomposition chamber pressure was not recorded as it was much lower than the pressure measured with nitrous oxide decomposition. Table 4.5 shows the characteristic temperatures
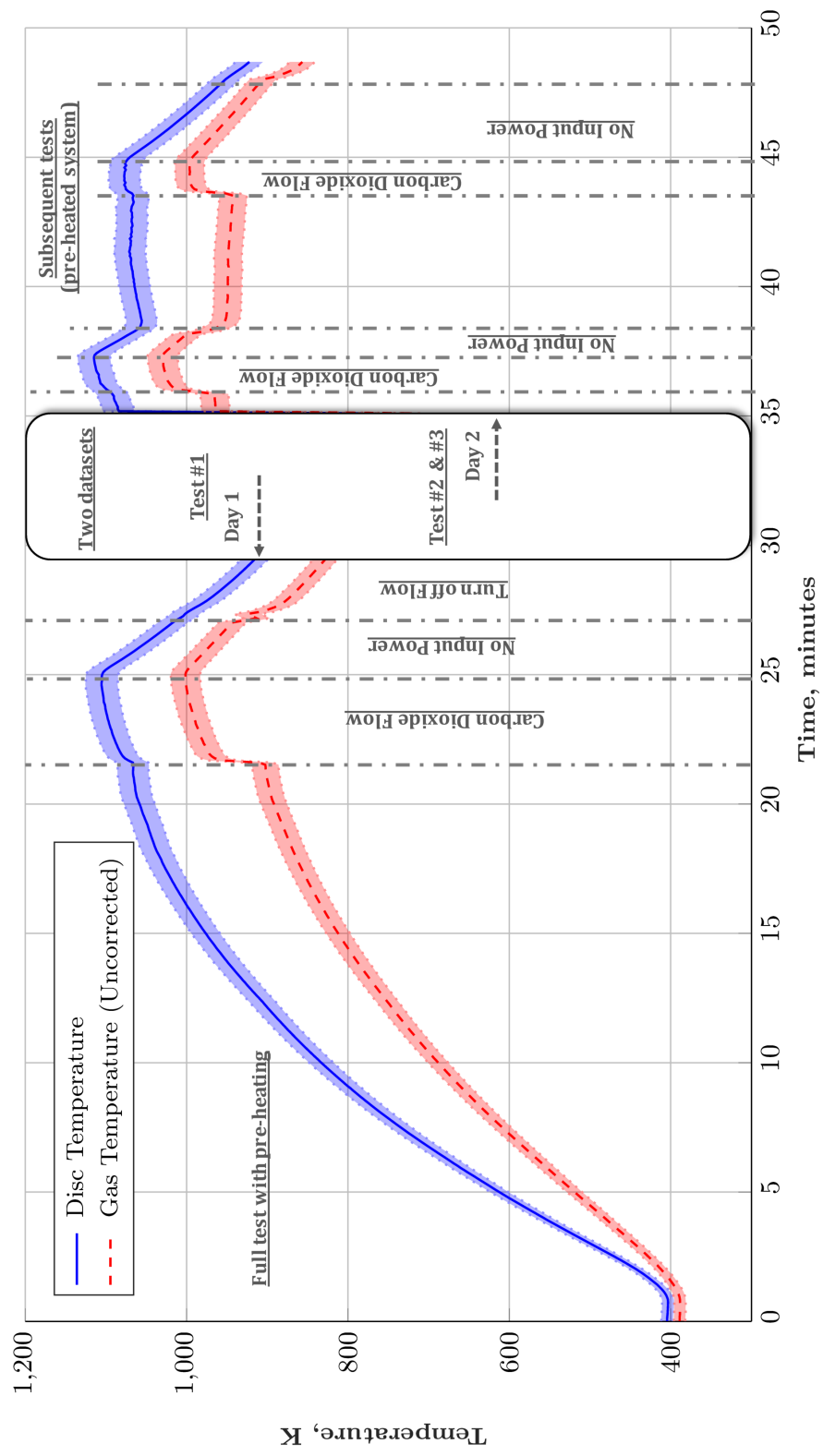
Figure 4.20: Carbon dioxide tests: stainless-steel housing/stainless-steel heat exchanger

for the carbon dioxide tests. The threshold temperature at which carbon dioxide was introduced into the system is in agreement with the nitrous oxide tests. However, the average temperature for both the gas and the heat exchanger at which input power was turned off is about 100 degrees less than that of the nitrous oxide tests. This is indicative of a lack of any decomposition for carbon dioxide. The large values for the combined uncertainties from the experimental tests are a result of the third run being at a lower power. Nonetheless, all three runs produced maximum and minimum temperatures that are all outside the range of the average temperature and uncertainty within the no input power regime.

Similar to the nitrous oxide tests, it is beneficial to study the rate of heating within the zero input power region. Fig. 4.20 shows a steady decrease in all temperature measurements as soon as the input power is switched off and there is no longer a power source. This can attributed to advective cooling as the cold carbon dioxide gas removes heat from the heat exchanger as it exits through the system. Because the time interval for no input power region varied for each test, a one minute window (third test was shorter than one minute) was selected for which the rate of heating for both the gas and the heat exchanger were plotted using the rolling regression analysis. These results are plotted in Fig. 4.21. The heating rates in both of these plots are always negative, showing that there is a steady decrease of both the gas and the heat exchanger temperatures. Furthermore, the magnitudes of the values are much higher than the ones found in Fig. 4.19, showing that the carbon dioxide system is much farther from steady-state than that of nitrous oxide.
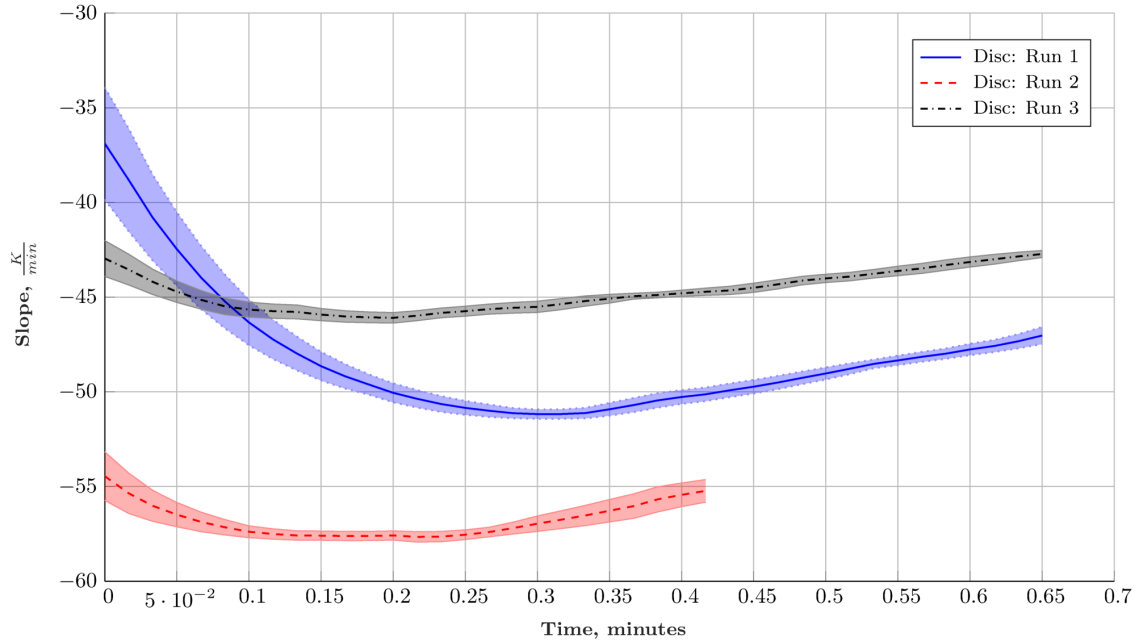
(a) Disc temperature heating rates
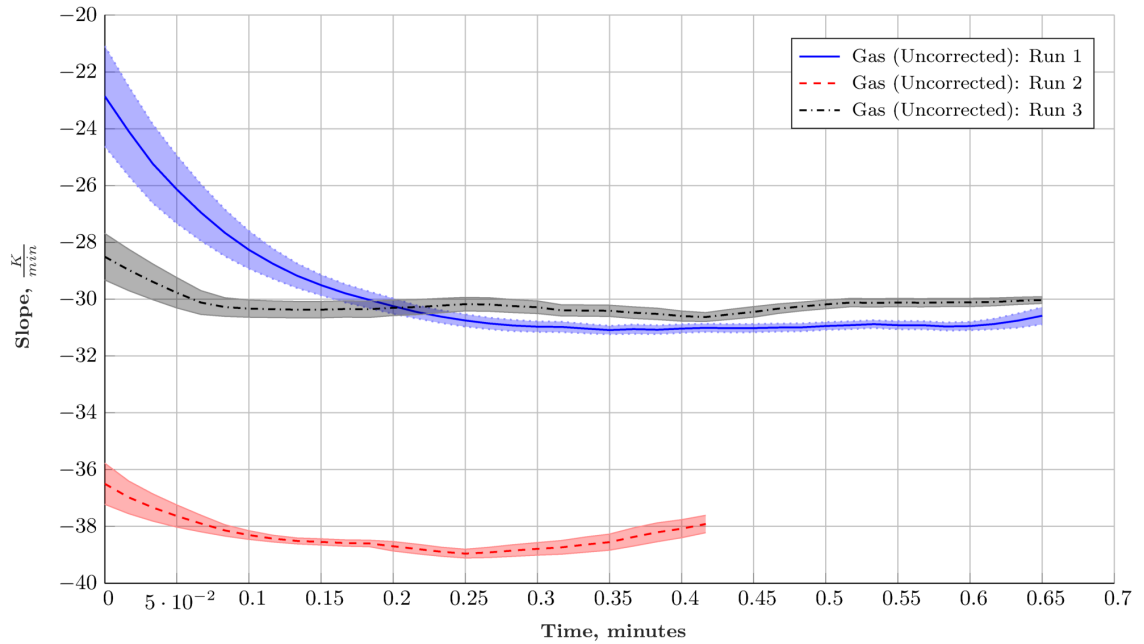
(b) Gas temperature heating rates

Figure 4.21: Rolling least squares regression analysis: slope during the no input power regime for all three runs of carbon dioxide

Table 4.5: Characteristic temperatures for the stainless-steel heat exchanger tests with carbon dioxide

	Run #1	Run #2	Run #3	Combined
System Measurements				
Total time for steady state (min)	2.03	0.8	3.1	2 ± 2.3
Characteristic Temperatures (K)				
Introduce CO_2	Discs: 1066 ± 19 Gas: 902 ± 16	Discs: 1092 ± 20 Gas: 1066 ± 17	Discs: 1066 ± 19 Gas: 942 ± 17	Discs: 1075 ± 36 Gas: 937 ± 667
Turn off input power	Discs: 1105 ± 20 Gas: 1001 ± 18	Discs: 1113 ± 20 Gas: 1029 ± 19	Discs: 1073 ± 19 Gas: 995 ± 18	Discs: 1097 ± 46 Gas: 1008 ± 40
Average temperature (no input power)	Discs: 1060 ± 19 Gas: 973 ± 18	Discs: 1092 ± 20 Gas: 1015 ± 18	Discs: 1009 ± 18 Gas: 950 ± 17	Discs: 1054 ± 86 Gas: 979 ± 68
Maximum temperature (no input power)	Discs: 1105 Gas: 1002	Discs: 1113 Gas: 1029	Discs: 1073 Gas: 995	Discs: 1097 ± 42 Gas: 1008 ± 36
Minimum temperature (no input power)	Discs: 1016 Gas: 940	Discs: 1071 Gas: 999	Discs: 951 Gas: 903	Discs: 1013 ± 120 Gas: 947 ± 97

4.2.3.3   Power Analysis

Although the power supply does output a digital reading of its voltage and current, only a fraction of this power is deposited into the workpiece. In fact, during the tests with both nitrous oxide and carbon dioxide, there were huge thermal losses within the circuit itself that reduced the net power available for heating the workpiece. These losses were more evident during the long heating times required for the austenitic stainless-steel housing. At times, there was localized heating on the circuit board that caused the solder to melt, disconnecting capacitors.

In order to try to cool the board, a small 1" x 1" x 1.25" (25.4 mm x 25.4m x 31.8 mm) copper block with water cooling (Fig. 4.22) was placed on the board to help remove a few watts. Although not efficient, simply placing the block on the circuit board was enough to keep the solder from melting during the long heating times for this work.

Figure 4.22: Copper block used to help dissipate heat from the inductive circuit

The actual power deposited into a workpiece through inductive heating can be complicated depending on the geometry of the workpiece, non-uniformity of the magnetic field and the coupling between the induction coil and the workpiece. There are, however, analytical functions to give approximate values of the induced power for common workpiece geometries. The following equation (Eq (4.2)) for workpiece power with a tubular geometry is adapted from Ref. [99].

$$P_w = 2\,\pi\,f\,p_{tube}(\pi\,r^2\,l\,)H_s^2\,\mu_o\,\mu_{rel} \tag{4.2}$$

Here, H_s is the magnetic field strength at the surface of the housing and is assumed to be equivalent to the magnetic field strength produced by an ideal solenoid ($\frac{IN}{l}$). Because the induction coil is not a perfect solenoid, the effective number of turns N was estimated using a measured value of the inductance. Using an Almost All Digital Electronics L/C Meter IIB, the inductance was measured to be $0.75 \pm 0.0075\ \mu Hy$. With a 1 inch (25.4 mm) inner radius, 2.5 inch (63.5 mm) long coil, the effective number of turns for the induction coil was 4.5 ± 0.5 (using $L = \mu_o \frac{N^2 A}{l}$). The volume term in Eq. (4.2), $\pi r^2 l$, is assumed to be of a solid rod of the same dimensions as the stainless steel decomposition region. The effects of a tubular geometry are absorbed into the dimensionless constant p_{tube}, determined from tabulated data in Ref. [99] based on system parameters. Given a thickness to diameter ratio of 0.12 and a diameter to skin-depth fraction of 17.9, p_{tube} is approximately 0.13. The current through the induction coil was measured using a Ragowski coil connected to an oscilloscope. Taking into account errors from both instruments, the current measured was 104 ± 2 A at a frequency of 86 ± 0.86 khz. In order to account for propagation of uncertainty for the following power calculations, all standard deviations were combined using the form $\sigma_f = |f|\sqrt{(\frac{\sigma_A}{A})^2 + (\frac{\sigma_B}{B})^2}$ with any covariances assumed to be zero. Furthermore, uncertainties in the physical dimensions were assumed negligible in comparison to errors in measurements and errors in the overall approximation for power. With relative permeability μ of 1 for

stainless steel and μ_o equal to (4π) x 10^{-7}, the power induced into the workpiece is 143 ± 10 W.

This power value calculated represents the total power deposited into the workpiece during the heating phase. One argument for steady-state can be based on the power deposited into the system from decomposition (P_{dcp}). Essentially, if P_{dcp} is large enough to replace the initial power source P_w, then the system should maintain a steady-state profile. The power generated from decomposition is relatively easy to calculate and is shown in Eq. (4.3). The energy density for nitrous oxide decomposition (Q_d) is $\sim 82 \frac{kJ}{mol}$. Using the combined volumetric flow rate from all three runs recorded in Table 4.4 at STP conditions ($\rho = 1.94 \frac{kg}{m^3}$), P_{dcp} is equal to 157 ± 12 W. Since the net power from decomposition is greater than the power induced into the workpiece, its reasonable to confirm, at least from a power balance standpoint, that steady-steady decomposition can be achieved.

$$P_{dcp} = \dot{m}\,\rho\,(MW_{N_2O})\,Q_d \qquad (4.3)$$

During the steady-state regime, a fraction of the available power is required to heat the incoming cold nitrous oxide gas to thermal decomposition temperatures. With P_{gas} representing this power required, the power balance now becomes the expression $P_{dcp} = P_{gas} + P_{lh}$ where P_{lh} captures all the heat loss for decomposition chamber and housing. Eq. (4.4) provides an approximate calculation for the amount of power required to heat incoming nitrous oxide gas (assumed to be at 273 K) to the average combined temperature at which nitrous oxide was introduced, as shown

106

in Table 4.4.

$$P_{gas} = \dot{m}\,Cp\,(T_{gas} - 273) \qquad (4.4)$$

At a constant specific heat capacity of 880 $\frac{J}{Kg-K}$, the power required to heat the gas to ~ 947 K is 50 ± 5 W. This results in approximately 107 ± 13 W of power lost across the system (minus the circuit), which is almost 70% of the power released from decomposition. Since this is a significant percentage of power available, a better heat loss analysis is required to properly understand where all the power is going and how to properly utilize all of it. In theory, the power loss estimated from the nitrous oxide tests should be the same for the carbon dioxide tests as long as the temperatures are approximately equal. From Fig. 4.21, the average heating rate for the disc temperature when carbon dioxide was first introduced is -44 $\pm$ 2 $\frac{K}{min}$. Using a nominal value for the specific heat capacity of stainless steel and an approximated total mass of the heat exchanger, the power loss across the system for the carbon dioxide tests is 97 ± 5 W. This value is within the uncertainty of the power loss estimated for nitrous oxide tests and further supports that tests with nitrous oxide did reach steady-state decomposition.

Using the derived power loss value, it is easy to calculate the amount of power lost through the inductive circuit. As mentioned above, a copper block had to be implemented to dissipate some of the heat from the circuit during long heating times. Near the end of the heating phase where the system is close to the measured steady-state temperatures, the power balance is $P_{crc} = P_w + P_{lh} + P_{lc}$, where P_{crc} is the

net input power from the DC power supply when the workpiece is being heated and P_{lc} is the unknown power loss term for the circuit. The circuit, without a workpiece, draws 5 ± 0.1 A at 31 ± 0.6 V. When the stainless-steel housing is inserted, the required current jumps to 14 ± 0.3 A at the same voltage. Subtracting the currents and multiplying by the voltage provides the net power into the circuit for workpiece heating, which is approximately 279 ± 11 W. Following the power balance stated above, the power being dissipated as heat through the inductive circuit is 29 ± 20 W. Although there is a high error for this estimation, the fact that the circuit board was getting hot enough to melt solder indicates that power loss is still substantial. The entirety of the power analysis suggests more research and development needs to be directed toward the inductive circuit and its efficiency towards heating the workpiece.

Chapter 5:   Feasibility of An Inductively-Heated Nitrous Oxide Thruster

5.1   Scaling from Simulated and Laboratory Set-Up

The mass flow rates simulated in the numerical model ($\sim$0.01 $\frac{g}{s}$) as well as the ones tested in the laboratory experiment ($\sim$0.08 $\frac{g}{s}$) are all lower than typical mass flow rates found in monopropellant thrusters. For example, 1N hydrazine monopropellant thrusters from Aerojet operate with flow rates between 0.09 - 0.5 $\frac{g}{s}$. The flow rates tested in this work were primarily selected based on the capabilities of the bench-top set-up, not for matching performance. Therefore, it is necessary to understand how to scale the experimental system in order to compete with existing thrusters. The Damköhler number was one metric found to be helpful in understanding how to scale the length of the decomposition chamber in order to properly handle higher flow rates. Recall that the dimensionless number is a ratio between the fluidic timescales and reaction timescales for decomposition. The higher the number (greater than 10 is ideal), the greater the conversion percentage of nitrous oxide. In Chapter 3, the implications on the physical dimensions of the decomposition chamber due to increasing the mass flow rate were discussed. The example focused on raising the mass flow rate to $\sim$ 0.13 $\frac{g}{s}$ in order to match that of an already-flown nitrous oxide thruster. The analysis concluded that an increase in the

length and area of the decomposition region along with an increase in initial gas density would properly accommodate the higher flow rates while maintaining a high D_n.

According to the continuity equation $\dot{m} = \rho\, u\, A$, the mass flow rate of a system can be increased by changing the effective cross-sectional area, the gas velocity or the gas density. Therefore, one could argue that by increasing only the gas velocity, and thereby increasing the length of the system (to keep the Damköhler number over one), the mass flow rate can be raised. This, however, would result in an unrealistic physical thruster. Consider the case mentioned above, where the mass flow rate was increased by more than a factor of 10. Keeping the Damköhler number, the resulting decomposition chamber would have to be ten times longer ($\sim$25 inches or 635 mm) to accommodate the increased gas velocity. This system would be much larger than existing monopropellant thrusters functioning at similar flow rates. A similar scenario can be presented with the cross-sectional area of the decomposition chamber. Therefore, the more realistic option is to increase all three parameters to produce a higher mass flow rate. For the 0.13 $\frac{g}{s}$ mass flow rate, the solution presented increased the length by a factor of 1.5, the area by a factor of 4 and the gas density by a factor of 2. The resulting decomposition chamber was still of reasonable size compared to existing thrusters.

In general, scaling the laboratory set-up to match existing thruster performance requires the use of both the Damköhler number and numerical simulations. Although the dimensionless number provides an initial confirmation that decomposition is possible, it is still important to use the numerical model to further test the

specific set of system conditions. The two main criteria to consider when scaling up the experiment is to maintain a high D_n and keep the physical dimensions comparable to other thrusters. Although the numerical model was validated against heating experiments using foam, it was not tested against any nitrous oxide decomposition results. It is therefore important to compare the numerical model with collected data to ensure it is a viable tool for thruster scaling.

Simulating the stainless-steel discs in the model was relatively easy since only the estimated effective surface area, porosity and physical dimensions were necessary. The main fluid parameters that need to be calculated are the inlet boundary conditions for density and velocity. Instead of finding some combination of density and velocity that matches the flow rate, it is more appropriate to first calculate the gas density using the recorded decomposition chamber pressure and in turn use that to quantify the gas velocity. From Table 4.4, the averaged decomposition chamber pressure is 45.7 ± 2.1 Psig (315 ± 14 kPa). Assuming that the gas temperature before it enters the hot region from the pre-heated heat exchanger is room temperature, the calculated density using the ideal gas law is $7.5 \frac{kg}{m^3}$. The solutions for these inlet conditions, however, produced downstream gas and heat-exchanger temperatures much larger than measured temperatures. From Chapter 4, it was estimated that a significant portion of the decomposition energy is being dissipated across the system. The heat loss component in the simulation, modeled by Eq. (3.16), only captures the radiative heat loss in the radial direction. Since the ceramic wool used for insulation has a low thermal conductivity, the power lost to radiation in the chamber is small. Therefore, the model does not account for any power dissipated

axially along the chamber, which seems to be the dominant heat loss for this system. A consequence of this approach is producing solutions that overestimate the temperatures within the system. Future modifications to the model should focus on adding more complexity to the heat loss component. Nonetheless, the model is still a vital tool for scalability as onset of decomposition is still dependent on a variety of parameters.

5.2 Comparing Performance

The downstream gas temperature, for both heat exchangers and catalysts, determines the maximum specific impulse achievable. Since no nozzle characteristics have been identified in this work, it is easier to compare performances assuming full expansion, where all of the thermal energy is assumed to have been converted to kinetic energy. Following the equation $h_o = \frac{1}{2}u^2$, where $h_o = Cp\,\Delta T$, the maximum specific impulse is 211 seconds. For the experiments using nitrous oxide, the estimated specific impulse at full expansion is 169 ± 23 seconds. Although this specific impulse is much lower than the maximum achievable (and lower than typical hydrazine thrusters), the exit gas temperature can be increased by changing the gas density (and mass flow rate). Uncertainty analysis for the following calculations is done using the same method as outlined in Chapter 4.

Because a significant amount of time was required to pre-heat the stainless-steel discs, the total energy expended becomes an important factor for characterizing efficiency. Consider two thrusters; one a nitrous thruster employing an inductively

heated heat-exchanger and the other a resistojet that can impart the total pre-heat energy directly into the nitrous oxide propellant. The physical dimensions for the nitrous thruster match the experimental setup and both thrusters are assumed to operate at the same specific impulse (same exit gas temperature). The main difference between the two is the resistojet requires a constant power source to maintain a desired specific impulse, where as the self-sustaining system does not. Disregarding any exothermic effects from decomposition and assuming an exit gas temperature, the total amount of propellant mass that can be heated to a specific temperature using a reistojet is calculated using $E_o = m_p\, cp\, \Delta T$. E_o here is the total energy used to preheat the heat exchangers in the nitrous thruster. Since the resistojet is capable of directly heating the propellant, the total propellant mass capable of achieving the same specific impulse for a given E_o will be much higher. Therefore, from a total energy standpoint, there exists a breakeven operation time at which it becomes more efficient to use the nitrous thruster since it does not require an input power source at steady-state. This total time is a linear combination of the preheating time for the nitrous oxide thruster and the time required to expel the same amount of mass at constant specific impulse, a shown in Eq. (5.1).

$$t_{eff} = \frac{E_o}{P_w} + \frac{m_p}{\dot{m}} \qquad (5.1)$$

For the nitrous oxide tests, the total preheat time was approximately 18 minutes. Using the estimated induced power into the workpiece, E_o is 150 ± 10.8 kJ. With this much energy available, the resistojet is capable of heating 0.16 ± 0.01

kg of propellant assuming a constant specific heat capacity for nitrous oxide. The average flow rate tested in the laboratory experiments is 2.6 SLPM or $\sim 0.08 \frac{g}{s}$. At this flow rate, it would take almost 32 ± 3 minutes to flow the same amount of propellant as the resistojet. Therefore, the total time t_{eff} at which the nitrous thruster becomes more efficient is 50 ± 3 minutes. Beyond this breakeven, it is better to use the nitrous thruster as it is capable of producing the specific impulse for less total energy.

This calculated time, however, includes the inefficiencies from heat loss as the induced power in the workpiece raises the heat exchangers temperature. If it were possible to contain the heating of the workpiece to just the heat exchangers, the total energy required would be reduced. One approximation is to calculate the entire energy E_o needed to preheat the material using its density and total volume. Assuming the porosity of the heat exchanger is relatively low, consider a solid piece of stainless steel with a diameter equal to the housing (1 inch or 25.4 mm) and a length of 2.5 inches (63.5 mm). The total energy required to heat this stainless-steel rod to 1088 ± 21 K (temperature at which nitrous oxide was introduced) is approximately 105 ± 3 kJ. Assuming the power into the workpiece is the same, t_{eff} is now reduced to 36 ± 3 minutes.

In Eq. (5.1), the terms $E_o(\dot{m})$ and $m_p(\dot{m})$ are both a function of the mass flow rate. The total energy required to preheat a system using heat exchangers depends on the volume of the decomposition chamber, which as discussed above, needs to be scaled up for higher mass flow rates. As this energy increases, so will m_p. Therefore, using dimensional constants k_1 and k_2, Eq. (5.1) can be re-written as the following:

114

$$t_{eff} = \frac{k_1 \, \dot{m}^{1+\epsilon}}{P_w} + \frac{k_1 \, \dot{m}^{1+\epsilon}}{\dot{m}} \qquad (5.2)$$

In the above equation, it is assumed that the dependance on $\dot{m}$ is either linear, super-linear or sub-linear based on ϵ. If epsilon is positive, t_{eff} scales proportionally with $\dot{m}$. However, if epsilon is negative, there exists a minimum at some value of $\dot{m}$. As discussed, scaling $\dot{m}$ requires an increase gas density, gas velocity and cross-section area. Since the length of the chamber increases proportionally with gas velocity based on the Damköhler number, the total volume scales linearly with $\dot{m}$ and therefore so does the total energy required. This shows that t_{eff} will always increase with $\dot{m}$. Therefore, it is best to focus more on increasing P_w such that the total time for preheating is decreased for any desired mass flow rate.

Monopropellant thrusters are chosen to satisfy a variety of mission-specific requirements. Two common objectives for these thrusters are station-keeping and orbit-changing maneuvers. Station-keeping operations typically are short impulses and are therefore on the order of seconds at a time. Based on the energy analysis, it is unlikely that a thruster utilizing the concept of inductive heating in flight will ever be energy efficient for these types of maneuvers unless t_{eff} is reduced. For orbital maneuvers however, it might not be the case as these can last on the order of minutes. No matter the case, it is difficult to interpret t_{eff} without being mission specific.

5.3 Replacing Hydrazine

The objective of this work was to provide an alternative to catalytic decomposition of nitrous oxide such that its chances of replacing hydrazine as monopropellant are increased. Although the results were successful, mitigating the dependance on hydrazine for monopropellant systems is not as straightforward. Take, for example, hydrogen peroxide, which was one of the first candidates as a green monopropellant replacement. Although there is on-going research focused on developing its status as a candidate, progress has been slow primarily due to its performance. Simply put, the reduced performance from hydrogen peroxide cannot be overlooked. Marshall et al. [25] mentions that any hydrazine replacement must be able to produce the same or better performance. This ensures that the new propellant can match the mission-specific requirements and reduce any extra costs associated with using a newer propellant. The maximum specific impulse achievable for nitrous oxide decomposition is approximately 211 seconds, which is comparable to hydrazine performance, but not greater.

Another aspect to consider is the preheating required if using nitrous oxide with heat exchangers. Since hydrazine can decompose spontaneously on contact with a catalyst, it is appealing to missions with limited power available and that require thrusters to activate on a short notice [25]. Although the preheat time was considerably long in experiments, proper analysis on the inductive heating circuit can lead to a start up on the order of seconds. But to do so, however, will require more power for preheating. If implemented for a mission, the laboratory set-up

would require more than 1.4 kW of power to reduce the total preheat time below 2 minutes. As a scale, consider the *Landsat 8*, a NASA funded spacecraft that operated in a sun-synchronous low earth orbit. Its average orbital power was 1351 W (for 25 m^2 solar arrays) [100]. The laboratory thruster would exceed the power available on the entire spacecraft. In general, for any given orbit, a significant fraction of a spacecraft's mass will be dedicated to its power source, typically solar arrays. Therefore, increasing the power budget will typically lead to more mission costs, a huge disadvantage compared to other options. Of course, all spacecrafts have batteries that could be charged slowly and discharge when required to preheat the chamber. For a nominal battery density of 160 $\frac{Wh}{kg}$, a 0.2 kg battery would be required to preheat the chamber [101]. Assuming the battery will support other operations on the spacecraft, this mass is well within the typical restrictions found in current missions. If the thruster duty cycle is low (1%), then the battery would only require 14 W of power to charge before discharging quickly for preheating. If required to fire the thruster in under seconds of preheating, the power required to charge the batteries does scale up to 35 W at the same duty cycle. The battery mass, however, does not change since the total energy required is constant.

The inductive circuit used might not be acceptable for missions requiring thrusters with minimal volumetric footprint. The circuits tested in this work were primarily selected due to their power capabilities and size of the induction coil. Although preliminary tests were focused towards identifying some parameters better suited for heating, further trade studies on how to to maximize the induced power for a given workpiece while minimizing its mass and volume were beyond the scope.

117

Typical hydrazine and other catalyst-driven thrusters employ heaters that do not necessarily add any additional footprint since they do not need to reach thermal decomposition temperatures during the preheat phase. Any development towards using inductive heating for thruster applications will need to focus on resizing the circuit in order to minimize its relative volume. If the inductive circuit does not meet mission constraints, an alternative solution could be combusting a nitrous oxide-hydrocarbon fuel blend to first preheat the chamber. Although this would remove the inductive circuit altogether, the spacecraft would have to carry additional storage for the hydrocarbon fuel.

Nonetheless, it must be restated that the harsh thermal conditions due to decomposition cause the destruction of the catalyst, regardless of which propellant is used. Monopropellant thruster lifetime is heavily dictated by the condition of the catalyst used. The use of heat exchangers at thermal decomposition temperatures as a replacement of catalysts helps address this issue, at least for nitrous oxide. Therefore, a nitrous oxide thruster using this concept can present itself as a candidate for replacing hydrazine and other monopropellants if it can achieve a specific impulse close to its theoretical maximum, preheat in a relatively short amount of time, be easily scaled for mass flow rates while maintaining an acceptable physical footprint, and operate for a similar or greater lifespan than that of existing thrusters.

Chapter 6:   Conclusion

Recent years have witnessed a surge in interest for finding a green monopropellant to replace hydrazine. One candidate is nitrous oxide; considered much less toxic and among other advantages, is capable of producing specific impulses close to that of hydrazine. Most monopropellant thrusters function with the aid of a catalyst. Although they help reduce the activation energy required for the exothermic decomposition of such propellants, thermal degradation limits their performance and dictates thruster lifetime. Specifically, thrusters that utilize catalysts depend on their high effective surface area to guarantee full decomposition of the propellant. Thermal degradation of the catalyst reduces the effective surface area, catastrophically affecting thruster lifetime and performance. This work aimed to address this issue by replacing catalysts with high temperature heat exchangers to decompose nitrous oxide and achieve steady-state. The heat exchangers tested have a significantly less effective surface area than catalysts and therefore significantly mitigate the effect of any degradation on thruster functionality. The first half of the study was dedicated to a numerical model and performed a large parametric study on nitrous oxide decomposition. The second portion used the modeling results to test three different heat exchangers.

6.1   Numerical Model

The model developed in Chapter 3 was a 1-D compressible fluid model that was capable of simulating nitrous oxide decomposition through a conducting metal foam (referred to as a block). Derived from the conservation equations, it tracks the gas temperature, block temperature, and gas density. The simulation employs the conducting metal foam to harness some of the released decomposition energy to help decompose incoming nitrous oxide gas. The effects of various thermal and system parameters were studied to help understand how to achieve self-sustained decomposition. One characteristic common throughout all solutions is that the exit gas temperature is approximately equal to the exit foam temperature. Therefore, the limiting aspect of this approach is directly dependent on the melting point of the metal used for the foam. For copper foam, this temperature is 1350 K. Simulations with other metal foams that have higher melting points do show it is feasible to bypass this limitation and even increase the gas temperature.stainless-steel One aspect to consider is materials with a higher melting point tend to have lower thermal conductivities, which directly impact the foam temperature profile. Using these high temperature materials, however, provide an alternative to catalysts for nitrous oxide and monopropellant decomposition in general. Furthermore, solutions simulating mass flow rates more representative of existing monopropellant thrusters achieved self-sustained decomposition given proper system scaling. Extending this model to other heat exchangers, not just a metal foam, is relatively easy. Along with the physical dimensions and the associated thermal properties, only the effective surface

area and porosity are required to model any heat exchanger.

6.2   Experimental Work

Using the results from the numerical model as guidelines, three different heat exchangers were tested in an evacuated bell jar. All three had effective surface areas much lower than that of typical catalysts used for decomposition. In order to preheat the heat exchangers to thermal decomposition temperatures, an inductive heating circuit was implemented inside the evacuated bell jar. The heating mechanism was successful in heating the heat exchangers above 1200 K without any contact. The first heat exchanger tested was the copper metal foam modeled in Chapter 3. Although preliminary tests showed successful preheating, no steady-state tests were successful. In fact, the copper metal underwent strong oxidation due to nitrous oxide decomposition. The second heat exchanger was a set of copper discs aimed at addressing the oxidation issues from the metal foam. Data from preheating correctly identified two different regimes due to hysteresis effects. Steady-state tests showed successful decomposition using nitrous oxide, with exit gas temperatures close to 1250 K. Unfortunately, the second heat exchanger failed relatively quickly due to partial melting within the heat exchanger. Since the downstream thermocouple never measured temperatures within 100 K of copper's melting point, there must have been some thermal disconnect between the downstream copper discs and the rest of the heat exchanger.

The third heat exchanger tested was a set of stainless-steel discs which have a

higher melting point and a stronger resistance to oxidation. A total of three tests were conducted with nitrous oxide, all showing successful decomposition within a two minute interval. Further analysis concluded that systems requiring a longer run time might not be able to maintain steady-state, at least for tested system parameters without a feedback control on the mass flow rate. To further substantiate the steady-state results, three tests were run with carbon dioxide as a control. As expected, no steady-state solution was achieved as the system rapidly cooled once input power was turned off. Power analysis confirmed the energy released from decomposition was at least equal to the energy deposited into the workpiece from the inductive circuit.

6.3 Thruster Analysis

The mass flow rates used in the model and in the experimental tests are much lower than those found in existing thrusters. When scaling up the system to accommodate higher flow rates, there are two criteria to consider. The first is to maintain a high Damköhler number to ensure that the fluidic time scales are longer than the reaction time scales. The other is to ensure the physical dimensions of the decomposition chamber are comparable to existing monopropellant thrusters. Although the model can help verify steady-state decomposition when scaling to higher mass flow rates, further work needs to be directed towards capturing all the heat loss within the system. When compared to a resistojet, analysis concluded there is a certain operation time at which a thruster employing inductively heated heat-

exchangers become more efficient. This operation time, at least for the experimental tests, is on the order of minutes and is much longer than the typical operation time of monopropellant thrusters used for station-keeping. Longer-duration thrusters, used for orbit maneuvers, might be able to benefit from utilizing this concept.

6.4 Future Work

The first step to advancing this work must focus on transforming the numerical model into at least a two-dimensional axisymmetric system. When using a one-dimensional approach, an assumption on temperature uniformity in the radial axis has to be made. An extension of this objective should also aim to provide a more comprehensive image of the heat loss experienced within the chamber, including upstream and downstream of the heat exchanger. The updated model should be validated with experimental results. Furthermore, although the model can simulate various heat exchangers, it assumes the material is isotropic and therefore can not simulate composite materials. Since a large part of this work emphasizes the type of heat exchanger used, one avenue of future work should focus on composites. As discussed throughout this work, many of the heat transfer parameters are all approximations using general analytical equations found in literature. It would be helpful to direct resources towards further validating these parameters to a specific system. For example, the heat transfer coefficient should be a function of the gas and heat exchanger in question. Finally, the model is incapable of producing transient solution due to a limitation of computational resources. Addressing this issue will

provide further insight on the initial onset of decomposition.

Concluding from the power and energy efficiency analysis, it is apparent that a large amount of work needs to be directed towards the inductive heating mechanism. It was identified from both experiments and analysis that a significant amount of power is lost to the inductive circuit due to localized heating. In addition, the circuits used carried a large volume and mass footprint, not ideal for monopropellant thrusters. Designing and testing a custom circuit might help address both of these issues. One obstacle that needs to be tackled is the total time required to preheat the heat exchangers. The longer it takes, the less usability such a thruster will have for chemical propulsion applications. Parametric studies on heating and system parameters focused on maximizing the the overall coupling between the coil and workpiece can help increase the induced power and reduce the preheat time. An ideal scenario would be a system capable of heating the decomposition chamber in less than a few seconds. If a re-design of the inductive circuit proves to be unsuccessful, an alternative approach could be using a nitrous oxide-hydrocarbon fuel blend to first preheat the chamber. This approach, however, would require further trade studies to quantify if it is more advantageous from a power, operational time and mass standpoint.

Following the results from the experimental work, the next steps should primarily focus on scaling the laboratory set-up to match flow rates in current thrusters. Producing experimental results with exit gas temperatures close to the theoretical maximum would certainly advance this concept. Achieving this requires better containment of the decomposition energy at steady-state. Preliminary analysis showed

a significant fraction of decomposition energy lost to the decomposition chamber itself. Reducing this should increase the expected specific impulse for the system. Furthermore, porting the system to an actual thruster design with an exit nozzle would provide concrete evidence on its feasibility. Trade studies on different geometries of heat exchangers can help identify which physical characteristics assist decomposition the most. It would also be beneficial to acquire temperatures at various locations axially along the heat exchanger. This would further validate the numerical model, especially if multi-dimensional. In addition, correcting the thermocouple measurements to account for radiation and conduction losses would help provide a more accurate representation of gas temperature. Experimenting with different housing and heat exchanger materials could result in finding the optimum that maximizes heating efficiency while minimizing corrosion and melting. Finally, it would help to quantify degradation and operation lifetime of a thruster when using inductively heated heat-exchangers.

Bibliography

[1] Nicholas Tsolas. Thermal spray forming of high-efficiency metal-foam heat exchangers. Master's thesis, University of Toronto, Toronto, January 2010.

[2] Taheri Mehrdad. *Analytical and Numerical Modeling of Fluid Flow and Heat Transfer through Open-cell Metal Foam Heat Exchangers*. PhD thesis, University of Toronto, Toronto, 2015.

[3] Vadim Zakirov, Martin Sweeting, Volker Goeman, and Timothy Lawrence. Surrey research on nitrous oxide catalytic decomposition for space applications. In *Proceedings of the 14th Annual AIAA/USU Conference on Small Satellites*, pages 1–9, Utah, 2000. Digital Commons. SSC00-XI-7.

[4] Vadim Zakirov, Martin Sweeting, Timothy Lawrence, and Jerry Sellers. Nitrous oxide as a rocket propellant. *Acta Astronautica*, 48(5):353 – 362, 2001.

[5] Akira Kakami, Taku Egawa, Natsuki Yamamoto, and Takeshi Tachibana. Plasma-assisted combustion of n2o/ethanol propellant for space propulsion. In *Proceedings of the 46th AIAA/ASME/SAE/ASEE Joint Propulsion Conference & Exhibit*, Nashville, Tennessee, November 2010. AIAA. AIAA 2010-6806.

[6] Luciano Hennemann, José Carlos de Andrade, and Fernando De Souza Costa. Experimental investigation of a monopropellant thruster using nitrous oxide. *Journal of Aerospace Technology and Management*, 6(4):363–372, 2014.

[7] J Wallbank, P Sermon, A Baker, L Courtney, and R Sambrook. Nitrous oxide as a green monopropellant for small satellites. In *Proceedings of the 2nd International Conference on Green Propellants for Space Propulsion (ESA SP-557)*, pages 125–130, Sardinia, Italy, June 2004. ESA Publications Division.

[8] Arif Karabeyoglu, Jonny Dyer, Jose Stevens, and Brian Cantwell. Modeling of n_2o decomposition events. In *Proceedings of the 44th AIAA/ASME/SAE/ASEE Joint Propulsion Conference & Exhibit*, Hartford, Connecticut, June 2012. AIAA. AIAA 2008-4933.

[9] Morris Argyle and Calvin Bartholomew. Heterogeneous Catalyst Deactivation and Regeneration: A Review. *Catalysts*, 5(1):145–269, February 2015.

[10] Jincheol Kim and Taegyu Kim. Study on Endurance and Performance of Impregnated Ruthenium Catalyst for Thruster System. *Journal of nanoscience and nanotechnology*, 18(2):1263–1265, February 2018.

[11] Dongwook Jang, Shinjae Kang, and Sejin Kwon. Preheating Characteristics of H_2O_2 Monopropellant Thruster Using Manganese Oxide Catalyst. *Aerospace Science and Technology*, 41:24–27, February 2015.

[12] T.G. Soares Neto, J. Gobbo-Ferreira, A.J.G. Cobo, and G.M. Cruz. $Ir-Ru/Al_2O_3$ Catalysts used in Satellite Propulsion. *Brazilian Journal of Chemical Engineering*, 20:273 – 282, 09 2003.

[13] Seonuk Heo, Sungkwon Jo, Yongtae Yun, and Sejin Kwon. Effect of Dual-Catalytic Bed using Two Different Catalyst Sizes for Hydrogen Peroxide Thruster. *Aerospace Science and Technology*, 78:26–32, July 2018.

[14] P. S. Saripalli and R. J. Sedwick. One-dimensional numerical model of nitrous oxide decomposition using a metal foam. *Journal of Propulsion and Power*, 2019. Accessed June 17, 2019.

[15] George P Sutton and Oscar Biblarz. *Rocket Propulsion Elements*, chapter 7. John Wiley & Sons, Hoboken, New Jersey, November 2016.

[16] M Russi. A Survey of Monopropellant Hydrazine Thruster Technology. In *9th Propulsion Conference*, Reston, Virigina, February 2013. American Institute of Aeronautics and Astronautics.

[17] Charles Brown. *Spacecraft Propulsion*. AIAA education series. American Institute of Aeronautics & Astronautics, 1996.

[18] Carl Wagner. The Mechanism of the Decomposition of Nitrous Oxide on Zinc Oxide as Catalyst. *The Journal of Chemical Physics*, 18(1):69–71, December 2004.

[19] Andrey Zeigarnik. Adsorption and Reactions of N_2O on Transition Metal Surfaces. *Kinetics and Catalysis*, 44(2):233–246, 2003.

[20] K Li, X F Wang, and H C Zeng. Kinetics of $N_2 0$ Decomposition on a RuO_2/Al_2O_3 Catalyst. *Chemical Engineering Research and Design*, 75(8):807–812, November 1997.

[21] John H Sinfelt. Structure of Metal Catalysts. *Reviews of Modern Physics*, 51(3):569–589, July 1979.

[22] Bahareh Tavakoli, Sonia Eskandari, Umema Khan, Rembert White, and John R. Regalbuto. *A Review of Preparation Methods for Supported Metal Catalysts.* 01 2017.

[23] Morris Argyle and Calvin Bartholomew. Heterogeneous Catalyst Deactivation and Regeneration: A Review. *Catalysts*, 5(1):145–269, February 2015.

[24] Chang Hwan Hwang, Sung Nam Lee, Seung Wook Baek, Cho Young Han, Su Kyum Kim, and Myoung Jong Yu. Effects of Catalyst Bed Failure on Thermochemical Phenomena for a Hydrazine Monopropellant Thruster Using Ir/Al2O3 Catalysts. *Industrial & Engineering Chemistry Research*, 51(15):5382–5393, 2012.

[25] W M Marshall and C M Deans. Recommended figures of merit for green monopropellants. In *49th AIAA/ASME/SAE/ASEE Joint Propulsion Conference*, California, 2013. AIAA 2013-3722.

[26] Eric Wernimont. System Trade Parameter Comparison of Monopropellants: Hydrogen Peroxide vs Hydrazine and Others. In *42nd AIAA/ASME/SAE/ASEE Joint Propulsion Conference & Exhibit*, page 03, Reston, Virigina, June 2012. American Institute of Aeronautics and Astronautics.

[27] Robert L Sackheim and Robert K Masse. Green Propulsion Advancement: Challenging the Maturity of Monopropellant Hydrazine. *Journal of Propulsion and Power*, 30(2):265–276, March 2014.

[28] E J Wucherer, Timothy Cook, Mark Stiefel, Randy Humphries, and Janet Parker. Hydrazine Catalyst Production - Sustaining S-405 Technology. In *39th AIAA/ASME/SAE/ASEE Joint Propulsion Conference and Exhibit*, Reston, Virigina, June 2012. American Institute of Aeronautics and Astronautics.

[29] Sungyong An, Jungkun Jin, Jeongsub Lee, Sungkwon Jo, Daejong Park, and Sejin Kwon. Chugging Instability of H_2O_2 Monopropellant Thrusters with Reactor Aspect Ratio and Pressures. *Journal of Propulsion and Power*, 27(2):422–427, March 2011.

[30] Sungkwon Jo, Dongwuk Jang, Jonghak Kim, Hosung Yoon, and Sejin Kwon. Chugging Instability of H_2O_2 Monopropellant Thrusters with Catalyst Reactivity and Support Sizes. In *47th AIAA/ASME/SAE/ASEE Joint Propulsion Conference & Exhibit*, page 574, Reston, Virigina, November 2012. American Institute of Aeronautics and Astronautics.

[31] R J Koopmans, J S Shrimpton, G T Roberts, and A J Musker. Dependence of Pellet Shape and Size on Pressure Drop in H_2O_2 Thrusters. *Journal of Propulsion and Power*, 30(3):775–789, May 2014.

[32] Angelo Cervone, Lucio Torre, Luca d'Agostino, Antony J Musker, Graham T Roberts, Cristina Bramanti, and Giorgio Saccoccia. Development of Hydrogen Peroxide Monopropellant Rockets. In *42nd AIAA/ASME/SAE/ASEE Joint Propulsion Conference & Exhibit*, Reston, Virigina, June 2012. American Institute of Aeronautics and Astronautics.

[33] M Ventura and P Mullens. The use of hydrogen peroxide for propulsion and power. In *35th Joint Propulsion Conference and Exhibit*, page 283, Reston, Virigina, February 2013. American Institute of Aeronautics and Astronautics.

[34] O V Romantsova and V B Ulybin. Safety issues of high-concentrated hydrogen peroxide production used as rocket propellant. *Acta Astronautica*, 109:231–234, April 2015.

[35] Antony Musker. Highly Stabilised Hydrogen Peroxide as a Rocket Propellant. In *39th AIAA/ASME/SAE/ASEE Joint Propulsion Conference and Exhibit*, Reston, Virigina, June 2012. American Institute of Aeronautics and Astronautics.

[36] H J Tian, T Zhang, X Y Sun, D B Liang, and L W Lin. Performance and deactivation of Ir/gamma-Al2O3 catalyst in the hydrogen peroxide monopropellant thruster. *Applied Catalysis a-General*, 210(1-2):55–62, 2001.

[37] A Pasini, L Torre, L Romeo, A Cervone, and L d'Agostino. Performance Characterization of Pellet Catalytic Beds for Hydrogen Peroxide Monopropellant Rockets. *Journal of Propulsion and Power*, 27(2):428–436, March 2011.

[38] A Pasini, L Torre, L Romeo, A Cervone, and L d'Agostino. Testing and characterization of a hydrogen peroxide monopropellant thruster. *Journal of Propulsion and Power*, 24(3):507–515, 2008.

[39] David Krejci, Sebastian Schuh, Robert-Jan Koopmans, and Carsten Scharlemann. Impact of Catalyst Length and Preheating on Transient Catalytic H_2O_2 Decomposition Performance. *Journal of Propulsion and Power*, 31(3):985–989, May 2015.

[40] Hongjae Kang, Dahae Lee, Shinjae Kang, and Sejin Kwon. Effect of H_2O_2 injection patterns on catalyst bed characteristics. *Acta Astronautica*, 130:75–83, 2017.

[41] David Krejci, Alexander Woschnak, Markus Schiebl, Carsten Scharlemann, Karl Ponweiser, Rachid Brahmi, Yann Batonneau, and Charles Kappenstein. Assessment of Catalysts for Hydrogen-Peroxide-Based Thrusters in a Flow Reactor. *Journal of Propulsion and Power*, 29(2):321–330, 2013.

[42] Mark Ventura and D Durant. Field Handling of Hydrogen Peroxide. In *40th AIAA/ASME/SAE/ASEE Joint Propulsion Conference and Exhibit*, Reston, Virigina, June 2012. American Institute of Aeronautics and Astronautics.

[43] Amir S Gohardani, Johann Stanojev, Alain Demaire, Kjell Anflo, Mathias Persson, Niklas Wingborg, and Christer Nilsson. Green space propulsion: Opportunities and prospects. *Progress in Aerospace Sciences*, 71:128–149, November 2014.

[44] Vittorio Bombelli, Dieter Simon, Jean-Luc Moerel, and Ton Marée. Economic Benefits of the Use of Non-Toxic Mono-Propellants for Spacecraft Applications. In *39th AIAA/ASME/SAE/ASEE Joint Propulsion Conference and Exhibit*, page 1, Reston, Virigina, June 2012. American Institute of Aeronautics and Astronautics.

[45] Rachid Amrousse, Keiichi Hori, Wafa Fetimi, and Kamal Farhat. HAN and ADN as liquid ionic monopropellants: Thermal and catalytic decomposition processes. *Applied Catalysis B: Environmental*, 127:121–128, 2012.

[46] Michele Negri, Marius Wilhelm, Christian Hendrich, Niklas Wingborg, Linus Gediminas, Leif Adelow, Corentin Maleix, Pierre Chabernaud, Rachid Brahmi, Romain Beauchet, Yann Batonneau, Charles Kappenstein, Robert-Jan Koopmans, Sebastian Schuh, Tobias Bartok, Carsten Scharlemann, Ulrich Gotzig, and Martin Schwentenwein. New technologies for ammonium dinitramide based monopropellant thrusters - The project RHEFORM. *Acta Astronautica*, 143:105–117, February 2018.

[47] Christopher H McLean. Green Propellant Infusion Mission (GPIM), Advancing the State of Propulsion System Safety and Performance. In *54th AIAA Aerospace Sciences Meeting*, Reston, Virginia, January 2016. American Institute of Aeronautics and Astronautics.

[48] Rachid Amrousse, Toshiyuki Katsumi, Nobuyuki Azuma, and Keiichi Hori. Hydroxylammonium nitrate (HAN)-based green propellant as alternative energy resource for potential hydrazine substitution: From lab scale to pilot plant scale-up. *Combustion and Flame*, 176:334–348, February 2017.

[49] B Slettenhaar, J Zevenbergen, H Pasman, A Maree, and J Moerel. Study on Catalytic Ignition of HNF Based Non Toxic Monopropellants. In *39th AIAA/ASME/SAE/ASEE Joint Propulsion Conference and Exhibit*, page 225, Reston, Virigina, June 2012. American Institute of Aeronautics and Astronautics.

[50] Abhijit Dey, Arun Kanti Sikder, Mahadev B Talawar, and Santanu Chottopadhyay. Towards New Directions in Oxidizers/Energetic Fillers for Composite Propellants: an Overview. *Central European Journal of Energetic Materials*, 12(2):377–399, 2015.

[51] Kamal Farhat, Charles Kappenstein, and Yann Batonneau. Thermal and Catalytic Decomposition of AN-, ADN and HNF-Based Ionic Monopropellants. In *44th AIAA/ASME/SAE/ASEE Joint Propulsion Conference & Exhibit*, page 213, Reston, Virigina, June 2012. American Institute of Aeronautics and Astronautics.

[52] L Courtheoux, D Amariei, S Rossignol, and C Kappenstein. Thermal and catalytic decomposition of HNF and HAN liquid ionic as propellants. *Applied Catalysis B: Environmental*, 62(3-4):217–225, 2006.

[53] Rupesh Aggarwal, Ishan Patel, and P Sharma. Green propellant: A study. *International Journal of Latest Trends in Engineering and Technology*, 6, 09 2015.

[54] Vadim Zakirov, Martin Sweeting, and Timothy Lawrence. An update on surrey nitrous oxide catalytic decomposition research. In *Proceedings of the 15th Annual AIAA/USU Conference on Small Satellites*, pages 1–9, 2001. SSC01-XI-2.

[55] Hans Beyer, Jens Emmerich, Konstantinos Chatziapostolou, and Klaus Koehler. Decomposition of Nitrous Oxide by Rhodium Catalysts: Effect of Rhodium Particle Size and Metal Oxide Support. *Applied Catalysis A-General*, 391(1-2):411–416, 2011.

[56] Chao Sui, Fulong Yuan, Zhiping Zhang, Chi Zhang, Xiaoyu Niu, and Yujun Zhu. Effect of Ru Species on N_2O Decomposition over Ru/Al2O3 Catalysts. *Catalysts*, 6(11):173, November 2016.

[57] Junko Oi, Akira Obuchi, Gratian R Bamwenda, Atsushi Ogata, Hiroshi Yagita, Satoshi Kushiyama, and Koichi Mizuno. Decomposition of Nitrous Oxide over Supported Rhodium Catalysts and Dependency on Feed Gas Composition. *Applied Catalysis B: Environmental*, 12(4):277–286, July 1997.

[58] Michalis Konsolakis. Recent Advances on Nitrous Oxide (N2O) Decomposition over Non-Noble-Metal Oxide Catalysts: Catalytic Performance, Mechanistic Considerations, and Surface Chemistry Aspects. *ACS Catalysis*, 5(11):6397–6421, September 2015.

[59] Kevin Lohner, Jonny Dyer, Eric Doran, Zachary Dunn, Brian Krieger, Valentin Decker, Eric Wooley, Andy Sadhwani, Brian Cantwell, and Thomas Kenny. Design and Development of a Sub-Scale Nitrous Oxide Monopropellant Gas Generator. In *43rd AIAA/ASME/SAE/ASEE Joint Propulsion Conference & Exhibit*, page 1695, Reston, Virigina, June 2012. American Institute of Aeronautics and Astronautics.

[60] Hans Beyer, Jens Emmerich, Konstantinos Chatziapostolou, and Klaus Koehler. Decomposition of Nitrous Oxide by Rhodium Catalysts: Effect of Rhodium Particle Size and Metal Oxide Support. *Applied Catalysis a-General*, 391(1-2):411–416, 2011.

[61] Runhu Zhang, Chao Hua, Bingshuai Wang, and Yan Jiang. N2O Decomposition over Cu–Zn/γ–Al2O3 Catalysts. *Catalysts*, 6(12):200, December 2016.

[62] Xiangyun Zhao, Yu Cong, Fei Lv, Lin Li, Xiaodong Wang, and Tao Zhang. Mullite-supported Rh catalyst: a promising catalyst for the decomposition of N2O propellant. *Chemical Communications*, 46(17):3028–3030, 2010.

[63] Woo Jun You, Hee Jang Moon, Seok Pil Jang, and Jin Kon Kim. Thermal characteristics of an N2O catalytic igniter with metal foam for hybrid rocket motors. *International Journal of Heat and Mass Transfer*, 66:101–110, November 2013.

[64] Matthew Wilson. Catalytic decomposition of nitrous oxide monopropellant for hybrid motor ignition. *ProQuest Dissertations And Theses; Thesis (M.S.)– Utah State University*, 2013.

[65] Pratik Saripalli and Raymond J Sedwick. Development of a green propellant station-keeping thruster using a dielectric barrier discharge. In *Proceedings of the 49th AIAA/ASME/SAE/ASEE Joint Propulsion Conference*, San Jose, California, July 2013. AIAA. AIAA 2013-3882.

[66] Jin-Oh Jo, Quang Hung Trinh, Seong H Kim, and Young Sun Mok. Plasma-catalytic decomposition of nitrous oxide over gamma-alumina-supported metal oxides. *Catalysis Today*, 310:42–48, 2018.

[67] M Galle, D W Agar, and O Watzenberger. Thermal N2O decomposition in regenerative heat exchanger reactors. *Chemical Engineering Science*, 56(4):1587–1595, February 2001.

[68] Max Vozoff and Greg Mungas. NOFBX™: A Non-Toxic, "Green" Propulsion Technology with High Performance and Low Cost. In *AIAA SPACE 2012 Conference & Exposition*, page 49, Reston, Virigina, September 2012. American Institute of Aeronautics and Astronautics.

[69] Xuesen Yang, Xin Hong, and Wei Dong. Investigation on self-pressurization and ignition performance of nitrous oxide fuel blend ethylene thruster. *Aerospace Science and Technology*, 82-83:161–171, November 2018.

[70] G. Mungas, D. Fisher, J. Vozoff, and M. Villa. Nofbx™ single stage to orbit mars ascent vehicle. In *2012 IEEE Aerospace Conference*, pages 1–11, March 2012.

[71] R Taylor. Safety and Performance Advantages of Nitrous Oxide Fuel Blends (NOFBX) Propellants for Manned and Unmanned Spaceflight Applications. In *Proceedings of the 5th IAASS Conference A Safer Space for Safer World*, page 67, January 2012.

[72] Nihad Dukhan. *Metal Foams: Fundamentals and Applications*, chapter 2. Destech Publications, Lancaster, PA, 2013.

[73] J.D. Anderson. *Fundamentals of Aerodynamics*, chapter 2, 7,15. McGraw-Hill Education, New York, 2016.

[74] R.B. Bird, W.E. Stewart, and E.N. Lightfoot. *Transport Phenomena*, chapter 9, 17. Wiley, New York, 2002.

[75] Michael Röhrig, Eric L Petersen, David F Davidson, and Ronald K Hanson. The pressure dependence of the thermal decomposition of n_2o. *International Journal of Chemical Kinetics*, 28(8):599–608, 1996.

[76] Mark T Allen, Richard A Yetter, and Frederick L Dryer. The decomposition of nitrous oxide at $1.5 \leq p \leq 10.5$ atm and $1103 \leq t \leq 1173$ k. *International Journal of Chemical Kinetics*, 27(9):883–909, 1995.

[77] Gerhard Löffler, Verina J Wargadalam, Franz Winter, and Hermann Hofbauer. Decomposition of nitrous oxide at medium temperatures. *Combustion and Flame*, 120(4):427–438, 2000.

[78] J Troe and V G Ushakov. Revisiting falloff curves of thermal unimolecular reactions. *The Journal of Chemical Physics*, 135(5):054304, 2011.

[79] Guillermo A Narsilio, Olivier Buzzi, Stephen Fityus, Tae Sup Yun, and David W Smith. Upscaling of navier–stokes equations in porous media: Theoretical, numerical and experimental approach. *Computers and Geotechnics*, 36(7):1200–1206, 2009.

[80] Nihad Dukhan, Özer Bağcı, and Mustafa Özdemir. Metal foam hydrodynamics: Flow regimes from pre-Darcy to turbulent. *International Journal of Heat and Mass Transfer*, 77:114–123, October 2014.

[81] Ahmed Kouidri and Brahim Madani. Experimental hydrodynamic study of flow through metallic foams: Flow regime transitions and surface roughness influence. *Mechanics of Materials*, 99:79–87, August 2016.

[82] K Boomsma and D Poulikakos. The Effects of Compression and Pore Size Variations on the Liquid Flow Characteristics in Metal Foams. *Journal of Fluids Engineering*, 124(1):263–272, March 2002.

[83] V V Calmidi and R L Mahajan. Forced Convection in High Porosity Metal Foams. *Journal of Heat Transfer*, 122(3):557, 2000.

[84] Donald A. Nield and Adrian Bejan. *Heat Transfer Through a Porous Medium*, pages 37–55. Springer International Publishing, Cham, Switzerland, 2017.

[85] L.J. Gibson and M.F. Ashby. *Cellular Solids: Structure and Properties*, chapter 7. Cambridge Solid State Science Series. Cambridge University Press, Cambridge, United Kingdom, 1999.

[86] T. Kajishima and K. Taira. *Computational Fluid Dynamics: Incompressible Turbulent Flows*, chapter 2. Springer International Publishing, Cham, Switzerland, 2016.

[87] Andrea Diani, Kartik K Bodla, Luisa Rossetto, and Suresh V Garimella. Numerical Analysis of Air Flow through Metal Foams. *Energy Procedia*, 45:645–652, June 2014.

[88] Structural impact of honeycomb catalysts on hydrogen peroxide decomposition for micro propulsion. *Chemical Engineering Research and Design*, 90(12):2302–2315, December 2012.

[89] Xu Zhou and Darren Hitt. Numerical modeling of monopropellant decomposition in a micro-catalyst bed. 35th AIAA Fluid Dynamics Conference and Exhibit, 06 2005.

[90] Wei Wang, Bi Zhong Xia, and Hong Hua Sun. Simulation Study of HTP Decomposition within Silver Screen Catalyst Bed of the Monopropellant Gas Generator. *Applied Mechanics and Materials*, 404:436–441, September 2013.

[91] J H Corpening, S D Heister, W E Anderson, and B L Austin. Thermal Decomposition of Hydrogen Peroxide, Part 2: Modeling Studies. *Journal of Propulsion and Power*, 22(5):996–1005, May 2012.

[92] M Martinez-Sanchez and J E Pollard. Spacecraft Electric Propulsion - An Overview. *Journal of Propulsion and Power*, 14(5):688–699, 1998.

[93] Carsten Scharlemann, M Schiebl, K Marhold, Martin Tajmar, P Miotti, C Kappenstein, Y Batonneau, R Brahmi, and C Hunter. Development and Test of a Miniature Hydrogen Peroxide Monopropellant Thruster. In *42nd AIAA/ASME/SAE/ASEE Joint Propulsion Conference & Exhibit*, page 307, Reston, Virigina, June 2012. American Institute of Aeronautics and Astronautics.

[94] Redha Amri, D Gibbon, and T Rezoug. The Design, Development and Test of One Newton Hydrogen Peroxide Monopropellant Thruster. *Aerospace Science and Technology*, 25(1):266–272, March 2013.

[95] S. Zinn, S.L. Semiatin, E.P.R. Institute, and B.M.I.C. Laboratories. *Elements of Induction Heating: Design, Control, and Applications*, chapter 2. A S M International, 1988.

[96] V. Rudnev, D. Loveless, R.L. Cook, and M. Black. *Handbook of Induction Heating*, chapter 3. Manufacturing Engineering and Materials Processing. CRC Press, Florida, 2002.

[97] Y F Zhu, K Mimura, and M Isshiki. Oxidation Mechanism of Copper at 623-1073 K. *Materials Transactions*, 43(9):2173–2176, September 2002.

[98] Alenka Vesel, Miran Mozetic, Aleksander Drenik, Nina Hauptman, and Marianne Balat-Pichelin. High Temperature Oxidation of Stainless Steel AISI316L in air plasma. *Applied Surface Science*, 255(5):1759–1765, December 2008.

[99] J. Davies and Institution of Electrical Engineers. *Conduction and Induction Heating*, chapter 10. Energy Engineering Series. P. Peregrinus Limited, United Kingdom, 1990.

[100] Landsat data continuation mission press kit. *NASA*, Feb 2013.

[101] Energy storage technologies for future planetary science missions. *NASA*, Dec 2017. JPL D-101146.